

---

# Setup of a Transportable Yb Optical Lattice Clock

---

Inaugural-Dissertation

zur

Erlangung des Doktorgrades der  
Mathematisch-Naturwissenschaftlichen Fakultät  
der Heinrich-Heine-Universität Düsseldorf

vorgelegt von

**Charbel Abou Jaoudeh**

aus Zalka, Libanon

Februar 2016

Aus dem Institut für Experimentalphysik  
der Heinrich-Heine-Universität Düsseldorf

Gedruckt mit der Genehmigung der  
Mathematisch-Naturwissenschaftlichen Fakultät der  
Heinrich-Heine-Universität Düsseldorf

Referent:	Prof. Dr. Axel Görlitz
Koreferent:	Prof. Dr. Stephan Schiller
Tag der mündlichen Prüfung:	29.09.2015

# Summary

In this thesis, a transportable setup of an Yb atomic source for a lattice optical clock is built and characterized [1] [2]. All three laser setups for cooling and trapping the Yb atoms, together with the vacuum system, are contained on a transportable  $2 \times 1$  m<sup>2</sup> optical table.

The preparation of the atomic sample before doing spectroscopy on the clock transition starts by slowing the atoms in the Zeeman slower. This is followed by trapping the atoms in the pre-cooling and the post-cooling MOTs, before loading the atoms into the optical lattice. Slowing and pre-cooling the atoms is done using the strong  $^1S_0$ - $^1P_1$  transition at 399 nm [3]. This cools the  $10^6$  atoms down to around a mK. To successfully load the atoms in the optical lattice, we have to cool the atoms further to beyond  $50 \mu\text{K}$ . This is done by exciting the weak  $^1S_0$ - $^3P_1$  transition at 556 nm [4]. The  $10^5$  transferred atoms into the post-cooling stage are cooled down to a few tens of  $\mu\text{K}$ . The atoms are then ready to be loaded into the optical lattice at the magic wavelength. The amplified laser light at 760 nm inside the 1-D intra-vacuum cavity results in a lattice trapping potential of approximately  $50 \mu\text{K}$ . A transfer efficiency, from the MOT into the optical lattice, of more than 25% was measured.

The spectroscopy on the clock transition was done for  $^{171}\text{Yb}$ . A step-by-step mechanism was adopted, starting by exciting the forbidden  $^1S_0$ - $^3P_0$  transition at 578 nm inside the post-cooling stage MOT, by using the "chopped-MOT" method. The 300 kHz Doppler-broadened line is then narrowed down to 3 kHz by switching on the light at 760 nm, while keeping the MOT on. The so-called "chopped-lattice" technique helped suppress the Doppler-broadening; however the other effects due to the light and the magnetic fields of the MOT were still present. By switching off the MOT's light and magnetic fields, the Yb atoms are completely trapped in the optical lattice. As a result, the FWHM of the spectroscopy line was reduced by a factor of 10.

In the frame of this thesis, the clock transition for  $^{171}\text{Yb}$  was observed for the first time using this apparatus. In-between, improvements on the experimental setup have been made by another Ph.D. student, and better measurements of the clock transition have been observed [5]. Moreover, the transportability of the experiment was successfully tested by moving it to Turin by road. The next steps would be to compare our setup with the setup present in INRIM-Turin and to do a full characterization of the systematic errors.



# Zusammenfassung

In dieser Arbeit wurde ein transportabler Aufbau von einer Ytterbium-Atomquelle für eine optische Gitteruhr gebaut und charakterisiert [1] [2]. Alle Lasersysteme für das Kühlen und Fangen der Ytterbium-Atome sowie das Vakuumsystem befinden sich dabei auf einem transportablen optischen Tisch von 2x1 m<sup>2</sup> Größe.

Die Präparation des Atomensembles für die Spektroskopie beginnt mit dem Abbremsen der Atome in einem Zeeman-Abbremsler, gefolgt vom Fangen der Atome in den beiden MOT-Stufen und anschließendem Laden des optischen Gitters. Zum Abbremsen und für die Vorkühlung der Atome wird der starke  $^1S_0$ - $^1P_1$ -Übergang bei 399nm genutzt [3]. So werden 10<sup>6</sup> Atome auf etwa 1 mK gekühlt. Um sie erfolgreich in das optische Gitter laden zu können, müssen die Atome auf unter 50  $\mu$ K gekühlt werden. Dazu wird der schwache  $^1S_0$ - $^3P_1$ -Übergang bei 556 nm benutzt [4]. Die 10<sup>5</sup> in die zweite Kühlstufe umgeladenen Atome werden dort auf einige zehn  $\mu$ K gekühlt und können anschließen in das optische Gitter auf der magischen Wellenlänge geladen werden. Das verstärkte Laserlicht bei 759 nm im 1D-Intra-Vakuum-Resonator ergibt ein Gitterpotential von etwa 50  $\mu$ K. Es wurde eine Transfereffizienz aus der MOT in das optische Gitter von mehr als 25% gemessen.

Zunächst wurde der verbotene  $^1S_0$ - $^3P_0$ -Übergang bei 578 nm in der zweiten Kühlstufe mit Hilfe der "Chopped-MOT"-Methode angeregt. Durch Einschalten des optischen Gitters wurde die auf 300 kHz verbreiterte Linie auf 3 kHz verbessert. Diese sogenannte "Chopped-Lattice"-Methode unterdrückt die Dopplerverbreiterung, andere Effekte durch Licht und magnetische Felder bleiben jedoch erhalten. Durch Ausschalten des MOT-Lichts und der Magnetfelder werden die Atome vollständig im optischen Gitter gefangen. Hierdurch wurde die Linienbreite um einen weiteren Faktor 10 verringert.

Während dieser Arbeit wurden erste Beobachtungen des Uhrenübergangs von  $^{171}\text{Yb}$  an dieser Apparatur gemacht. Seitdem wurde der Aufbau im Rahmen einer anderen Promotion verbessert und der Übergang weiter vermessen [5]. Außerdem wurde die Transportfähigkeit der Apparatur durch einen Transport auf dem Straßenweg nach Turin erfolgreich getestet. Die nächsten Schritte sind eine vollständige Charakterisierung der Systematiken und ein Vergleich mit anderen Uhren in Turin.



# Contents

<b>1</b>	<b>Introduction</b>	<b>1</b>
<b>2</b>	<b>Overview About Optical Lattice Clocks</b>	<b>5</b>
2.1	The Optical Oscillator . . . . .	5
2.2	The Atomic Reference . . . . .	9
2.2.1	Ions as a Reference for Optical Clocks . . . . .	9
2.2.2	Neutral Atoms as References for Atomic Clocks . . . . .	11
2.3	The Femtosecond Frequency Comb . . . . .	14
2.4	Statistics of Atomic Frequency Standards . . . . .	17
2.5	Systematic Errors in Optical Lattice Clocks . . . . .	19
<b>3</b>	<b>Theory of Laser Cooling and Trapping</b>	<b>25</b>
3.1	The Radiation Force . . . . .	25
3.2	Cooling Atoms Using Laser Light . . . . .	26
3.2.1	Zeeman-Slowing . . . . .	27
3.3	Magneto-Optical-Trapping . . . . .	28
3.4	The Optical Lattice . . . . .	32
<b>4</b>	<b>The Experimental Setup</b>	<b>37</b>
4.1	Atomic Ytterbium . . . . .	37
4.2	The Vacuum System . . . . .	39
4.2.1	The Atomic Ovens . . . . .	42
4.3	The Magnetic Fields . . . . .	44
4.3.1	The Zeeman Slower . . . . .	45
4.3.2	The MOT Magnetic Fields . . . . .	45
4.4	The Laser Systems . . . . .	46
4.4.1	The Blue Laser System . . . . .	46
4.4.2	The Green Laser System . . . . .	47
4.4.3	The Lattice Laser System . . . . .	49
4.4.4	The Yellow Laser System . . . . .	52
4.5	The Intra-Vacuum Optical Resonator . . . . .	56
<b>5</b>	<b>Characterization of the Ultracold Atomic Source</b>	<b>61</b>
5.1	Loading of the First Stage MOT . . . . .	61
5.2	The Atom Number . . . . .	63
5.3	Temperature of Atomic Cloud . . . . .	67

---

5.3.1	The Optical Lattice . . . . .	68
<b>6</b>	<b>Spectroscopy on <math>^1S_0</math>-<math>^3P_0</math> Transition in <math>^{171}\text{Yb}</math></b>	<b>77</b>
6.1	The Experimental Sequence . . . . .	77
6.2	Spectroscopy on Untrapped Atoms . . . . .	79
6.3	Spectroscopy on Atoms Trapped in the Optical Lattice . . . . .	81
6.3.1	Spectroscopy in a Chopped-Lattice . . . . .	82
6.3.2	Spectroscopy in the Optical Lattice . . . . .	86
<b>7</b>	<b>Conclusion and Next Steps</b>	<b>91</b>
	<b>Bibliography</b>	<b>95</b>
	<b>ACKNOWLEDGEMENTS</b>	<b>105</b>

# Chapter 1

## Introduction

### History of Timekeeping

The physical quantity which can be measured nowadays with the highest accuracy is time [6]. Even in ancient times, our ancestors developed different instruments for measuring time, some of which had a high level of complexity. Time measurement instruments allowed for social and economic development in ancient societies, and helped providing us with more accurate dates of ancient events. It was at first, however, crucial for primitive societies to perceive the cyclic behavior in nature. Shorter cycles such as the sunrise and the sunset were easier to notice than the longer ones such as the seasons. But being able to measure the time of the day was only a part of the problem. The real challenge was the formation of a complete calendar. The fact that neither the earth has an integer number of rotations around itself when completing a full path around the sun, nor the moon has a whole number of periods in one year, made calendar keeping a complex issue. It was proven that societies who were able to develop a calendar, such as the Maya, have witnessed remarkable developments compared to other societies of their time [7]. The Mayan civil calendar for example adopted 18 months per year, each including 20 days and a closing month having five days. The result is a calendar covering 365 days per year. The clocks used in the past ranged from instruments depending on periodic phenomena already existing in nature such as the sun movement, or others depending on man made oscillators.

The oldest clocks used to measure time spans over a day are the sundials. These clocks were first developed by the Sumerians in Babylonia and are formed of a gnomon (an object producing a shadow), which throws its shadow on a horizontal plane with markings showing the time of the day. The sexagesimal number system (based on 60) that was present at that time, and that was used to read the time from sundials has even influenced the way we subdivide the day into hours, minutes, and seconds. But the Sumerians weren't able to find a solution for the crucial problem that sundials at that time faced. It is the variability at which the shadow moves throughout the day, and even throughout the seasons. A solution was first found by Arab astronomers. The trick was to mount the gnomon parallel to the earth's axis of rotation. This produces a constant angular motion of the shadow projected on the

horizontal plane. With time, sundials transformed into highly complex instruments with an uncertainty of 24 seconds [7].

Many clocks were also developed which don't depend on celestial bodies. One of the first clocks with a self-built oscillator is the so know water clock. But the breakthrough came with the invention of the mechanical clocks in the seventeenth century, namely the pendulum clocks. Christiaan Huygens was the first to construct a pendulum, through which an error of 1 minute a day has been achieved [8]. Pendulum clocks were refined over the years by changing the geometries and decreasing the friction. Such clocks with accuracies below a hundredth of a second a day served as the standard for many astronomical observations during the last quarter of the nineteenth century [8]. A nice introduction about the history of timekeeping can be found in [7], where clocks based on electronic oscillators are also discussed. Through the centuries, timekeeping instruments made their way from the cosmos to the quantum. Nowadays, the time is defined by atomic standards.

### The Atomic Standard

The SI unit of time is the second which is defined by the Cs fountain clock. In such clocks, the hyperfine transition  $F=3$  to  $F=4$  of the ground state (i.e. the  $^2S_{1/2}$  state) is used as the clock transition. The corresponding transition frequency is 9192631770 Hz. Thus, a second is defined to be equal to the duration of 9192631770 periods of the microwave radiation which drives the hyperfine transition. The latest fountain clocks are able to preserve time with an inaccuracy of  $4 \times 10^{-16}$  [9] [10]. This is already a very accurate result, but optical standards promise with a result that is better by two orders of magnitude. In the past years a lot of improvements were made to the Cs fountain clock. However, lowering the inaccuracy to below  $4 \times 10^{-16}$  is becoming more and more challenging. This is due to two factors. The fact that accuracy is limited by the fractional instability  $\sigma_i$  results in statistical limitations. The fractional instability is expressed as follows [11]

$$\sigma_i \propto \frac{\Delta\nu}{\nu_0} \sqrt{\frac{\tau_m}{N\tau}} \quad (1.1)$$

Here,  $\Delta\nu$  is the width of the transition frequency centered at  $\nu_0$ ,  $\tau_m$  is the measurement time,  $N$  is the number of quantum absorbers, and  $\tau$  is the averaging time. Reducing the statistical uncertainty of a clock by a factor of one thousand requires an averaging time of  $10^6$ s. This implies that lowering the inaccuracy of Cs clocks below  $10^{-17}$  with current instabilities ranging between  $2 \times 10^{-13}$  and  $1 \times 10^{-14}$  [9] [10] is quite difficult. In addition to the statistical limitations, the systematic errors serve as the second limiting factor. Systematic errors range from technical such as the microwave cavity leakage, to fundamental issues like the blackbody radiation and the cold collision shifts.

The next generation atomic clocks, known as optical clocks, seem to provide an accuracy of two orders of magnitude better. Optical clocks use clock transitions in

the optical instead of the microwave regime, thus providing a remarkable decrease in the instability. The factor  $\Delta\nu/\nu_0$  for optical transitions is  $10^{-4}$  to  $10^{-5}$  smaller than that for microwave transitions in Cs [12] [13]. The increase in accuracy opens the door for scientists to test theories and quantities which they were not able to explore so far. Developments in this field have been done on two main groups of clocks, where the first is based on neutral atoms while the second has ions as a reference. The ion candidates have been taking the lead in the past few years before the neutral optical clocks made a boost in performance recently. The references based on neutral atoms and ions have different characteristics. A common goal however between the different groups is to improve their setups, by better understanding and controlling the different sources of uncertainties. The groups working at JILA and PTB with neutral  $^{171}\text{Yb}$  and neutral  $^{87}\text{Sr}$ , respectively, were able recently to demonstrate clocks with instabilities that are about one order of magnitude better than the best ion candidates to date [14] [15] [16] [17]. The challenges faced by each candidate, in addition to the recent developments and measurements, will be demonstrated in chapter 2 of this thesis.

## The SOC Project

My Ph.D. thesis was devoted to the development of a transportable ultracold Ytterbium atomic source for an optical lattice clock, in the research group of Professor Axel Görlitz at the Heinrich-Heine-Universität Düsseldorf. In the time frame of my work, a Diploma and a Master theses in addition to two Bachelor theses were carried out. A second PhD student also joined the project during this time. The clock laser and the frequency comb serving as the oscillator and the counter are also developed and operated at the Heinrich-Heine-Universität Düsseldorf by the group of Professor Stephan Schiller. This Yb clock is one prototype of several clocks developed by other research institutions in Europe under the umbrella of the "Space Optical clocks" (SOC) project. The proposal was submitted in 2004 to ESA, and it aims at developing transportable lattice optical clocks to be operated at the ISS. The first stage of this project ended in 2010 and in 2011 the SOC2 project followed. The SOC2 project is a follow up for the SOC project with the aim to start shortening the distance between research and industry in this field, and reach inaccuracies and instabilities that are better than what is obtained by microwave clocks by a factor of 100 and a factor of 10, respectively [18]. This will be coupled with the development of laser systems, atomic packages and electronics that require less space and power and have a reduced mass to enhance the transportability. Two types of clocks were developed within the SOC and SOC2 projects, namely optical clocks based on neutral Ytterbium and Strontium atoms. The goal is to demonstrate the functionality of those clocks by the end of the SOC2 project. Thus, the plan is to transport the Sr clock from the University of Birmingham to PTB, while the Yb clock has been transported from Heinrich-Heine-Universität Düsseldorf to INRIM in Torino. The transportable clocks will be then compared to stationary ones that are located at the mentioned destinations. Other experiments that would add to the value of those prototypes would include operating the clocks at different altitudes. Apart

from the technical aspect of this experiment, the altitude difference would serve to measure the gravitational redshift of the clocks and the Local Position Invariance in the earth's gravitational field [18]. Presently, the collaborating research institutions and industries are:

- Heinrich-Heine-Universität Düsseldorf, Germany
- Physikalisch-Technische Bundesanstalt, Germany
- Leibniz Universität Hannover, Germany
- Observatoire de Paris, France
- Università degli Studi di Firenze, Italy
- Istituto Nazionale di Ricerca Metrologica, Torino-Italy
- University of Birmingham, United Kingdom
- National Physical Laboratory Teddington, United Kingdom
- TOPTICA Photonics AG, Germany
- Kayser-Threde GmbH, Germany
- EADS Astrium Friedrichshafen, Germany
- Menlo Systems GmbH, Germany
- Kayser Italia Srl, Italy
- Université de Neuchâtel, Switzerland
- Centre Suisse d' Electronique et de Microtechnique, Switzerland
- Ecoles Polytechniques Fédérales Lausanne, Switzerland

Why is it important to bring optical clocks to space?! The field of frequency measurement is evolving in a fast pace and present clocks have reached very high precisions. Further improvements however require taking more care about the clock systematics and error sources, which are discussed in section 2.5. One of these errors is the so-called gravitational shift resulting from the earth's gravitational field. With a contribution of about  $10^{17}$  to the uncertainty budget of systematic effects, the gravitational shift is a serious limitation facing ultra-precise optical clocks. The solution is an optical clock operating in space where the gravitational field becomes relatively negligible. The proposals and publications related to the SOC project and the work done at the different institutions can be found on the specially tailored website [http://www.exphy.uni-duesseldorf.de/optical\\_clock](http://www.exphy.uni-duesseldorf.de/optical_clock).

## Chapter 2

# Overview About Optical Lattice Clocks

Atomic clocks constitute mainly of 3 parts; namely the source, reference, and counter (see fig. 2.1). The reliability, stability, and precision of clocks has evolved enormously throughout the years, but the building blocks stayed the same. The technological advancements that took place in the past century opened the way for the development of optical atomic clocks.

Optical clocks use an ultrastable laser as the source for the clock setup. The laser's freedom to drift in a certain range is controlled by referencing it to a narrow atomic transition. A feedback loop keeps the laser at the resonant frequency of the respective atomic transition. The atomic reference can constitute of ions or neutral atoms and of different atomic species. Although the idea is not new, it was hard before the year 1990 to develop such clocks because a counter that can deal with optical frequencies was missing. This problem was solved with the invention of the frequency comb, which is able to measure frequencies ranging from the IR to the UV regime [19,20]. Since then, optical clocks started witnessing a fast development which will most probably keep its pace in the coming years.

### 2.1 The Optical Oscillator

As already mentioned in the introduction of this chapter, lasers are used as a source for optical clocks, with the requirement of having a low frequency and phase noise. A wide variety of laser systems exists nowadays on the market, ranging from semi-conductor and solid-state lasers (i.e. diode lasers and Ti:Sapphire lasers) to Dye lasers and fiber lasers. For the development of space optical clocks, semi-conductor lasers have gained the highest popularity [18]. The reason is their compactness, large wavelength tuning, and their moderate price.

In the middle of the last century, Schawlow and Townes showed that optical masers (nowadays known as lasers) have a lower limit on their linewidth  $\Delta\nu_{Schawlow-Townes}$

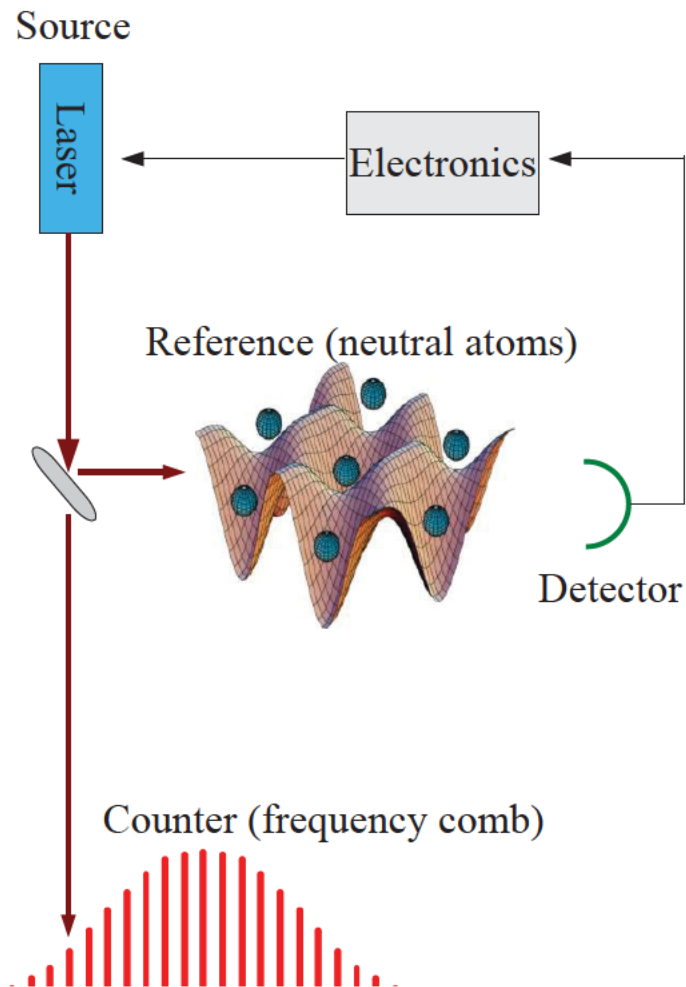


**FIGURE 2.1:** This figure shows the different components of an optical lattice clock. The optical oscillator is stabilized by the atomic reference, in this case it is the neutral atoms trapped in the optical lattice. The frequency of the stabilized laser light is then evaluated (counted) by the frequency comb.

derived to be [21]

$$\Delta\nu_{Schawlow-Townes} = \frac{4\pi h\nu(\Delta\nu)^2}{P_{out}} \quad (2.1)$$

where  $\Delta\nu$  is the half width of the laser's resonator resonances and  $P_{out}$  is its output power. The derivation of this finite linewidth was based on thermal noise considered for masers and is a result of spontaneous emission in the laser medium. The outcome is then amplitude and phase fluctuations. While the amplitude noise is damped because of the gain saturation, phase noise undergoes a random walk and induces a lower limit on the linewidth. A review of Schawlow and Townes' formula was done in 2010 based on quantum noise [22]. The modified formula is

$$\Delta\nu_{laser} = \frac{h\nu(1 + \alpha^2)l_{tot}T_{oc}}{4\pi t_{rt}^2 P_{out}} \quad (2.2)$$

with  $l_{tot}$  being the total resonator losses,  $T_{oc}$  the output coupler transmission, and  $t_{rt}$  the round-trip time. The extra factor  $(1 + \alpha^2)$  is only taken into consideration when dealing with semi-conductor lasers. That's due to the amplitude and phase coupling in a semi-conductor medium. The linewidth is then influenced by this behavior which demonstrates itself in Eq. 2.2 through the linewidth enhancement factor  $\alpha$ . As already mentioned, equations 2.2 and 2.1 give a lower limit for the linewidth. However, in reality, we have noise sources which were not taken into consideration when deriving these formulas. The noise sources broaden the linewidth of the laser far beyond the theoretical value. In the past years a lot of research was going on to develop stabilization methods which would help reducing the linewidth. The most common one for optical metrology is using high finesse ultra-stable cavities and locking the laser on the cavity signal. The two most known locking techniques used for this purpose are the Hänsch-Couillaud and the Pound-Drever-Hall methods (see section 4.4.3).

### Cavities for optical metrology

In this section, I will discuss the stability factors relevant for ultrastable cavities. Many new models and cavity designs were developed in the past few years [23] [24]. The techniques differ but the goal is one. High finesse cavities are needed that are influenced by the factors listed below (an indepth description can be found in [25]):

- The absorption factor by the mirrors has a direct affect on the finesse. The reflected and transmitted intensities can then be written in terms of the absorption  $A$ , the transmission  $T$ , and the Airy function  $A(2\pi\nu/\Delta\nu_{FSR})$  as follows

$$\frac{I_r}{I_i} = \left[1 - \frac{A}{A+T}\right]^2 [1 - A(2\pi\nu/\Delta\nu_{FSR})] \quad (2.3a)$$

$$\frac{I_t}{I_i} = \left[1 - \frac{A}{A+T}\right]^2 [A(2\pi\nu/\Delta\nu_{FSR})] \quad (2.3b)$$

So for high finesse cavities, mirrors with a very low absorption coefficient are required. Typical values are on the order of  $10^{-5}$ . For a cavity which satisfies the impedance matching condition, the reflectivity of the mirrors would be 0.99999. This results in a finesse of 300,000 which is a typical value for ultra-low expansivity glass (ULE) cavities.

- The thermal motion of molecules in the surrounding environment and the pressure waves result in a force on the cavity mirrors. This leads to a linewidth broadening which is directly proportional to the change in the index of refraction. To avoid this, a cavity is placed in a vacuum chamber. The ULE cavity used to stabilize the Yb clock laser at the University of Düsseldorf is mounted in a vacuum chamber, pumped down to  $3.5 \times 10^{-8}$  mbar by a ion-gitter pump [18].
- Another environmental factor that plays a big role for the stability of reference cavities is the temperature. The change in length due to temperature variations can be described by the following expression

$$\Delta L = \alpha L \Delta T \quad (2.4)$$

where  $L$  is the length of the cavity,  $T$  is the temperature, and  $\alpha$  is the coefficient of thermal expansion (CTE). ULE is a material which is commonly used to construct ultra-stable cavities due to its low thermal expansion  $\alpha = 0 \pm 30 \text{ ppb}/^\circ\text{C}$  at temperatures between  $5^\circ\text{C}$  and  $35^\circ\text{C}$ , according to Corning Advanced Optics. In addition to the material used, the cavity housing needs also to be temperature stabilized. In our case, this is done by shielding the internal part of the aluminum box enclosing the cavity with copper and temperature stabilizing it with peltier elements.

- The next factor which has to be fought against are the forces acting on the cavity chassis. They can be separated into two components, namely the one due to the gravitational acceleration and the other is a compressive force exerted by the support acting against gravity. Several designs came up to reduce these effects. Cavities went beyond the cylindrical form and spherical as well as cubic ones were tested. A spherical cavity developed recently by Bergquist et al. reached a minimum acceleration sensitivity of  $1.3 \times 10^{-11}/\text{g}$ , where a feed-forward correction was included in this setup [26]. The spherical spacer is fixed at two points on the sphere's diameter, and the angles are chosen such that the compressive force on the cavity is minimized. On the other hand, Webster et al. presented a cubic shaped cavity which demonstrated a passive acceleration sensitivity of  $2.5 \times 10^{-11}/\text{g}$  [27]. Here, the spacer is supported at four symmetrical points about the optical axis in a tetrahedral geometry. Both groups used the finite element analysis (FEA) method to calculate the most effective supporting positions to minimize the cavity's sensitivity to the previously mentioned forces.

The clock laser and its stabilization system used for our measurements was developed by the research group of Professor Stephan Schiller at Heinrich-Heine-Universität Düsseldorf and it will be discussed in section 4.4.4.

## 2.2 The Atomic Reference

An atomic reference used for an optical atomic clock can be based on ions or neutral atoms. In both cases, the atoms have to be prepared such that they are confined at a certain position, where they are supposed to intersect with the clock laser radiation and with a minimal motional behaviour. The motion of atoms would induce a Doppler broadened line which would limit the accuracy that the clock can reach. I will describe here the different trapping methods used for ions and neutral atoms as well as the pros and cons of both references.

### 2.2.1 Ions as a Reference for Optical Clocks

Groups working on frequency metrology using ions were the pioneers in developing ultra-stable optical clocks. The reason is the relatively uncomplicated setups available to trap ions for long times. Several species are competing for the highest accuracy and stability, some of which are  $\text{Yb}^+$ ,  $\text{Al}^+$ ,  $\text{Hg}^+$ ,  $\text{Ca}^+$ ...etc [14] [28] [29] [30] [31] [32] [33]. But before discussing the differences between the existing clocks based on the different ions species, I will show shortly the techniques used to trap these ions.

#### Ion trapping techniques

Ions used as a reference for the clock optical oscillator are produced by ionizing an atomic gas heated in an oven. In other words, the ions have initially high velocities which makes it impossible to trap them directly. Therefore, they have to be laser cooled. For this purpose, a fast transition is chosen. For  $\text{Yb}^+$ ,  $\text{Hg}^+$ ,  $\text{Sr}^+$  and  $\text{Ca}^+$ , the  $^2S_{1/2} \rightarrow ^2P_{1/2}$  transition is used. More details on laser cooling can be found in the next chapter. The trapping process of ions is done however with an AC electric field instead of laser light.

If we consider an ion in a static electric field, it will be under the influence of a potential with a saddle form. So the ion escapes through the sides of the potential and the trapping mechanism would not work. Therefore, traps with combinations of DC and AC electric fields as well as magnetic fields were developed for the sake of trapping ionized particles. For optical clocks, the Paul trap was the standard trap for many years. It is named after its inventor, the Nobel laureate Wolfgang Paul. Let us consider a 3-dimensional trap geometry constituting of a hyperbolic ring electrode enclosed on both sides with two hyperbolic end caps facing each other. An AC voltage source is connected to the trap's electrodes such that a high frequency voltage, together with a DC component, forms between the ring and the two end caps. If the conditions of a stable trap are met, ions will oscillate within a certain

region from the center of the trap. Thus, the trapping procedure is successful.

Several trap geometries have been developed to trap ions for optical clocks and quantum computing. The most popular one being the linear Paul trap. Its advantages are a low signal to noise when detecting fluorescent light from trapped ions and a relatively flat axial potential which allows for multiple ion trapping. Different geometries of the classical Paul trap exist nowadays in modern trapped ions experiments such as planar Paul traps and ring traps. These geometries will not be discussed here but a detailed explanation can be found in [7].

### The present status of optical clocks based on ions

The best clock measurement to-date using ions was achieved by comparing two  $\text{Al}^+$  clocks in NIST [14]. The interrogated  $^{27}\text{Al}^+$  ions were cooled sympathetically by different ion species in each of the clocks. While the first used  $^9\text{Be}^+$  ions inside a linear Paul trap, the second made advantage of  $^{25}\text{Mg}^+$  ions. The advantage of  $\text{Mg}^+$  over  $\text{Be}^+$  ions is its smaller mass mismatch with the interrogated  $\text{Al}^+$ , which makes laser cooling more efficient. Moreover, the  $\text{Mg}^+$  ion serves to detect the quantum state of the  $\text{Al}^+$  ion. The measurement yielded a fractional frequency difference of  $-1.8 \times 10^{-17}$  and have demonstrated a relative stability of  $2.8 \times 10^{-15} \tau^{-1/2}$ .

The best ion-based clock measurement relying on two different atomic species was also achieved at NIST. The measurement was done by comparing two optical clocks, the first based on  $^{27}\text{Al}^+$  and the second on  $^{199}\text{Hg}^+$  [28]. In mercury, the short living  $^2S_{1/2} \rightarrow ^2P_{1/2}$  transition at 194 nm is used to cool the  $^{199}\text{Hg}^+$  ion down to the Doppler limit. While the atom is trapped in a quadrupole trap, clock measurement is done on the 1.8 Hz narrow  $^2S_{1/2} \rightarrow ^2D_{1/2}$  transition at 282 nm. On the other hand, the aluminum ion is coupled to a  $^9\text{Be}^+$  in the trap and cooled via the sympathetic doppler cooling method [34]. Laser radiation at 266 nm is used to excite the 0.008 Hz narrow  $^1S_0 \rightarrow ^3P_0$  transition. The frequency ratios of both clocks gave a fractional instability of  $5.2 \times 10^{-17}$ . The systematic uncertainties of the aluminum and the mercury clocks are  $2.3 \times 10^{-17}$  and  $1.9 \times 10^{-17}$ , respectively. The uncertainties in the Al ion clock were dominated by the micro- and secular motions resulting from the Paul trap's dynamics and the high Doppler limit. The second-order Doppler effect is easier to control for mercury ions due to their higher mass which results in a stronger resistance to the ambient electric fields. This explains the lower systematic uncertainty associated with the mercury single ion clocks.

Another relevant species for single ion optical clocks is ytterbium. The pioneers working on ytterbium ions are the groups from PTB (Physikalisch-Technische Bundesanstalt) and NPL (National Physical Laboratory). Here, two transitions are being studied for clock operation. The first is the  $^2S_{1/2} \rightarrow ^2D_{3/2}$  electric quadrupole transition [29] [30], and the second is the  $^2S_{1/2} \rightarrow ^2F_{7/2}$  electric octupole transition [31] [32]. Radiation at 370 nm is used to excite the  $^2S_{1/2} \rightarrow ^2P_{1/2}$  short-living transition, to cool the single ion which is trapped in a cylindrically symmetric Paul trap. The

3.1 Hz electric quadrupole transition at 436 nm has proven to be a good choice with easy-to-handle systematic uncertainties. This is because alkaline-earth-metal like ions have a relatively low sensitivity to external electric fields and to blackbody radiation. In 2005, two clocks operating on single  $^{171}\text{Yb}^+$  ions excited at the electric quadrupole transition were compared at PTB and the result was a relative frequency shift of  $3.8 \times 10^{-16}$  [35]. Further investigations followed where the relevant shifts on the transition line were measured. One of the most important for such clocks is the effect of the electrostatic stray field gradient in the trap on the electric quadrupole moment in the atom. It was shown that the quadrupole shift can be eliminated with a high accuracy when applying appropriate measurement schemes [29]. But that's only one part of the story. Ytterbium ions have actually another state which can be used for a clock transition. In fact, the  $^2F_{7/2}$  state has several advantages over the  $^2D_{3/2}$  state. The first thing is the  $10^{-9}$  Hz broad linewidth which compares to a linewidth of 1 Hz in electric quadrupole transitions. Thus, a lower instability is expected. Another advantage is the smaller electric quadrupole moment. The result is a smaller quadrupole shift due to electric field gradients. A recent work done at PTB on this transition showed a total fractional uncertainty of  $8 \times 10^{-16}$  [31]. The relevant shifts on the  $^2S_{1/2} \rightarrow ^2F_{7/2}$  transition are the AC Stark shift and the second-order Zeeman shift induced by the probe light beam and the magnetic fields, respectively. More on systematic frequency shifts in optical clocks based on ytterbium ions and how to control them can be found in [36] and [31].

Optical clocks referenced to  $^{40}\text{Ca}^+$  also proved to be good candidates for time metrology. Calcium already reached a relative uncertainty of  $2.4 \times 10^{-15}$  on the 0.14 Hz  $^2S_{1/2} \rightarrow ^2D_{5/2}$  transition [33]. Still more can be done to reduce the systematic uncertainties such as the AC Stark shift and the blackbody shift. This would bring the uncertainty down to the  $10^{-16}$  level.

The species discussed above are not the only candidates for optical clocks. Strontium and indium ions are also being investigated and have shown promising results. People interested in these two atomic species can refer to [37] [38].

### 2.2.2 Neutral Atoms as References for Atomic Clocks

The development of atomic clocks based on neutral atoms have been slower than its single ion competitor. Only recently did the quality of such clocks rise to start meeting the long-awaited expectations. As it is shown in equation 1.1, the clock instability is proportional to  $1/\sqrt{N}$ . Thus, the big sample of atoms, having  $N$  atoms that are illuminated at once by the oscillator, provide an improved stability and a relatively high signal to noise ratio compared with the ion-referenced candidates.

The principle of optical lattice clocks was first introduced in 2003 by Katori et. al.. The main benefit is to overcome the limitations imposed by the quantum projection noise and the long averaging times on single-ion operating optical clocks. Thus, it was proposed by Katori to trap millions of neutral atoms in a light field

Ion	Clock Transition (nat. linewidth)	$\lambda$ (nm)	Sys. Uncertainty	Fract. Instability
$^{27}\text{Al}^+$	$^1S_0 \rightarrow ^3P_0$ (0.008Hz)	266	$8.6 \times 10^{-18}$	$2.8 \times 10^{-15} / \sqrt{\tau}$
$^{199}\text{Hg}^+$	$^2S_{1/2} \rightarrow ^2D_{5/2}$ (1.8Hz)	282	$1.9 \times 10^{-17}$	$3.9 \times 10^{-15} / \sqrt{\tau}$
$^{171}\text{Yb}^+$	$^2S_{1/2} \rightarrow ^2D_{3/2}$ (3.1Hz)	436	$5 \times 10^{-16}$	$4.2 \times 10^{-15} / \sqrt{\tau}$
$^{40}\text{Ca}^+$	$^2S_{1/2} \rightarrow ^2D_{5/2}$ (0.14Hz)	729	$2.4 \times 10^{-15}$	$2.9 \times 10^{-13} / \sqrt{\tau}$

**TABLE 2.1:** This table lists the important values for the most relevant ion-based optical clocks. In addition to the atomic species, the clock transitions, the natural linewidths, and the exciting wavelengths are shown. The last two columns list the fractional systematic uncertainties and the fractional instabilities [14] [28] [29] [33].

potential and interrogate this sample of atoms at once. If the light field potential is designed carefully, the perturbations of the light field on the interrogated atoms can be cancelled out to below  $10^{-17}$  [13]. The detailed processes of cooling the atoms and afterwards confining them in an optical lattice will be explained in the following chapters. This section will be dedicated to show the cutting-edge experiments and modern results of clocks operating on different neutral atomic species.

I will explain the working principles of a neutral atom optical clock by using Yb as an example. For ytterbium, as well as for atomic mercury and strontium, clock measurements have been performed on fermionic as well as on bosonic isotopes. The alkaline-earth-like atoms have the  $^1S_0 \rightarrow ^3P_0$  forbidden transition which is suitable as a clock transition. In fermions, the  $^3P_0$  state is only partly forbidden due to hyperfine mixing and that corresponds to a natural linewidth that is smaller than 10 mHz [39]. This makes fermions a better candidate than the bosonic isotopes. Nevertheless, the usage of bosonic isotopes as a reference was enabled by applying a DC magnetic field. This mixes a fraction of the  $^3P_1$  state into the  $^3P_0$ , thus allowing single-photon excitation on the  $^1S_0 \rightarrow ^3P_0$  transition [40]. A clock measurement was performed at NIST on the abundant  $^{171}\text{Yb}$ , by comparing an Yb with a Ca atomic clock, which showed an uncertainty of  $3.4 \times 10^{-15}$  [15] on the absolute frequency. The same Yb clock was compared recently with another clock of the same species. The first results have shown an unprecedented Yb atomic clock instability, reaching the  $10^{-18}$  level after an averaging time of 7 hours [16].

Fermionic ytterbium was also investigated at Kriss in Korea and at NMIJ in Japan. However, the uncertainty due to the systematic shifts is still relatively high compared to the results that were reached by the group in NIST. The Korean group have shown

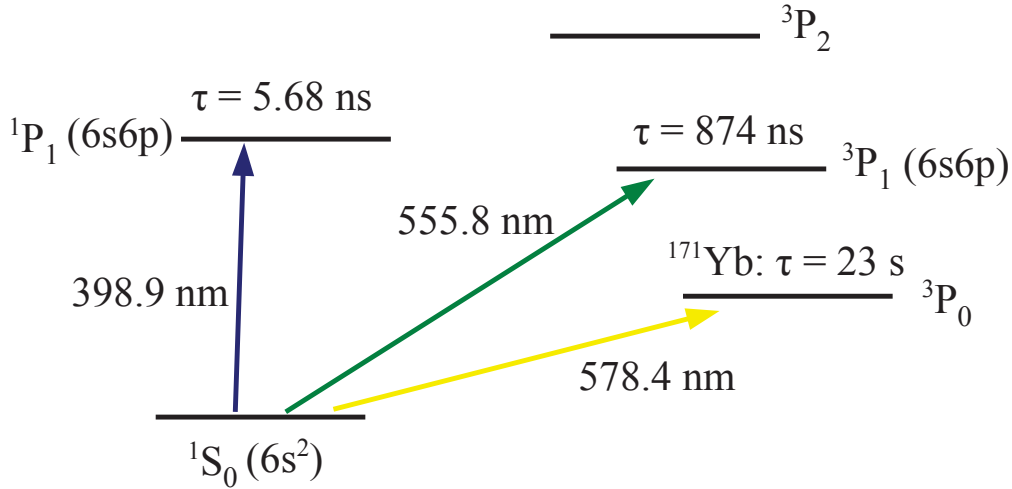


**FIGURE 2.2:** A simplified energy level scheme of atomic ytterbium showing the yellow clock transition, the green post-cooling transition and the blue pre-cooling transition. A more detailed graphic can be found in fig 4.1.

lately an uncertainty of  $1.5 \times 10^{-14}$  [41].

Clock operation on the forbidden  $^1S_0 \rightarrow ^3P_0$  transition in bosonic ytterbium has also been done by use of magnetically induced spectroscopy [42]. A 1.3 mT static magnetic field together with the  $300 \text{ mW/cm}^2$  probe intensity result in a 5 Hz Rabi frequency. This line with the Fourier limited linewidth of 10 Hz is then used to reference the clock laser. For the  $^{174}\text{Yb}$ , the absolute frequency was measured with an uncertainty of  $1.5 \times 10^{-15}$ . Systematic uncertainties were determined by comparing the  $^{174}\text{Yb}$  clock with the  $\text{Hg}^+$  time standard. This was done by locking a femto-second frequency comb on the latter clock and measuring the beat signal with the Yb clock. The result is an uncertainty of  $3 \times 10^{-16}$ , where the new challenge is controlling the shift induced by the applied magnetic field. The performance of atomic clocks referenced to bosonic neutral Yb atoms is still lagging behind the fermionic competitor.

The strongest competitor for ytterbium is strontium. Several groups in the world, such as in SYRTE, JILA and PTB to name a few, have chosen it as the atomic species to be used as a clock's reference, and the results show an excellent agreement [43] [44] [45] [17]. Strontium has a very similar internal structure as ytterbium. Pre-cooling is done on the  $^1S_0 \rightarrow ^1P_1$  fast transition at 461 nm. The intercombination line  $^1S_0 \rightarrow ^3P_1$  at 689 nm is then used to cool the atoms down as a pre-stage for trapping in the optical lattice at 813.42 nm [46]. A recent work at JILA has demonstrated a new record in Sr clock stability and accuracy. Two  $^{87}\text{Sr}$  optical clocks were used for this measurement. The control and limitation of the atomic-interaction-induced frequency shift as well as the BBR Stark shift are the main factors behind the measured accuracy of  $6.4 \times 10^{-18}$  [17]. This has been done by increasing the optical lattice volume, building in-situ BBR probes inside vacuum and enclosing the vacuum chamber with a thermal isolation. The stability of the setup is similar to

that provided by the recent  $^{171}\text{Yb}$  optical clock.

In Tokio, clock measurements were also done on  $^{88}\text{Sr}$  atoms. The revolutionary part in this experiment is the trapping process which took place in a 3-D optical lattice [46]. The advantage is the reduction of the collisional shift whose uncertainty is dependent on the atom number fluctuation in a single lattice site on one hand, and the tunneling of atoms between different lattice sites on the other hand. The  $^1S_0 \rightarrow ^3P_0$  transition is then observed by applying a 2.34 mT magnetic field. This, together with a clock laser intensity of  $400 \text{ mW/cm}^2$ , induces a rabi frequency of 9 Hz. The systematic uncertainties were determined by referencing the clock with a  $^{87}\text{Sr}$  1-D lattice optical clock. As it is the case for Yb referenced optical clocks, fermions have proven to be a better candidate to-date than the bosonic isotopes.

Although Sr and Yb are the most popular atomic species used for optical clocks based on neutral atoms, a group at SYRTE in Paris introduced a few years ago a new candidate for such clocks. Through building an optical clock based on neutral mercury atoms, S.Bize et. al. opened the way for Hg to compete for the ultimate optical clock, taking into consideration the low blackbody shift that this candidate offers. The clock based on Hg is still young in comparison to its Sr and Yb competitors. However, frequency measurements with a fractional frequency instability of  $5.3 \times 10^{-15} / \sqrt{\tau}$  have already been demonstrated on the 100 mHz narrow  $^1S_0 \rightarrow ^3P_0$  transition [47]. In contrast to clocks working with Sr and Yb, the Hg clock has only one cooling stage at the 1.3 MHz narrow  $^1S_0 \rightarrow ^3P_1$  transition. The difficulty arises in producing the required cooling light at 253.7 nm. Due to the unavailability of direct laser sources, this wavelength was produced by frequency doubling light at 1014.8nm from a Yb:YAG thin disk laser, twice. The MOT is loaded from a 2-D MOT and trapping follows by a 1-D vertical optical lattice [48]. The relatively low atomic polarizability in Hg raises the need for a high power source in order to be able to trap the atoms. The solution was integrating a power-enhancement cavity which provided in the end a potential depth which is 22 times the recoil energy  $E_R$ . The ultrastable clock laser was then locked on the clock  $^1S_0 \rightarrow ^3P_0$  transition. This was the first time where a laser is locked on a UV transition line [47].

## 2.3 The Femtosecond Frequency Comb

In the 1990's, Theodor W. Haensch and John L. Hall made a big contribution to laser based precision spectroscopy, including the development of the optical frequency comb technique. The frequency comb serves as the counter in optical atomic clock setups. It makes use of a mode locked laser's spectrum to identify the frequency of the clock laser. Optical frequency combs opened the way in the past few years for a wide range of interesting physical and technological advancements. In addition to the role that frequency combs played in the development of optical atomic clocks, these devices found their way recently also into astrophysics where ultra-high precision spectroscopy is needed to observe fade planets close to nearby stars [49]. A wide

Ion	Clock Transition (nat. linewidth)	$\lambda(\text{nm})$	Sys. Uncertainty	Fract. Instability
$^{171}\text{Yb}$	$^1S_0 \rightarrow ^3P_0(0.044\text{Hz})$	578	$3 \times 10^{-16}$	$3.2 \times 10^{-16} / \sqrt{\tau}$
$^{174}\text{Yb}$	$^1S_0 \rightarrow ^3P_0(-)$	578	$1.5 \times 10^{-15}$	$1 \times 10^{-15} / \sqrt{\tau}$
$^{87}\text{Sr}$	$^1S_0 \rightarrow ^3P_0(0.008\text{Hz})$	698	$6.4 \times 10^{-18}$	$3 \times 10^{-16} / \sqrt{\tau}$
$^{88}\text{Sr}$	$^1S_0 \rightarrow ^3P_0(-)$	698	$2 \times 10^{-15}$	$2.3 \times 10^{-14} / \sqrt{\tau}$
$^{199}\text{Hg}$	$^1S_0 \rightarrow ^3P_0(0.00014\text{Hz})$	266	-	$5.4 \times 10^{-15} / \sqrt{\tau}$

**TABLE 2.2:** Here is a list showing the most important optical clocks based on neutral atoms [16] [42] [17] [46] [47].

range of applications that require frequency combs in the infrared and ultraviolet regimes also benefited from this development, such as molecular spectroscopy [50] and nuclear clocks [51], just to name a few. In this section, I will explain in a simplified way the mode of operation of frequency combs in the optical regime and their relevance to optical atomic clocks. The cited literature can serve for a more in-depth reading.

Mode locked lasers generate ultrashort optical pulses by establishing a fixed phase relationship across a broad spectrum of frequencies. Mode locking requires a method which results in higher gain for short pulses compared to continuous waves. Nowadays, passive mode locking is used for this purpose due to its ability to produce the shortest pulses. The ultrashort optical pulses are mostly generated by Kerr-lens mode-locked Ti:sapphire lasers. The frequency comb is obtained by performing a Fourier series expansion on the train of optical pulses (see [52] for a detailed derivation). The spectrometer which is capturing the pulses is not able to resolve those pulses. Thus, interference inside the spectrometer occurs. The interference is constructive for frequencies which are a multiple of the repetition rate  $f_r = 1/\tau$ , and destructive otherwise. The role of the pulse phase in this interference process is shown in fig. 2.3. The result is a spectrum of well defined frequency lines forming the frequency comb. The separation between two neighbouring frequency lines is given by the repetition rate of the laser. Therefore, we can find the optical frequency  $\nu_n$  of a certain comb line by applying the following relation [53]

$$\nu_n = n f_r + f_0 \quad (2.5)$$

where  $n$  indexes the comb line and  $f_0$  is the comb offset caused by the pulse-to-pulse phase shift.

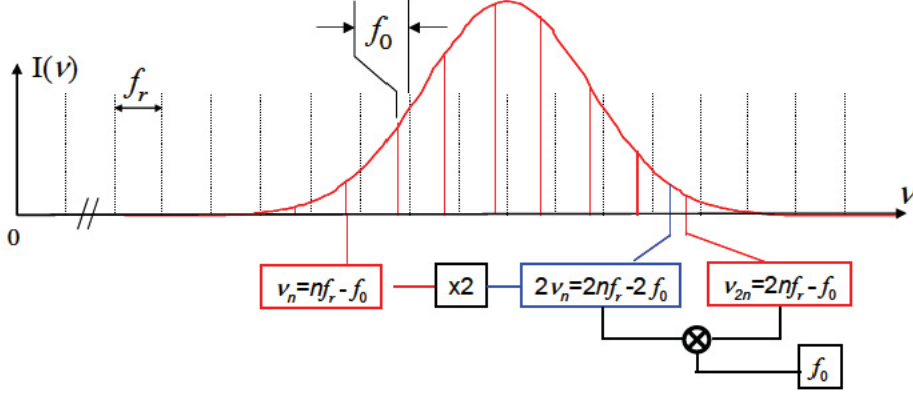


**FIGURE 2.3:** This figure shows a basic spectrum of a frequency comb. The optical spectrum of the frequency comb is plotted in red. The process of extracting the values of  $f_0$  and  $\nu_n$  is also shown [53].

According to the above equation, doing an absolute frequency measurement requires two RF measurements. The first is to determine  $f_r$ . This is easily done by measuring the intensities as a function of time using a fast photodiode. The second measurement is to determine  $f_0$ . The fact that  $f_0$  is related to the phase and not to the intensity makes its measurement harder. One method to determine  $f_0$  is to create an optical spectrum that spans one octave, i.e. the highest frequency in the spectrum is double that of the lowest frequency. By frequency doubling the lowest frequency in the spectrum, it gets a value which is approximately equal to that at the second side of the octave. Through interfering the two lines,  $2f_n$  and  $f_{2n}$ , and by measuring the beat, the following result for  $f_0$  is obtained [53]

$$2f_n - f_{2n} = 2(nf_r + f_0) - (2nf_r + f_0) = f_0 \quad (2.6)$$

Having  $f_r$  and  $f_0$ , the frequency  $\nu_n$  can be found. The well defined comb parameters serve to measure optical frequencies of optical atomic clocks through taking the beatnote of the clock laser radiation and that of the frequency comb by superimposing both sources on a photodetector.

## 2.4 Statistics of Atomic Frequency Standards

The head of this section appeared in 1966 in the proceedings of the IEEE [11]. With this work, David W. Allan placed the basis on which the statistics of optical clocks is built. At this time, the role of atomic frequency standards was gaining more and more importance. Due to the unprecedented precision that these devices provide, quantum and electronic noise sources become critical. This section will give an overview about statistical definitions and limitations relevant for atomic clocks.

Let's create a mental experiment consisting of 100 uncorrelated two-level atoms of the same species. The atoms are excited with the same light source. The emission from atoms is then detected with an ideal high-precision detector. The frequencies detected would vary from an atom to another. Nevertheless, most of the atoms would emit at or near the central frequency  $f_0$  which can be obtained by calculating the mean:

$$f_0 = \frac{\sum_{n=1}^{100} f_n}{n} \quad (2.7)$$

where  $f_n$  represents the frequency of the  $n^{\text{th}}$  atom. After finding the mean value, it is interesting to study the spectral distribution of our measurement. This information can be extracted from the sample standard deviation  $\sigma$ :

$$\sigma = \sqrt{\frac{\sum_{n=1}^{100} (f_n - f_0)^2}{n - 1}} \quad (2.8)$$

Through this expression, the frequency distribution around the central value can be plotted and the uncertainty can be determined. Let us take the case of moving atoms as an example. The Doppler effect here would play a non-negligible role, thus broadening the frequency range around which the individual atoms can emit. The result is a large standard deviation. Till now I have been dealing with the emission process as discrete. For a clock measurement we have to sample our data over a period of time. Even if uncorrelated repetition events are assumed, the error that appears at time  $t$  would be preserved throughout the whole measurement. If the errors are added up throughout the whole integration time, the average frequency yields [11]

$$\langle f(t) \rangle = \lim_{T \rightarrow \infty} \frac{1}{T} \int_{-T/2}^{T/2} f(t) dt \quad (2.9)$$

Such a behaviour is fatal for the classical standard deviation which would then diverge with time. The change in frequency over a time interval  $\tau$  is reserved in the phase angle  $\phi(t + \tau)$  of the electromagnetic (EM) wave. The frequency of the EM wave under observation at time  $t$  is directly proportional to the derivative of  $\phi$  with time. Therefore, the frequency  $f$  is written as

$$f = f_0 + \frac{1}{2\pi} \frac{d\phi}{dt} \quad (2.10)$$

White Phase Modulation	$\alpha = 2$	SD diverges
Flicker Phase Modulation	$\alpha = 1$	SD diverges
White Frequency Modulation	$\alpha = 0$	SD converges
Flicker Frequency Modulation	$\alpha = -1$	SD diverges
Random Walk Frequency Modulation	$\alpha = -2$	SD diverges

**TABLE 2.3:** The five most relevant Power-Law noises, their corresponding value of  $\alpha$ , and whether the standard deviation (SD) converges for each of them [11].

Without going into the mathematical details, the variance extracted from eq. 2.9 is derived to be [11]

$$\sigma^2 = \frac{2}{\tau^2} \left( \underbrace{\langle \phi^2(t) \rangle}_{R_\phi(0)} - \underbrace{\langle \phi(t+\tau) \cdot \phi(t) \rangle}_{R_\phi(\tau)} \right) \quad (2.11)$$

where  $R_\phi(\tau)$  is known as the autocovariance function and is nothing but the time average of  $\phi(t+\tau) \cdot \phi(t)$ . The importance of this expression lies in the equality of  $R_\phi(\tau)$  to the fourier transform of the power spectral density of the phase  $S_\phi(\omega)$ , as the Wiener-Khinchin theory states [11], thus the final result

$$S_\phi(\omega) = h\omega^\alpha \quad (2.12)$$

where  $\alpha$  is an integer and  $\omega$  is the fourier frequency. Although power spectral densities at  $\alpha = -3$  and  $\alpha = -4$  appear from time to time, the range  $-2 < \alpha < 2$  is often enough to model the instability of almost every frequency source [54]. The five most relevant noise types and the corresponding values for  $\alpha$  are shown in table 2.3. As also shown, the classical standard deviation diverges for the majority of noise types. To avoid this statistical inconvenience, the so-called Allan variance is used to handle data related to time and frequency measurements. When dealing with the classical variance, the data point taken at time  $\tau$  is subtracted from the mean. The Allan variance however takes the difference between different data points thus eliminating the walk away movement from the central value, and it is expressed as [55]

$$\sigma_y^2(\tau) = \frac{1}{2(m-2n)n^2\tau_0^2} \sum_{i=1}^{m-2n} (\phi_i - 2\phi_{i+n} + \phi_{i+2n})^2 \quad (2.13)$$

where

- $\phi_i$  is the phase of the  $i^{\text{th}}$  measurement,

Allan Variance	$\frac{1}{2(m-2n)n^2\tau_0^2} \sum_{i=1}^{m-2n} (x_i - 2x_{i+n} + x_{i+2n})^2$
Mod. Allan Variance	$\frac{1}{2(m-3n+1)n^2\tau_0^2} \sum_{j=1}^{m-3n+1} \left[ \sum_{i=j}^{n+j-1} (x_i - 2x_{i+n} + x_{i+2n}) \right]^2$
Hadamard Variance	$\frac{1}{6(m-3n)n^2\tau_0^2} \sum_{i=1}^{m-3n} (x_i - 3x_{i+n} + 3x_{i+2n} - x_{i+3n})^2$
Time Variance	$\frac{\tau^2}{3} (\text{Mod.}\sigma_y^2(\tau))$
Allan Deviation	$\sigma_y(\tau)$

**TABLE 2.4:** The most commonly used statistical expressions in the field of time and frequency measurements [55].

- $\tau_0$  is the measurement period,
- $m$  is the total number of data points,
- and  $n\tau_0$  is the total averaging time.

Several expressions related to the Allan variance (AVAR) are used to express the stability of atomic clocks (see table 2.4). The square root of the Allan variance is called the Allan deviation (ADEV). The ADEV is the most popular statistical expression for time and frequency measurements. Although it is resistant to time and frequency offsets, the ADEV fails in the presence of linear frequency drifts. Other disadvantages are its inability to distinguish between white frequency modulation (WFM) and flicker phase modulation (FPM), and an increasing uncertainty for longer averaging times. In the presence of high WFM and FPM noise levels, it is advantageous to use the modified Allan variance  $\text{Mod}\sigma_y^2(\tau)$  which is able to distinguish between both noise types on one hand, and to average them out on the other hand. But still the  $\text{Mod}(\text{ADEV})$  cannot handle linear frequency drifts. To tackle this phenomenon, a third difference statistics expression was developed namely the Hadamard variance or deviation (HDEV). The HDEV produces higher uncertainties at large averaging times compared to the ADEV. Its insensitivity, however, to linear frequency drifts makes it a very useful statistical tool. Another widely used expression is that of the time deviation. Its main application is studying time offsets on a short term basis. More about these techniques can be found in reference [55].

## 2.5 Systematic Errors in Optical Lattice Clocks

Limitations on the precision of optical clocks are different in magnitude and can have many causes. While some are due to intrinsic characteristics such as the natural linewidth of the atomic transition, others are dependent on experimental systematics. The systematic errors relevant for clocks based on neutral atoms are partly different

from those based on ions. The DC Stark shift and the quadrupole shift are two good examples of error sources which play a bigger role in ion optical clocks than for optical clocks based on neutral atoms, with some exceptions such as having a dielectric surface close to the atomic sample. The DC Stark shift which is proportional to  $\langle E^2 \rangle$  becomes relevant when the ion undergoes a certain displacement from the center of the trap. In this case, the non-vanishing electric field induces micromotion which has to be compensated upon in order to reduce the shift. The quadrupole shift on the other hand is to be considered when dealing with atomic states which have an electric quadrupole moment, as the name suggests. The interaction of the atom with the DC quadrupole component of an external electric field leads to a quadrupole shift. I will not go into details about the shifts in ion clocks, but interesting readers can refer to [36]. Since my topic has to do with optical clocks based on neutral atoms, I will give a short description of the most important shifts which have to be limited in order to reach a higher stability.

### The Zeeman shift

When an atom happens to be at a position where a magnetic field is present, we speak about a Zeeman shift. Whether to worry about such an effect or not is dependent on the atomic transition we are dealing with. Generally, each of the atomic states couple differently to the magnetic field through their magnetic moments, which in turn correlate with the total angular momentum of each state. The resulting frequency shift on the clock transition can then be expressed as [56]

$$\delta\nu = \alpha_{e,g}B + \beta_{e,g}B^2 \quad (2.14)$$

where  $\alpha_{e,g}$  and  $\beta_{e,g}$  are the Zeeman shift coefficients. The first and the second items in the equation represent the first-order and the second-order Zeeman shifts, respectively. While it is possible to eliminate the first-order Zeeman effect by choosing the right atomic transition, the second-order Zeeman shift will stay there due to interactions between the neighboring atomic states [56]. The spectroscopy measurements that were done in the scope of this thesis on the clock transition  $^1S_0$ - $^3P_0$  in  $^{171}\text{Yb}$  show a clear presence of the first-order Zeeman shift. This is due mainly to the presence of the nuclear spin and the state mixing between the  $^3P_0$  and the  $^3P_1$  states. The linear Zeeman shift that the  $^1S_0$ - $^3P_0$  clock transition in  $^{171}\text{Yb}$  experience is  $-4.1 \text{ m}_F \text{ Hz}/\mu\text{T}$  [39], while the second-order Zeeman shift measured for  $^{174}\text{Yb}$  is  $-6.12 \text{ Hz}/\text{mT}^2$  [42].

### The collisional shift

Another source of shift is the collisional shift. Its origin are the atom-atom and the atom-background gas collisions. Atom-atom interactions can result in frequency shifts when the atom density is high. Thus, this kind of shift is mainly relevant for optical clocks based on neutral atoms. Neutral atoms trapped in a 1-D optical lattice experience cold collisional shifts as a result of the van-der-Waals interaction. The collisional shift is directly dependent on the density of atoms in a lattice site

and on the states which the atoms occupy. Taking  $^{171}\text{Yb}$  into consideration, it has been shown that the collisional frequency shift is a result of the dominant p-wave interactions for atoms in the  $^1\text{S}_0$  and  $^3\text{P}_0$  states [57]. If working with a 1-D optical lattice, one should take good care concerning the homogeneity of the clock laser's optical beam, as well as its alignment. The group at NIST has measured a collisional shift of  $-16 \times 10^{-16}$  for  $^{171}\text{Yb}$  with a density of  $10^{11}/\text{cm}^3$  in 2009 with an uncertainty of  $0.8 \times 10^{-16}$  [15].

### The AC Stark shift

The Stark shift is a frequency shift which occurs due to the interaction of the atomic transition, in this case for example the clock transition, with electromagnetic radiation. For optical clocks operating with neutral atoms, the most known Stark shifts are the AC Stark shift and the blackbody shift.

The probing light field is one of the sources that can result in an AC Stark shift. This shift exists because of the non-resonant coupling of the  $^3\text{P}_0$  state with the  $^3\text{P}_1$  state. Theoretically, this should not be a problem when probing bosonic isotopes. However, the magnetically induced spectroscopic method which makes it possible to probe the clock transition for even isotopes induces again a coupling between the given states. Thus, a Stark shift arises.

Another trigger for the AC Stark shift is the trapping light field. Its interaction with the atomic states is expressed as

$$\Delta\hbar\omega_0 = -\frac{1}{4}\Delta\alpha(\vec{e} \cdot \omega_{laser})E^2 - \frac{1}{64}\Delta\gamma(\vec{e} \cdot \omega_{laser})E^4 - \dots \quad (2.15)$$

The first term proportional to  $E^2$  disappears when operating the optical lattice at the magic wavelength. Its dependence on the polarization, however, makes it hard to get rid of it completely because of polarization impurities. This is because of the trapping light field's transmission through windows or reflections from mirrors. Therefore, the first term in this equation expresses the lattice polarizability shift.

The second term, known as the hyperpolarizability and expressed as  $\Delta\gamma(\vec{e} \cdot \omega_{laser})$ , is a 2-photon process with a quadratic dependence on the light intensity. The shift arising from this phenomena is a result of a two photon resonance process. For ytterbium, the closest two photon resonance to the magic wavelength is the  $6s6p^3P_0 \rightarrow 6s8p^3P_0$  at 759.7082 nm [58]. This shift can be reduced by operating the trapping light field at lower intensities.

### The blackbody shift

Not only light fields produce a Stark shift, but also thermal fields. Since the trapped atoms are present in a vacuum chamber at room temperature, the emitted blackbody radiation has also its contribution to the total Stark shift. The thermal waves interact with the different states of the transition and induce in turn a shift which is very

similar to the AC Stark shift. The blackbody shift increases with the temperature in the surrounding environment. This effect is described by the Stefan-Boltzmann law which states

$$I_{thermal} = (5.67 \times 10^{-8} \text{Wm}^{-2}\text{K}^{-4})T^4 \quad (2.16)$$

with  $I_{thermal}$  being the intensity of the radiation emitted by the body which is surrounding the atomic sample and  $T$  is the body's temperature. The proportionality of the intensity to  $T^4$  explains the sensitivity of the induced shift with regard to the temperature. Moreover, the blackbody emission spectrum changes with temperature. The effect of the blackbody radiation on the performance of optical clocks using the  $^1S_0 - ^3P_0$  clock transition was studied by Porsev and Derevianko in 2006. Special care is taken when dealing with the upper state. That's because the wavenumber of the blackbody radiation at 300 K is  $208.51 \text{ cm}^{-1}$ . This enhances transitions between the three manifolds ( $j=1,2,3$ ) belonging to the  $^3P$  state. Therefore, the authors went beyond the electric-dipole approximation and took advantage of the multipolar contributions to calculate the blackbody radiation shift  $\delta E_g$  to be [59]

$$\delta E_g = \sum_{J\lambda} \delta E_g^{J\lambda} \quad (2.17)$$

which is nothing but the sum over the multipolar contributions  $\delta E_g^{J\lambda}$  (a detailed derivation can be found in [59]). Here the solution for  $\delta E_g^{J\lambda}$  in the ground state  $^1S_0$  is different than that of the excited state  $^3P_0$ . This is due to the large transition energy between the ground state and the second closest state compared to the temperature  $T$ . Through subtracting the blackbody radiation shift of the ground state from the upper state, the total shift on the clock transition for yb was calculated to be  $-1.34 \text{ Hz}$  [59]. This value for the blackbody radiation shift was reproduced experimentally in NIST by Oates et. al. [60]. The experimental value of the BBR shift was measured to be  $-1.27 \text{ HZ}$  at  $T=300\text{K}$ . This value was obtained after a precise measurement of the differential static polarizability of the  $^1S_0$  and the  $^3P_0$  clock states, which yielded  $36.26 \text{ kHz}(\text{kV}/\text{cm})^{-2}$  [60]. The major source of uncertainty with respect to the BBR shift was the  $1\text{K}$  uncertainty in temperature. At room temperature, this added to the uncertainty of the clock transition by  $3 \times 10^{-17}$  [60]. As equation 2.16 suggests, a method to reduce the effect of blackbody radiation would be to place the trapped atoms in a cryogenic environment.

### The gravitational shift

The last shift that I would like to point to is the gravitational shift, which is a result of the gravitational redshift. Let us consider for example a light source mounted at the Düsseldorfer tower where the gravitational potential energy at that point is  $V_a$ . The light field which leaves the source at  $V_a$  and travels towards the earth, where the potential energy is  $V_b$ , experiences a frequency shift. For  $V_a > V_b$ , the observer at position  $b$  measures a higher frequency, and vice versa. The redshift is then [56]

$$\frac{\Delta\nu}{\nu} = \frac{1}{c^2} \int_a^b g \cdot dx \quad (2.18)$$

Effect	Shift $^{171}\text{Yb}$	Shift $^{174}\text{Yb}$
Blackbody radiation shift	$-25 \times 10^{-16}$	$-25 \times 10^{-16}$
Second-order Zeeman shift	$-1.67 \times 10^{-16}$	$-1.8 \times 10^{-14}$ to $-3.6 \times 10^{-14}$
Collisional shift	$-16.1 \times 10^{-16}$	$-2 \times 10^{-16}$
Probe light Stark shift	$0.05 \times 10^{-16}$	$6 \times 10^{-15}$ to $12 \times 10^{-15}$
Lattice polarizability	$0.4 \times 10^{-16}$	$< 1 \times 10^{-15}$
Hyperpolarizability	$3.3 \times 10^{-16}$	$3.3 \times 10^{-16}$

**TABLE 2.5:** Values of frequency shifts in fractional units for bosonic and fermionic ytterbium, adopted from [15] and [42], respectively.

When doing a frequency measurement on an optical clock, we compare two different oscillators. Each of the oscillators serve as an observer in relationship to the other. At positions with different potential energies, the observer will measure a shifted frequency. Thus, in order to compensate for the gravitational shift, two parameters have to be taken into consideration. The first is the vertical distance between the two oscillators, denoted in the above equation as  $x$ . The second one is the gravitational acceleration at the positions where both clocks are located. While it is quite straight forward to measure  $\Delta x$ , it is hard to compensate for the part resulting from the gravitational acceleration due to its dependence on the earth's structure at that particular location. That's one of the main motivations to develop transportable optical clocks. Such clocks open the way for comparing clocks near each other, thus raising the measurement's precision.



# Chapter 3

## Theory of Laser Cooling and Trapping

Does radiation carry momentum? The whole story of trapping atoms with laser light began with this question. Early theoreticians, such as Maxwell and Einstein, showed the existence and importance of this phenomena. But since it is hard to observe these effects using thermal light, an experimental study of this topic was not possible before the invention of the laser in 1957. T.W.Haensch and A.L.Schawlow were the first to propose cooling an atomic beam using laser light [21].

The theory presented in this chapter exists since many years, and is the building block for laser cooling and trapping experiments. A big part of this section has been adopted from my master thesis, in which the theory of laser cooling and trapping has been explained thoroughly [2]. The topics discussed in this chapter are the ones relevant for our experimental work. A detailed theoretical review can be found in different specialized textbooks on the topic [61].

### 3.1 The Radiation Force

To form a complete picture of the topic, light-matter interaction should be described quantum mechanically. For our purposes, the semi-classical description will also do the job. In this semi-classical treatment, a 2-level atom will be considered that is interacting with a laser light having a wavevector  $\vec{k}$ .

An atomic beam illuminated by laser light experiences a force [61]:

$$\vec{F} = \hbar \vec{k} \frac{\Gamma_{10}}{2} \frac{\Omega_0^2(\vec{r})/2}{\delta^2 + (\Gamma_{10}/2)^2 + \Omega_0^2(\vec{r})/2} - \frac{\hbar \delta}{4} \frac{\vec{\nabla} \Omega_0^2(\vec{r})}{\delta^2 + (\Gamma_{10}/2)^2 + \Omega_0^2(\vec{r})/2} \quad (3.1)$$

This equation is considered by many textbooks to be the starting point when discussing the topic of light matter interaction. Therefore, it is useful to discuss it in details. The parameters  $\Gamma_{10}$  and  $\Omega_0$  that are introduced in eq. 3.1 are the decay rate from state 1 to state 0 and the Rabi frequency, respectively. The decay rate can be

expressed as [61]

$$\Gamma_{10} = \frac{\omega_{10}^3 d_{10}^2}{3\pi\epsilon_0 \hbar c^3} \quad (3.2)$$

whereas the Rabi frequency is [61]

$$\Omega_0 = \frac{\vec{d}_{10} \cdot E_0 \vec{\epsilon}}{\hbar} \quad (3.3)$$

where  $\omega_{10}$  is the resonance frequency to excite the atom from state 0 to state 1,  $d_{10}$  is the dipole matrix element, and  $E$  is the field's electric field oscillating in the  $\vec{\epsilon}$  direction. In addition to the force's dependence on decay rate and the Rabi frequency, the detuning of the laser  $\delta$  also appears in eq. 3.1 and plays a major role in the topic of laser cooling and trapping of atoms.

Assuming a detuning  $\delta \gg \Gamma_{10}$ , the equation describing the force simplifies to [61]

$$\vec{F} = \hbar \vec{k} \frac{\Gamma_{10}}{4} \frac{\Omega_0^2(\vec{r})}{\delta^2} - \frac{\hbar}{4} \frac{\vec{\nabla} \Omega_0^2(\vec{r})}{\delta} \quad (3.4)$$

The first part of the above equation is referred to as the dissipative force and the second part as the reactive force. The dissipative force is responsible for cooling, whereas the reactive force represents the trapping effect of the radiation force. In contrast to the reactive force, which is dependent on the sign of the detuning, the dissipative force depends only on the magnitude of the detuning. By going to higher light intensities we are able to increase the deceleration of atoms till we reach saturation at

$$\vec{a}_{max} = \frac{\hbar \vec{k} \Gamma_{10}}{2M} \quad (3.5)$$

where  $M$  is the atomic mass. For a completely saturated transition, half of the population would be in the excited state. That is where the factor of 2 in eq. 3.5 comes from. This limit for the maximum deceleration is induced by stimulated emission which becomes relevant when a certain intensity is reached.

## 3.2 Cooling Atoms Using Laser Light

This section and the next one will explain in more details the role of the dissipative and the reactive forces in cooling and trapping atoms. Starting with the dissipative force  $F_{diss.}$ , this force is active in the cooling and slowing processes. Before going into more details, it is essential to mention the relationship between the atomic temperature and velocity that will keep on appearing in this context. There is a direct connection between these two quantities that is described as

$$k_B T = m(v_{rms,x})^2 \quad (3.6)$$

Thus, the r.m.s thermal velocity ( $v_{rms,x}$ ) of an atomic beam traveling in the x direction is proportional to the square-root of the atomic temperature T. This leads to the conclusion that cooling an atomic beam can be done by taking out momentum. Therefore, if resonance between the atomic beam and the counter-propagating light field can be assured for different velocities, a continuous slowing process over a defined length can be achieved. This brings us to the topic of Zeeman slowing.

### 3.2.1 Zeeman-Slowing

As it was shown in the previous section, atoms can be decelerated and cooled by laser light. However, in order for this process to be successful, the right conditions have to be met. One of the most important conditions is illuminating the moving atoms with the right frequency. This said, the continuously changing frequency of the atomic transition along the slowing-axis has to be compensated for in order to assure resonance between the atomic transition and the laser light. But before discussing the Zeeman-slowing technique for doing that, let us speak a bit about the frequency shift associated with the moving atoms, namely the Doppler shift.

#### The Doppler shift

We consider again an atom at rest with a ground state 0 and an excited state 1. Both states are separated by the energy  $\hbar\omega_{10}$ . By absorbing a photon with wavevector  $\vec{k}$ , the atom is excited to state 1 before decaying back to state 0 through spontaneous emission. The average result is then a change in momentum  $\Delta p = -\hbar k$ . In the case of a moving atom, the atomic transition and the laser field are shifted out of resonance due to the Doppler effect. For a moving atom to stay at resonance with the laser frequency, a velocity-correlated correction of the resonant frequency has to be applied. This can be done either by manipulating the atomic transition or by changing the laser frequency. For a laser field to be resonant with a moving atom, its resonant frequency with the atoms at rest  $\nu_L$  has to be adjusted in order to compensate for the Doppler shift, such that

$$\nu'_L = \nu_L - \vec{k} \cdot \vec{v} \quad (3.7)$$

where  $\nu'_L$  is the adjusted frequency of the laser,  $\vec{k}$  is the wavevector of the laser and  $\vec{v}$  is the velocity vector of the atoms. To successfully cool an atomic beam, the laser frequency  $\nu'_L$  has to be regularly modified to stay at resonance with the decelerating atoms. A better and relatively simple solution to compensate for the Doppler shift is to go the other way around and adjust the frequency of the atomic transition to stay at resonance with the laser beam. The device used for this purpose is the so-called Zeeman slower.

D. Phillips and H. Metcalf were the first to demonstrate the method of keeping the cooled atoms and the cooling laser at resonance by Zeeman splitting the atomic excited state with an external magnetic field [62]. The applied magnetic field along

the slowing region results in a Zeeman shifted energy of [61]

$$\Delta E = \pm g\mu_B m_J B_z \quad (3.8)$$

where  $g$  is the Landé  $g$ -factor,  $\mu_B$  is the Bohr magneton and  $B_z$  is the magnetic field along the  $z$  axis. Therefore, the energy separation of the Zeeman substates  $m_J = \pm 1$  can be manipulated by the external magnetic field  $B_z$ . Additionally, we can choose whether to excite the  $J=0 \rightarrow J=1(m_J = +1)$  transition or the  $J=0 \rightarrow J=1(m_J = -1)$  by using  $\sigma^+$  or  $\sigma^-$  polarization, respectively. In our setup, the  $\sigma^-$  scheme is adopted (see fig. 3.1) [2].

For the  $\sigma^-$  cooling scheme, the laser frequency is resonant with the fast atoms at velocity  $v_i$ , just after leaving the atomic oven. As atoms move away from the oven their speed is slowed down by the laser beam. The changing Doppler shift is compensated for by the external magnetic field

$$B(z) = \frac{\hbar k v_i}{\mu} \left( 1 - \sqrt{1 - \frac{z}{z_o}} \right) \quad (3.9)$$

Thus, the Zeeman slower's magnetic coil should produce a magnetic field close to zero at the location closest to the atomic oven ( $z=0$ ) and  $\hbar k v_i / \mu$  at  $z=z_o$ . In order to determine  $z_o$ , namely the length of the slower, we have to combine the Zeeman slower's deceleration capability with the final atom velocity sought. To minimize the size of the Zeeman slower, one has to go for the maximum deceleration [61]

$$a = \frac{\hbar k \gamma_{10}}{2m} \quad (3.10)$$

This is achieved when the laser is operated at resonance with the atomic transition and at an intensity that is high enough but not too high, to avoid stimulated emission [61]. In a laboratory environment, even if these conditions are met, the deceleration will always be smaller by a factor  $\eta$  due to technical imperfections. According to Newton's laws of motion and eq. 3.10, slowing an atom from an initial velocity  $v_i$  to a final velocity  $v_f$  requires a slowing distance of [2]

$$z_0 = m \frac{v_i^2 - v_f^2}{\eta \hbar k \gamma_{10}} \quad (3.11)$$

where  $\gamma_{10}$  is the natural linewidth of the atomic transition. Therefore, when considering maximum deceleration for a Zeeman slower, its length would be determined by the atomic species we want to cool, the initial and final velocities of the atoms, and the design parameter  $\eta$ .

### 3.3 Magneto-Optical-Trapping

It was shown in the previous section how to slow atoms coming out of an atomic oven by laser radiation. The second step would be to trap them and cool them in order

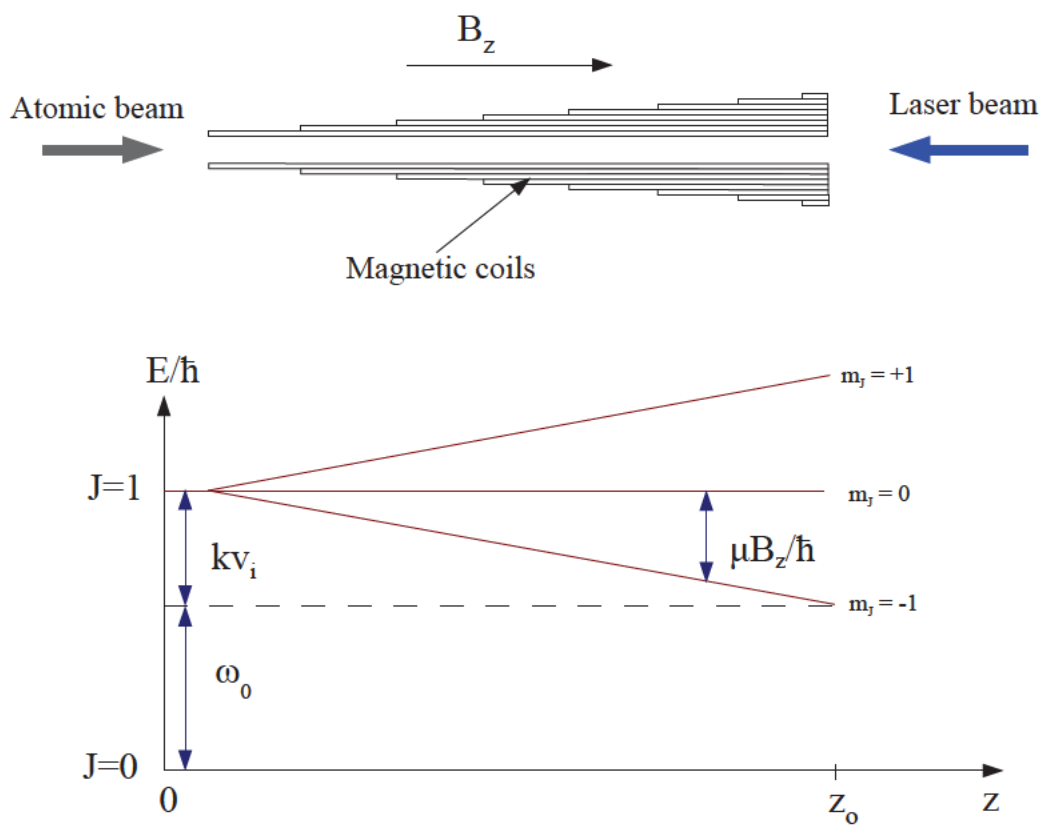


**FIGURE 3.1:** A schematic showing the function of  $\sigma^-$  cooling. The laser is at resonance with atoms moving at  $v_i$ . The increasing magnetic field with  $z$  accounts for the decreasing doppler shift experienced by the slowed atoms [2].

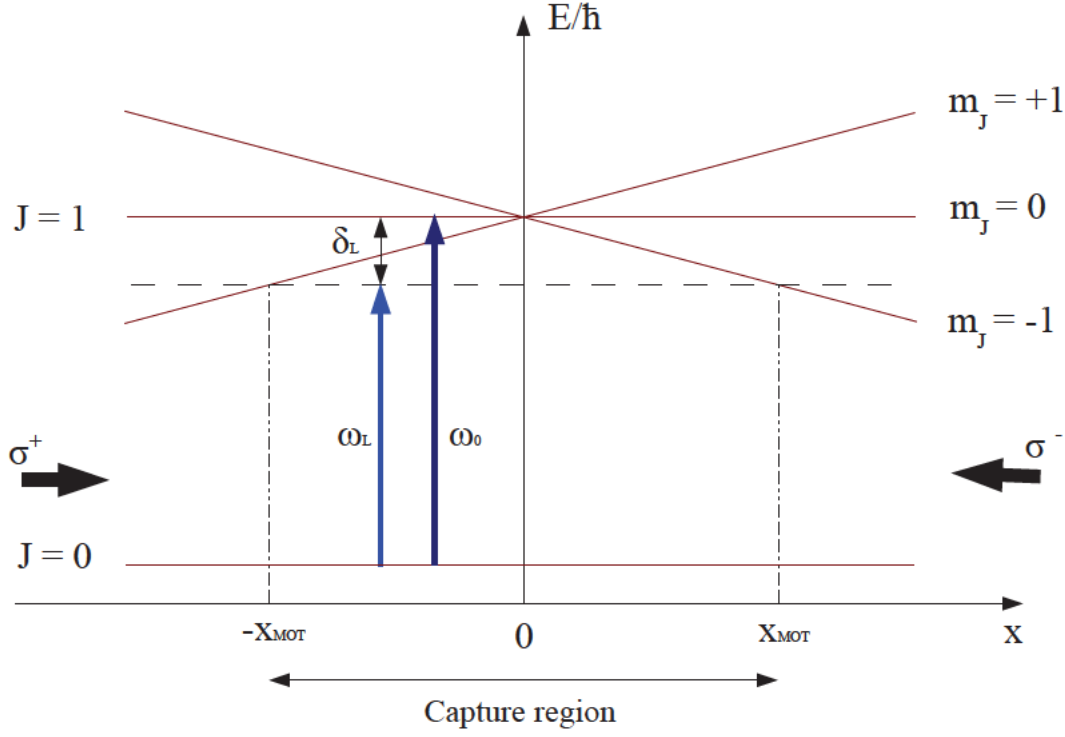


**FIGURE 3.2:** A schematic of a one-dimensional MOT. Atoms near the region  $z=0$  are illuminated with  $\sigma^-$  ( $\sigma^+$ ) polarized light from the right(left). The magnetic field increases(decreases) linearly with distance from  $z=0$  [2].

to gain longer access to the cold atoms. In this section, the Magneto-Optical-Trap (MOT) will be introduced, which became one of the essentials in almost every experiment dealing with ultra-cold neutral atoms. MOT setups make use of inhomogeneous magnetic fields and circularly polarized laser beams to trap the atoms within the MOT's capture region through spatially dependent absorption of photons. For the sake of simplicity, this section will explain the physics behind one-dimensional MOTs for atoms with a  $J=0 \rightarrow J=1$  transition.

A model of a 1-D MOT acting on an atomic transition  $J=0 \rightarrow J=\pm 1$  is shown in figure 3.2. The inhomogeneous magnetic field  $B(x)$  has a given gradient and vanishes at  $x=0$ . For an atom located at position  $x$ , the magnetic field  $B(x)$  shifts the energy of an atomic transition with ground state 0 and excited state 1 by

$$\Delta E(x) = (g_1(m_j)_1 - g_0(m_j)_0)\mu_B B(x) \quad (3.12)$$

where 0 and 1 refer to the ground and excited state,  $g_{10}$  is the Landé  $g$  factor,  $m_{10}$  is the magnetic quantum number,  $B(x)$  is the spatially dependent magnetic field, and

$\mu_B$  is the Bohr magneton. This leads us to the spacially dependent absorption of photons by slowly moving atoms. The calibration of the laser beams' polarizability with the magnetic field gradient should be done such that atoms at positions  $\pm x$  get pushed towards the center.

Through referring to figure 3.2, the scenarios for atoms at different positions can be split as follows:

- For  $x=0$  : The atoms experience no Zeeman shift due to the infinitesimal magnetic field. Therefore, the probability that the atoms absorb a photon from either beam is equal. This results in a net force equals to zero.
- For  $x>0$  : The Zeeman shift brings the transition  $J=0$  (  $(m_j)_0=0$  )  $\rightarrow$   $J=1$  (  $(m_j)_1=-1$  ) close to resonance with the laser beams. Therefore, the atoms at that position will couple to the  $\sigma^-$  polarized laser beam coming from the right and get pushed towards the center.
- For  $x<0$  : The same principle as described in the previous case happens here but in the opposite direction. The negative magnetic field brings the transition  $J=0$  (  $(m_j)_0=0$  )  $\rightarrow$   $J=1$  (  $(m_j)_1=+1$  ) closer to resonance with the laser frequency. The result is atoms absorbing light from the  $\sigma^+$  polarized laser beam directed from the left towards the center. Therefore, atoms gain momentum towards the center of the trap.

The trapping process described above works only if the laser is red-detuned with respect to the atomic transition. This limits the trapping region of the MOT to within  $\pm x_{MOT}$ . Beyond this limit, the laser frequency becomes blue detuned with the atomic transition leading to the loss of atoms. This behaviour is that of a damped harmonic oscillator and can be written as [61]

$$F_{diss.} = \alpha v + \kappa x \quad (3.13)$$

where  $\alpha$  is the damping coefficient and  $\kappa$  is the spring constant. For red detunings, the spring constant is negative and thus the force is restoring which results in an oscillatory motion of atoms around  $x=0$ . A blue detuning on the other hand leads to a non-restoring force. This results in atoms being expelled out of the trap.

As atoms get confined to a small region around the center of the trap and their velocity becomes very small, their movement to either direction becomes less distinguishable for the laser radiation. This raises the probability of atoms that are moving in one direction to absorb photons coming from both directions. This behavior sets a limit to which atoms can be cooled in a MOT, known as the Doppler limit [63]

$$T_D = \frac{\hbar\gamma_{10}}{2k_B} \quad (3.14)$$

where  $h$  is the planck's constant,  $k_B$  is the Boltzmann's constant and  $\gamma_{10}$  is the natural linewidth of the atomic transition. Schemes to cool atoms beyond the Doppler limit have already been demonstrated. Interested readers can refer to [61].

### The capture process

Till now we have been assuming that atoms in the trapping region have low velocities. In laboratory environments, atoms usually leave the Zeeman slower and enter the MOT with velocities on the order of tens of m/s. To assure that the atoms are captured by the MOT, their velocity shouldn't exceed the capture velocity

$$v_c = \sqrt{ar_c} \quad (3.15)$$

If the maximum deceleration  $a$  of the atoms exerted by the MOT is not enough to stop them within the effective MOT diameter  $2 \times r_c$ , the atoms will escape the trap. The deceleration of atoms inside the MOT is directly related to the laser's intensity and detuning. Through choosing the right detuning, one can increase  $v_c$  by a factor of two [61].

The derivation that led to eq. 3.13 assumed that the atoms are moving at low velocities. Even though this argument fails here, the equation is still valid, but the non-vanishing Doppler shift has to be taken into consideration. Figure 3.3 shows a sketch that demonstrates the influence of the Doppler shift on the MOT's capture-radius. Atoms entering the trap with non-negligible velocities have a larger capture-radius than their much slower counterparts.

## 3.4 The Optical Lattice

A trap in which atoms are trapped in wavelength size regions of a standing wave is known as an optical lattice. An optical lattice confines atoms in the interference structure of a standing wave by means of the dipole force. This phenomena was suggested by Letokhov in 1968 [64], but first realised by C. Salomon et. al. in 1987 [65]. Analogous to the positioning of atoms in a real crystal, atoms in an optical lattice are also arranged in a periodic structure. The acting force in this case is the external potential of the electromagnetic field.

An optical lattice plays a big role in suppressing the Doppler broadening of atomic transitions in optical lattice clocks. Even after cooling the atoms in a MOT to a few mK temperatures, the atomic motion can result in a Doppler broadening on the order of tens of kHz [66]. It has been shown however, that through trapping the atoms within a spacial region smaller than the probing laser's wavelength, the Doppler broadening can be eliminated [67] [13]. This mechanism is known as the Lamb-Dicke confinement and can be quantified through the Lamb-Dicke parameter [68]

$$\eta = \frac{2\pi x}{\lambda_l} \quad (3.16)$$

where  $x$  is the width along which the atomic population is distributed in a lattice site and  $\lambda_l$  is the wavelength of the probing laser. For  $x \ll \lambda_l$ ,  $\eta$  is much smaller than one and thus trapped atoms are said to be in the Lamb-Dicke regime [67].

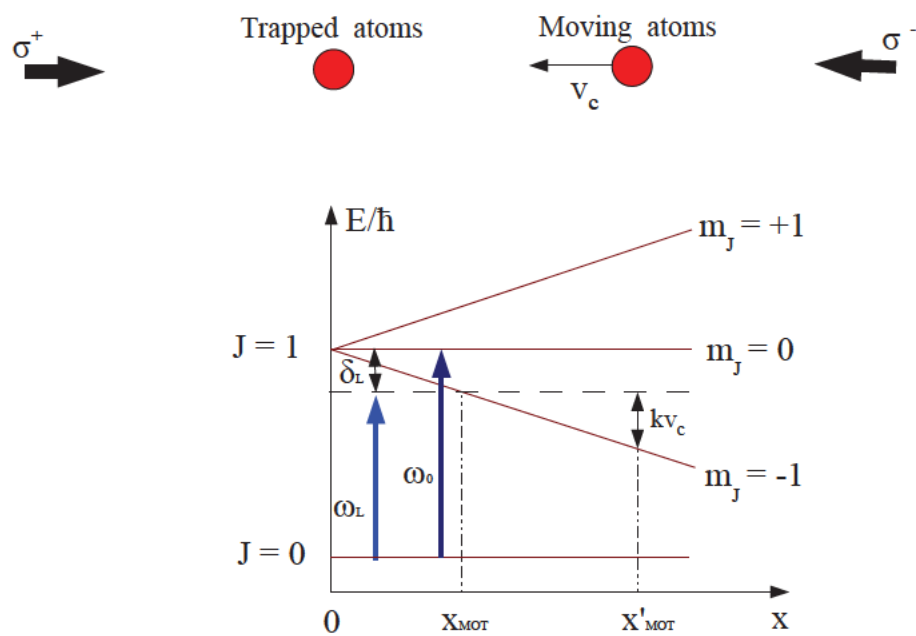


**FIGURE 3.3:** The capture distance of a MOT, where  $x_{MOT}$  and  $x'_{MOT}$  represent the trapping regions for atoms moving initially at very low velocities and others moving with  $\vec{v}_c$ , respectively [2].

### The physical mechanism

In the presence of a light field, atoms experience a light shift which acts on the ground and excited states of a given transition resulting in an energy shift [61]

$$E_{10} = \frac{\hbar}{2}(-\delta \pm \sqrt{\Omega_0^2 + \delta^2}) \quad (3.17)$$

with  $\delta$  being the laser detuning from the atomic transition, and  $\Omega_0$  is the Rabi frequency. The light shift is a result of the atom-light interaction. Its dependence on the intensity of the light field  $I$  is embedded in  $\Omega_0$  which is proportional to  $\sqrt{I}$ . A light shift which is not constant with position results in an energy gradient. This creates the dipole force which is responsible for confining the atoms in an optical lattice.

Let's go back to the fact that our atoms are present at a position  $\mathbf{r}$  in a standing wave. The light intensity at this position is determined by the relative phase of the two counterpropagating beams, thus determining the strength of the force applied on the atoms. A simple visualisation of the trapping force is the net effect of the atom absorbing a photon from the first beam and emitting in the direction of the counterpropagating beam through stimulated emission, which gives the force a conservative nature. In contrast to the dissipative force, the dipole force can be arbitrarily large for large intensities. Since the momentum exchange between the atom and the light field occurs in both directions, the force averages to zero.

Now let us examine this effect for a single traveling light beam from a mathematical point of view. I will show here the semi-classical approach which is enough for our experimental purposes, following the review by Grimm et al. [69]. A quantum mechanical derivation can be found in specialized texts dealing with this topic [70].

The interaction of an electromagnetic field with an atom embedded in a light field can be quantified in terms of the dipole potential as follows

$$V_{dip} = -\frac{1}{2} \langle \vec{p} \cdot \vec{E} \rangle \quad (3.18)$$

with  $\vec{p}$  being the induced dipole moment

$$\vec{p} = \alpha(\omega) \vec{E} \quad (3.19)$$

and the factor 1/2 reflecting the fact that the dipole moment is induced and not permanent [69]. This equation is a result of the linear relationship between the external electric field and the induced atomic dipole moment. It also shows that  $\vec{p}$  oscillates at the same frequency as that of the external field through its proportionality to the complex atomic polarizability  $\alpha(\omega)$  [69]

$$\alpha(\omega) = 6\pi\epsilon_0 c^3 \frac{\Gamma}{\omega^2} \cdot \frac{1}{\omega^2 - \omega_l^2 - i(\omega_l^3/\omega^2)\Gamma} \quad (3.20)$$

with  $\Gamma$  standing for the atomic transition rate whereas  $\omega$  and  $\omega_l$  being the resonant transition frequency and light frequency, respectively. After some algebra, the expression for  $V_{dip}$  can be re-written as

$$V_{dip} = 3\pi c^2 \underbrace{\sum_a \frac{1}{\omega_a^2} \cdot \frac{\Gamma_a}{\omega_l^2 - \omega_a^2}}_{f_{dip}} \cdot I(\vec{r}) \quad (3.21)$$

The first part of this equation includes the atomic properties and is summed up over the relevant transitions from a given ground state. This equation shows the direct relationship of the dipole potential  $V_{dip}$  in a light field with the intensity distribution  $I(\vec{r})$ .

As we have seen, it is possible to trap atoms in a non-uniform light field. However, the number of trapped atoms can be increased simply by making the dipole potential deeper and more defined. A standing wave allows us to create a periodically varying intensity on the longitudinal axis. This creates a periodic arrangement of microscopic traps with very tight confinement. I will skip the mathematical derivation and go directly to show the expression for the dipole potential in the case of a standing wave (for a detailed explanation you can refer to [69])

$$V_{dip} = 4f_{dip} \frac{2P}{\pi\omega(z)^2} e^{-\frac{2r^2}{\omega(z)^2}} \cos^2 k_l z \quad (3.22)$$

where  $r, z$  are the cylindrical coordinates,  $P$  is the power of the light acting on the atoms and  $\omega(z)$  is the light-beam radius at position  $z$ . What is also clear in this formula is the oscillatory term which gives our potential a periodic structure along  $z$ . This structure allows us to trap the atoms in half wavelength intervals.

Trapping single atoms in different lattice sites helps reducing the collisional shift in optical atomic clocks (see section 2.5). A blue or red detuning determines if the atoms are trapped in the minima or the maxima of the intensity sites.



# Chapter 4

## The Experimental Setup

The aim for this thesis is to build a compact atomic source for an ytterbium optical lattice clock. Therefore, the focus from the beginning on was to build the whole setup on a 2 m<sup>2</sup> optical table. To achieve this goal a compact vacuum system was built and except of one compact fiber laser, all lasers used for cooling and trapping are compact diode lasers. In this chapter, the experimental setup will be shown.

### 4.1 Atomic Ytterbium

In this section, I will discuss the internal properties of atomic Ytterbium, with a focus on the 398.9 nm  $(6s^2)^1S_0 - (6s6p)^1P_1$ , the 555.8 nm  $(6s^2)^1S_0 - (6s6p)^3P_1$  and the 578.4 nm  $(6s^2)^1S_0 - (6s6p)^3P_0$  transitions. These transitions are relevant for pre-cooling, post-cooling and doing clock measurements, respectively [58].

Atomic ytterbium is a rare earth element with seven stable isotopes, five of them are bosons and two are fermions. The relative natural abundances, atomic mass numbers, nuclear spins and magnetic moments are given in table 4.1.

The ytterbium ground state configuration is  $Xe + 4f^{14}6s^2$  [72]. So the two electrons in the 6s shell are the relevant ones for Yb optical clocks. Thus, the total spin  $S$  can take the values 0 or 1, resulting in singlet states for atoms in the ground state whereas triplet states appear when an electron is excited to the p-states.

$$S = 0 \rightarrow J = L \tag{4.1a}$$

$$S = 1 \rightarrow J = L - 1, L, L + 1 \tag{4.1b}$$

This structure is typical for alkaline earth-like atoms and is an essential factor in making Yb a good candidate for optical clocks.

To explain this further, let's go back to the selection rules for atomic transitions shown in table 4.2. According to these rules, transitions within the manifolds are allowed, such as the  $(6s^2)^1S_0 - (6s6p)^1P_1$  transition. However, transitions between the manifolds are forbidden because then the  $\Delta S = 0$  is violated [74]. Two of the

Isotope	Rel.Abundance[%]	Nuclear spin	Magnetic moment
168	0.13	0	-
170	3.05	0	-
171	14.3	1/2	+0.4919
172	21.9	0	-
173	16.12	5/2	-0.6776
174	31.8	0	-
176	12.7	0	-

**TABLE 4.1:** The relative abundances, nuclear spins, and magnetic moments of the stable isotopes of ytterbium [71].

Transition Type	$\Delta J$	$\Delta M_J$	$\Delta S$	$\Delta L$	$\Delta \Pi$
Electric Dipole	0, $\pm 1$	0, $\pm 1$	0	-	1
Electric Quadrupole	0, $\pm 1, \pm 2$	-	0	0, $\pm 1, \pm 2$	0
Magnetic Dipole	$\pm 1$	-	0	0	0

**TABLE 4.2:** Selection rules for electric dipole, electric quadrupole, and magnetic dipole transitions between L-S coupled states [73].

transitions required for Yb optical clocks violate the selection rules. Here are the most important characteristics of the mentioned transitions:

- The  $^1S_0$ - $^1P_1$  blue transition is the only fully allowed transition used. It is a fast transition with an excited-state lifetime of 5.68 ns [71]. Its large scattering rate makes it a good transition for the first cooling stage. But with its broad linewidth of 29 MHz [3] and the lack of a hyperfine structure, and thus of a Zeeman structure, in the ground state (especially in bosons) makes it impossible to cool atoms below the Doppler limit of  $T_D=700 \mu K$ . Since that's not low enough for the purposes of an optical clock, we have to use another transition to cool the atoms further.
- Although the  $^1S_0$ - $^3P_1$  green transition at 555.8 nm violates the rule  $\Delta S = 0$ , the mixing of the singlet  $^1P_1$  state with the  $^3P_1$  state makes it a key transition for cooling Yb. With a relatively narrow linewidth of  $2\pi \cdot (180 \text{ kHz})$  [4] corresponding to a lifetime of 874 ns, the transition rate is high enough to produce a strong cooling force but low enough to allow reaching temperatures on the order of  $10 \mu K$ . Considering that the potential of our optical lattice is only  $50 \mu K$  deep, this transition is a must to be able to trap our Yb atoms in the optical lattice.
- The  $^1S_0$ - $^3P_0$  yellow transition at 578.4 nm is used as the clock transition. Two issues make this transition a strongly forbidden one. First, the transitions between manifolds are spin-flip forbidden, as we already discussed previously. But the main reason behind its long lifetime is the fact that the decay to the  $^1S_0$  ground state is not permitted ( $j=0 \rightarrow j=0$  is not allowed). For atoms with no nuclear magnetic moment, photons cannot decay down to the  $^1S_0$  state. That's why the first experiment to observe the  $^1S_0$ - $^3P_0$  transition was done using a fermionic isotope at NIST in 2005 [75]. In the presence of a nuclear magnetic moment, an intermediate mixing between the  $^3P_1$  and  $^1P_1$  states on the one hand, and the  $^3P_0$  state on the other hand takes place. As a result, the lifetime for the  $^3P_0$  state is around 20 s for the fermionic isotopes  $^{171}\text{Yb}$  and  $^{173}\text{Yb}$  [39]. The same group at NIST showed a year later that it is possible to excite this state in  $^{174}\text{Yb}$  if a nonzero electric dipole transition probability at 578.42 nm was induced using a small static magnetic field [76].

## 4.2 The Vacuum System

The vacuum system in our experiment is designed to be compact so that it occupies a minimal space on the transportable optical table. This has been achieved by minimizing the volume of the different parts and connecting them together to form a compact vacuum system. The vacuum system consists of a main chamber, a Zeeman slower, a spectroscopy cell and two atomic ovens (see figure 4.2).

The main chamber has a cylindrical shape and possesses 10 ports, 8 of which are

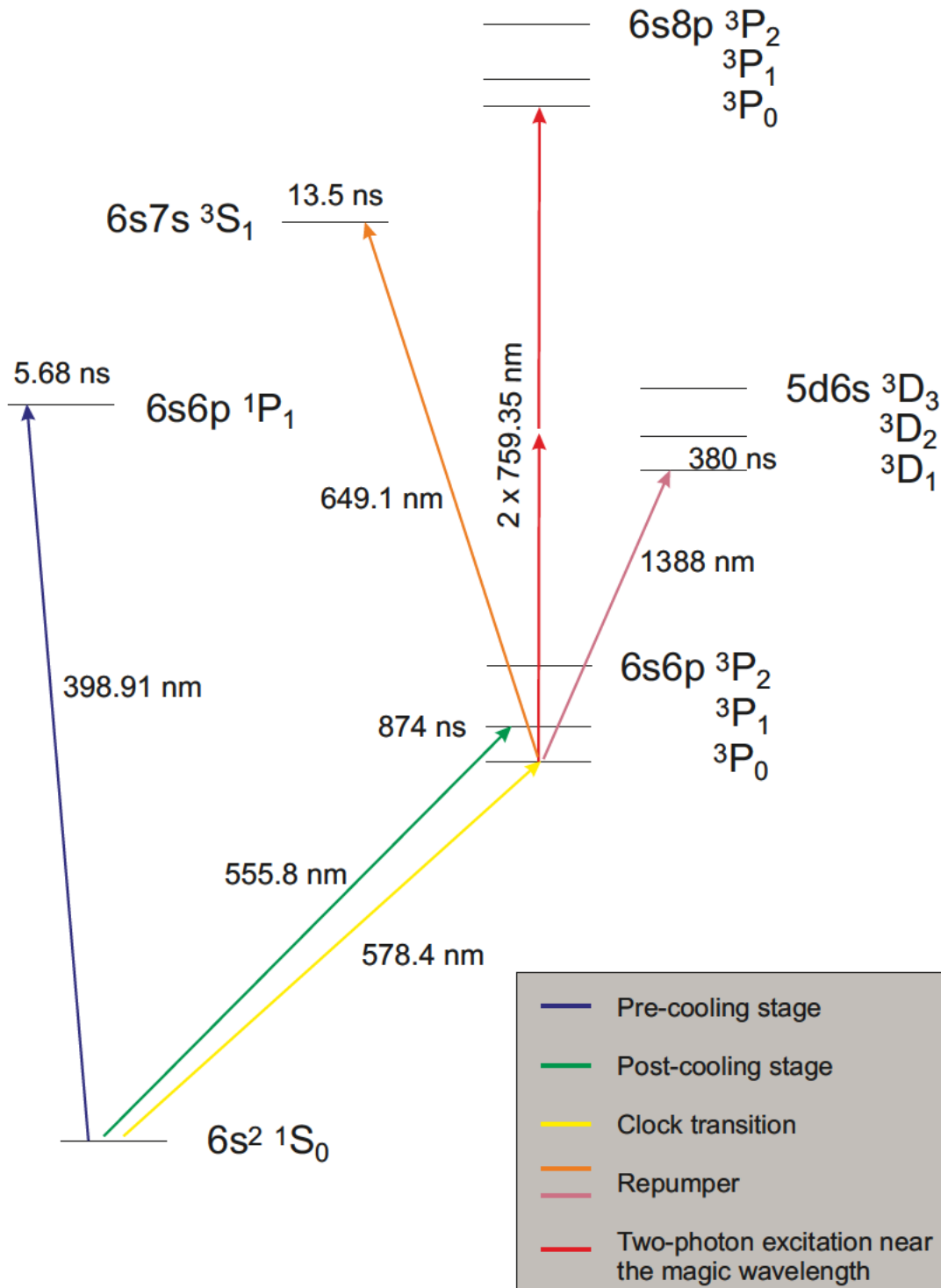


**FIGURE 4.1:** The Yb atomic energy levels showing the relevant transitions for an atomic clock. The fine structure splitting is not to scale [58] [72] [4] [77].

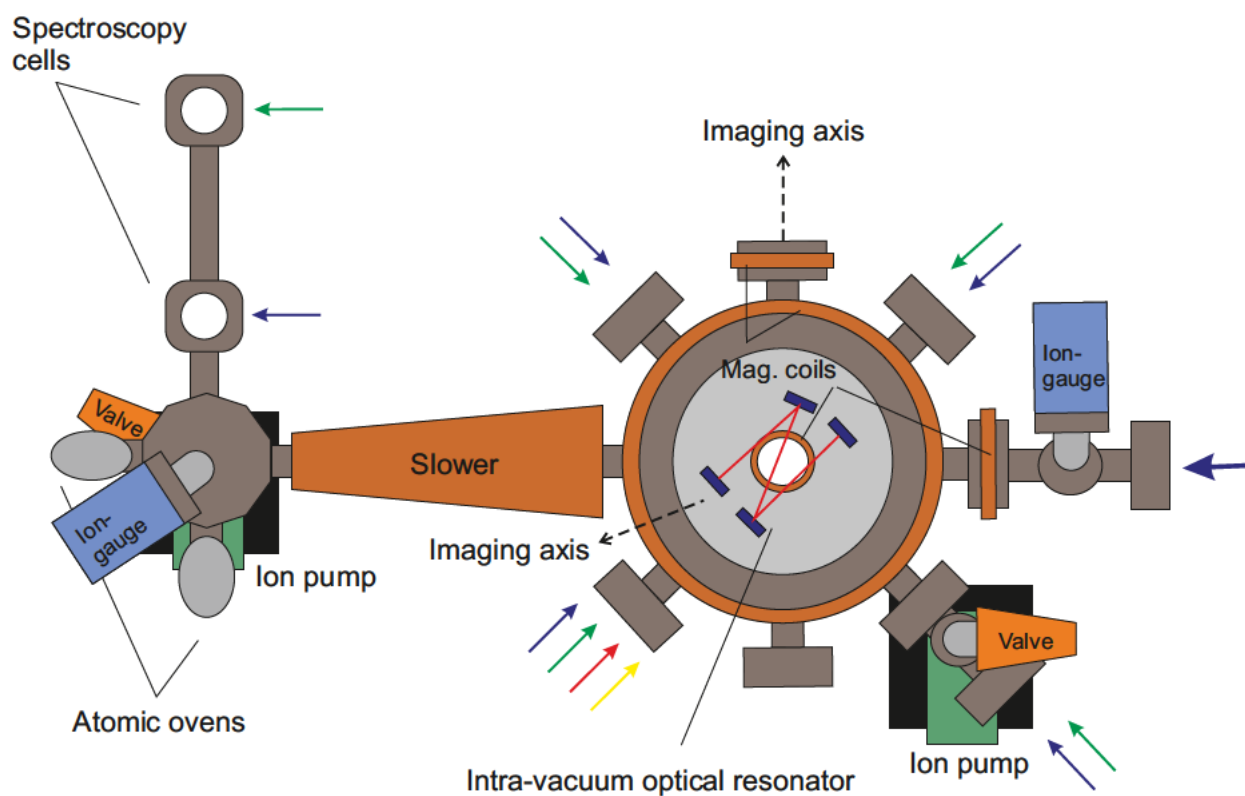


**FIGURE 4.2:** The complete vacuum system consists of the main chamber, Zeeman slower, secondary chamber, and spectroscopy cells. The valves used for mechanical pumping, ion pumps, ion gauges, magnetic coils and the intra-vacuum resonator are also included. The four magnetic coils, sketched as dark-brown rings, that are mounted on the main chamber, generate the magnetic fields needed for cooling and trapping the atoms.

used for optical access. All 10 ports employ knife-edge seals. The 2 main ports of the main chamber are CF 100. One port has a full size window attached to it. This gives us a good optical access for manipulating and imaging the atoms inside the main chamber. The second CF 100 port is parallel to the first port and lies on the opposite side of the main chamber. A closed flange with an opening at its center is attached to this port. This construction is designed to fix the optical resonator for the optical lattice inside the vacuum chamber. The small window at the center of this metallic construction allows the incident and the reflected MOT beams to pass through. The other ports of the chamber vary between CF 35 and CF 16. The spectroscopy cell and atomic ovens are separated from the main chamber by the Zeeman slower. This keeps the temperature of the main chamber unaffected by the ovens whose operating temperatures are around 550 °C.

Pumping the vacuum chamber is done by 2 ion pumps. The first is attached to the main chamber, while the second pumps the region where the atomic ovens are located. The leakage rate detected in our vacuum system was below  $10^{-9}$  l/s. Having a pumping rate of 20 l/s, the ion pumps can bring the system to a pressure below  $10^8$  mbar in a few days after closing the system. The operating pressure now inside the chamber is around  $10^{-9}$  mbar. This results in a vacuum limited atomic trap lifetime of approximately 600 ms. The pressure inside the chamber is monitored with 2 ion gauges attached to both ends of the chamber and connected to a Varian Multi-Gauge device which displays the actual values.

### 4.2.1 The Atomic Ovens

Two different atomic ovens are used, one for the experiment and the other for spectroscopy. The one for the spectroscopy is a WATLOW Mini K-Ring oven. It is heated up to 500°C when doing spectroscopy on the atoms. The atomic beam is collimated by using three copper disks along the spectroscopy setup, with 4 mm holes in the middle. This would block atoms with horizontal velocity components. The result is a vertically collimated beam which would suppress the Doppler effect in our spectroscopy signal. As it is shown in figure 4.2, the spectroscopy setup is built such that the spectroscopy signal for the narrow  $^1S_0$ - $^3P_1$  transition at 556 nm is obtained from the spectroscopy cell that is at maximum distance from the atomic oven. The reason for that is the better collimation of the atomic beam at that position, after the atoms have travelled the maximum distance and have been filtered by the three copper disks. For the broader  $^1S_0$ - $^1P_1$  blue transition, the situation is less critical. Therefore, the lower spectroscopy cell is used for that transition.

The oven used for the experiment is self-made. The body is a metallic cylinder with diameter  $R = 1.5$  cm and length  $L = 6$  cm. A cylindrical body forms the oven and is slid over the one where the Ytterbium is embedded. At operation, the oven is heated up to around 450 °C and consumes approximately 35 Watts of power. The collimation of the atomic beam is also done using 2 gaskets with 4 mm holes, separated by a distance of 25 mm.

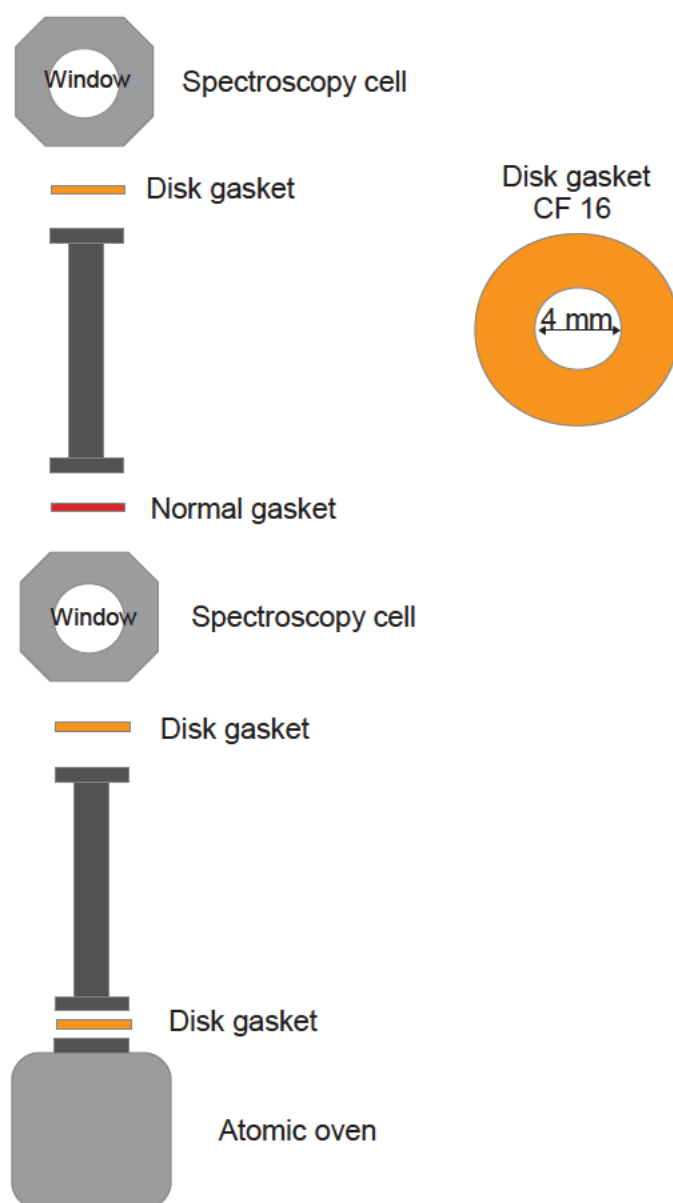


**FIGURE 4.3:** A simplified sketch showing the setup connecting the spectroscopy cells with the atomic oven. Three copper disks have been used to collimate the atomic beam in order to suppress the Doppler effect. The spectroscopy cells are shown with the windows which allow the perpendicular laser beams to cross the collimated atomic beam.

As the ovens are heated up, the Yb atomic-vapor in the oven move randomly in all directions. An atomic beam is formed by exiting the oven through the nozzle with a  $2\pi$  solid angle.

The thermal atomic sample inside the oven has a Maxwell-Boltzmann velocity distribution, given by [78]

$$f(v) = 4\pi \left( \frac{m}{2\pi k_B T} \right)^{3/2} v^2 e^{-\frac{mv^2}{2k_B T}} \quad (4.2)$$

where  $v$  is the atomic speed,  $m$  is the atomic mass, and  $k_B$  is the Boltzmann constant. The most probable velocity can be obtained by setting the derivative  $(df(v)/dv) = 0$ , thus obtaining the value

$$v_{max3D} = \sqrt{\frac{2k_B T}{m}} \quad (4.3)$$

Substituting for the mass ( $m_{Yb}=171 \text{ amu} \approx 284 \times 10^{-27} \text{ kg}$ ) and the temperature (723 K), the most probable velocity is calculated to be around  $265 \text{ m/s}$ . However, due to the fact that faster atoms have a higher probability of exiting the oven, the atoms forming the velocity distribution in the atomic beam is given by [78]

$$F(v) = 2 \left( \frac{m}{2k_B T} \right)^2 v^3 e^{-\frac{mv^2}{2k_B T}} \quad (4.4)$$

The same method used for  $v_{max3D}$  is used to find the most probable velocity for the  $F(v)$  distribution, and is derived to be

$$v_{max} = \sqrt{\frac{3k_B T}{m}} \quad (4.5)$$

Therefore, the most probable velocity for  $^{171}\text{Yb}$  atoms in the thermal beam is about  $323 \text{ m/s}$ . This velocity is essential for the design of the Zeeman slower which will serve to slow the atoms to tens of meters per second before they enter the main chamber.

### 4.3 The Magnetic Fields

As it was shown previously, cooling and trapping the Yb atoms requires the application of a certain magnetic field at the different stages. This section describes the Zeeman slower used in our experimental setup as well as the magnetic coils used for the MOTs.

### 4.3.1 The Zeeman Slower

In the previous section, we studied the kinematics of atoms as they leave the atomic ovens. According to eq. 4.2, the probability distribution under our experimental conditions has its maximum at 323  $m/s$ . A 30cm long Zeeman slower is used to slow the atoms down below the trapping velocity  $v_c$ . The Zeeman slower was designed by Sven Tassy, a previous Ph.D. student in our group, to provide the required slowing effect at a current of 10 A. For the slowing process, the fast  $^1S_0$ - $^1P_1$  transition at 399 nm is used.

The Zeeman slower is an increasing-field slower and therefore provides  $\sigma^-$  cooling. Fast atoms near the oven are resonant with the blue light field. At the position near the oven, the magnetic field is zero. As the slowed atoms move further towards the chamber, an increasing magnetic field  $\vec{B}$  pointing away from the oven shifts the energy of the atoms through the Zeeman effect. The Zeeman shift induced by  $\vec{B}$  on the  $J = 0(m_J = 0) \rightarrow J = 1(m_J = -1)$  transition compensates for the decreasing Doppler shift and keeps the atoms at resonance with the laser light. The increasing magnetic field reaches a maximum of  $B=286$  G at a position close to the chamber before dropping to zero. But a nonvanishing magnetic field extends inside the main vacuum chamber which can disturb the MOT. Thus, an additional magnetic coil is used to correct for this field and provides zero magnetic field at the center of the main chamber.

### 4.3.2 The MOT Magnetic Fields

The magnetic fields required to trap and cool the atoms, as well as the fields required to control the position of the atomic cloud, are produced by four magnetic coils which are fixed externally on the vacuum chamber. Two coils in a near anti-Helmholtz configuration, mounted vertically on the vacuum chamber (see figure 4.2), are responsible for creating the magnetic field gradient required for the pre-cooling and the post-cooling MOTs.

The two coils for the MOTs have different radii due to the vacuum chamber's geometry which is designed such that a large optical axis is available for observation on one side of the chamber. All coils are formed of a copper wire ( $R=5.7 \times 10^{-3} \Omega/m$ ), wound on a water cooled cylindrical ring to prevent heating due to power dissipation. The big coil is formed of a cylindrical ring with an inner radius of 15 cm and an outer radius of 20 cm, on which a total of 84 windings are placed. The small coil is formed of 16 windings on a body, having the same geometry, with a radius spanning from 2.5 to 4.3 mm. Two things have to be taken into consideration when designing the coils. The first thing is the magnetic field gradient needed to trap the atoms in a MOT, which is mainly determined by the small coil in our experimental setup. As a pre-cooling stage MOT, for example, we are using the  $^1S_0$ - $^1P_1$  transition to trap and cool the atoms. Having a linewidth of 29 MHz and a beam diameter of 1 cm, the magnetic field should have a minimum gradient of 40 G/cm. The second parameter to be taken into account is the position at which the magnetic fields of both coils

cancel each other. This sets the trapping position of the atoms. In our setup, the zero point of the magnetic field is given by the position of the optical lattice. Since the resonator for the lattice is a passive intra-vacuum setup, it pre-determines the position of the MOTs. The adjustment of the MOT position can be done by changing the current in one of the coils.

In addition to the coils responsible for the trapping magnetic field, we have two other coils for tuning the MOT position in the directions orthogonal to that of the MOT coils' setup. One coil applies a vertical field while the other produces a field opposing that of the Zeeman slower. As it will be shown later in this thesis, these fields are used for optimizing the transfer efficiencies between the MOTs themselves as well as that between the post-cooling MOT and the lattice. But the most important application is their role in controlling the magnetic field at the position where the clock transition is probed to cancel the Zeeman shift.

## 4.4 The Laser Systems

In this section, the laser systems used for the pre-cooling and post-cooling stages, as well as the lattice and the clock lasers, will be described. In order to keep the experimental setup compact, we use diode lasers for all purposes except for the master laser used for the 555.8 nm transition. There, we substituted the previously used ECDL diode laser at 1112 nm with a fiber laser. The result is a higher stability and narrower linewidth. More about the laser system for the  $(6s^2)^1S_0 - (6s6p)^3P_1$  transition is shown in 4.4.2. The laser systems for the  $(6s^2)^1S_0 - (6s6p)^1P_1$  transition and the optical lattice are described in 4.4.1 and 4.4.3, respectively.

### 4.4.1 The Blue Laser System

The  $(6s^2)^1S_0 - (6s6p)^1P_1$  transition at 398.9 nm, as shown in section 4.1, is the most suitable transition for the slowing and pre-cooling processes in atomic ytterbium. We use two diode lasers in master-slave configuration to generate the needed laser power. The master External Cavity Diode Laser (ECDL) has a Toptica LD-0405-0030-1 diode with a maximum driving current of 55.8 mA. The wavelength selection is done with a grating (3800 lines/mm) in Littrow configuration. The laser diode current and temperature are controlled with a Thorlabs ITC 102 laser diode controller. The power emitted by the laser diode, when operated at 50 mA, is 14 mW (before the isolator). The light from the master laser is used for spectroscopy, injection of the slave laser for the MOT, and slowing the Yb atoms in the Zeeman slower (see figure 4.4).

Two AOMs are used to manipulate the frequency of the master laser. The first is set at 230 MHz and is modulated with a frequency of 100 kHz. After the laser beam makes a double-pass through the AOM, it is directed to the spectroscopy cell. The addition of 460 MHz to the laser frequency is due to the Zeeman slower's  $\sigma^-$

configuration. The resonant blue light used to excite the  $^1S_0 - ^1P_1$  transition is re-collected from the spectroscopy cell by a photomultiplier. The resultant dispersive signal is then used to stabilize the master laser through a feedback signal from a Lock-In amplifier. This signal is applied on the piezo element inside the master laser setup. The frequency up-shift for the injection-light that feeds the slave laser is done by another AOM. This AOM frequency is set to 160 MHz. The laser beam again makes a double-pass through the AOM, thus gaining 320 MHz, before injecting the slave laser. The remaining frequency shift is compensated for by another AOM that is placed in the path of the slave laser's beam.

For the slave laser, a Nichia NDHV310APC laser diode at 401 nm is used. To get it emitting at 399 nm, the diode is cooled down to 5 °C. The slave laser serves as a power amplifier for the master, and carries its characteristics. Its maximum current of operation is 87.7 mA, which results in 60 mW of laser power. It is however operated at a current near 60 mA in order to insure an extended diode lifetime. Through taking the losses induced by the optical isolator, the optical elements, and the acousto-optic-modulator (AOM) into account, we are only left with around 10 mW of optical power for the MOT operation. The light field used for the blue MOT is detuned by around 20 MHz from the atomic transition. This total detuning is obtained from summing the detunings coming from the injection beam and that of the switching AOM. The switching AOM is placed in the path of the slave laser beam and is set to 110 MHz. The first order coming out of the AOM is used for the blue MOT. By switching the AOM off, we block the blue light used for the pre-cooling stage and prevent it from reaching the main chamber.

#### 4.4.2 The Green Laser System

The green light required to cool the atoms using the  $^1S_0 - ^3P_1$  narrow transition is produced by frequency doubling infrared laser light at 1112 nm. The master laser is a Koheras Adjustik fiber laser with piezo tuning and has a maximum output power of 10 mW. The fiber laser was introduced to the experiment due to its stability and narrow spectrum which are relevant when taking into consideration the narrow ( $\gamma=2\pi \cdot (180 \text{ kHz})$ ) atomic natural linewidth. The fiber laser is only used to seed the slave diode laser at 1112 nm. The diode laser is driven by a Thorlabs ITC 110 controller and has a maximum output power of 120 mW, out of which 70 mW are used for frequency doubling.

A PPLN waveguide in a single pass configuration is used to generate light at 555.8 nm from infrared light. The crystal contains 21 parallel waveguides. It is 2 cm long and 0.3 cm wide. Under optimized temperature and incoupling conditions, the second harmonic generation conversion efficiency is  $>150\%/W/cm^2$ . From the 70 mW of infrared light sent to the crystal, 8 mW of green light are obtained after the waveguide. A fraction of this power is used for stabilization purposes, while the

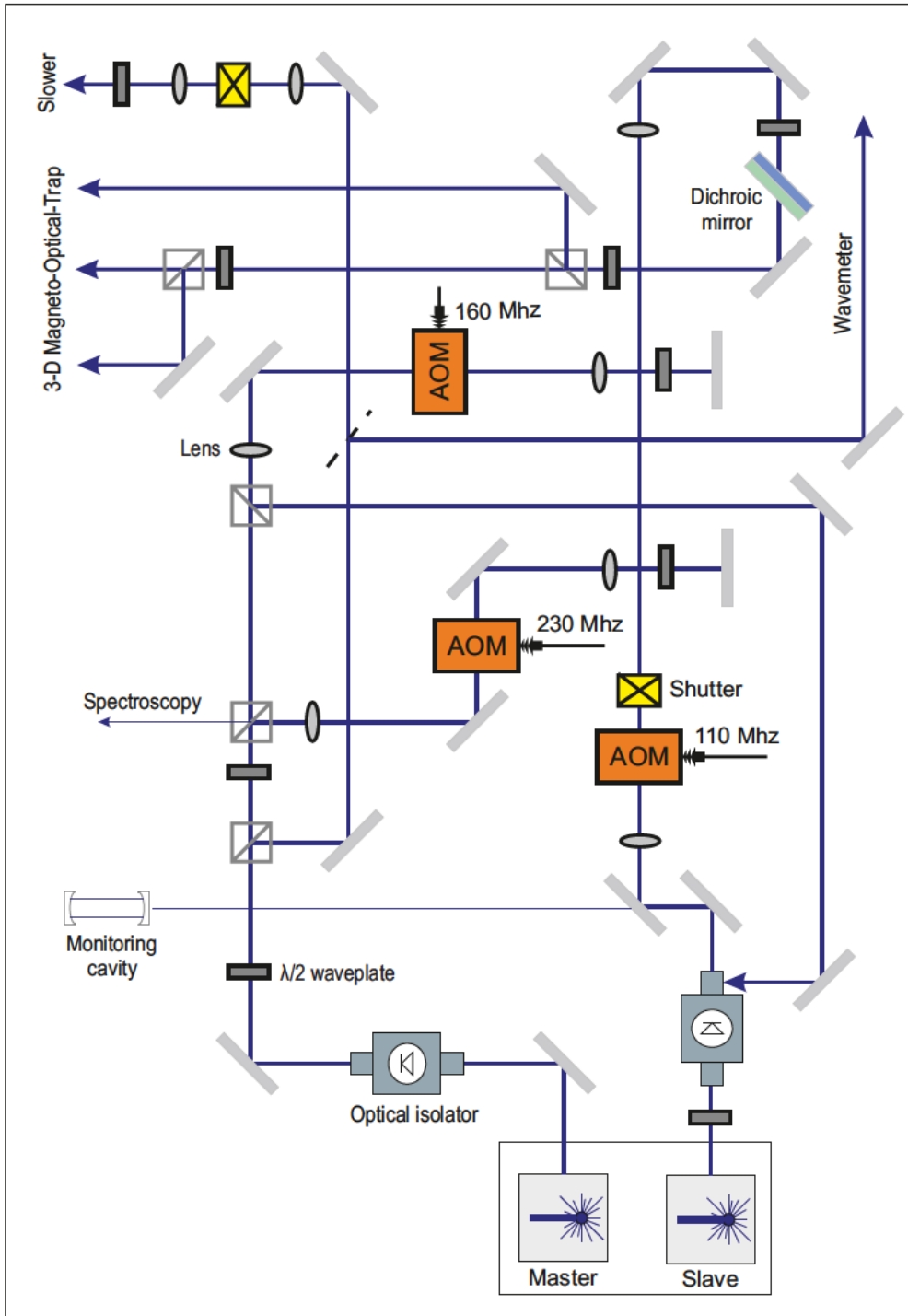


**FIGURE 4.4:** The blue laser setup used for Zeeman slowing and magneto-optical trapping of the neutral Yb atoms.

rest is used for cooling the atoms. The method used to stabilize the fiber laser is similar to that used for the blue master diode laser. The light beam used for the spectroscopy is modulated by 100 kHz and detuned by an AOM operated at 230 MHz. The spectroscopy signal is then collected by a photomultiplier and the feedback signal from the Lock-In amplifier locks the fiber laser on the right frequency. In turn, the light used for the green MOT is manipulated by an AOM which provides the right detuning at the MOT's different phases (see chapter 6). The AOM is operated at a detuning close to -10 MHz from the resonant frequency during the loading phase from the blue into the green MOT. This detuning is optimized for best loading efficiency. To compress and cool the atomic cloud, the frequency is ramped-up to a detuning close to -1 MHz from resonance. This is an essential step before attempting to load the cold atoms in the optical lattice.

### 4.4.3 The Lattice Laser System

The lattice laser system at 760 nm is used to form the optical lattice inside an optical resonator. As mentioned in section 3.4, this trapping process can induce light shifts on the  $(6s^2)^1S_0 - (6s6p)^3P_0$  transition, on the order of hundreds of kHz. Since our clock transition is 8 mHz wide, a perturbation on the kHz level induces a large limitation on the clock uncertainty measurement. To get a Stark shift-free trapping, we have to reduce the relative light shift between the two states involved in the clock transition, written as [58]

$$\Delta\hbar\omega_0 = -\frac{1}{4}\Delta\alpha(\vec{e}, \omega_{laser})E^2 - \dots \quad (4.6)$$

where  $\Delta\alpha(\vec{e}, \omega_{laser})$  is the AC polarizability. I have shown here only the lowest order term of the polarizability which is proportional to the square of the laser electric field and hence the intensity in the optical lattice. Higher order terms are neglected at the moment. Looking at this equation, we see that  $\Delta\hbar\omega_0$  is dependant on the electric field polarization  $\vec{e}$ , the laser frequency  $\omega_{laser}$  and the light field intensity. So to reduce the light shift we have to vary one or more of these parameters. The high intensity at the lattice position is a must to get a strong trapping force, therefore reducing it is not an option. However, what we can do is varying the frequency. As shown in figure 4.6, there exists a wavelength, called the magic wavelength, for alkaline earth-like atoms which gives an equal Stark shift for the ground and the excited states. For the  $^1S_0$  ground state, the AC Stark shift is negative for infrared light and its absolute value decreases with increasing wavelength. The excited states have a large and positive AC Stark shift due to the influence of the  $^3P_0 - ^3D_1$  transition and a large and negative shift due to the  $^3P_0 - ^3S_1$  resonance. The intersection point between the curves representing the ground and the excited states gives the magic wavelength, which was predicted for odd isotopes by Porsev et al. to be 752 nm [39]. The magic wavelength for neutral  $^{174}\text{Yb}$  was measured experimentally to be 759.3537 nm [58].

The lattice laser system is built of two diode lasers in master-slave configuration.



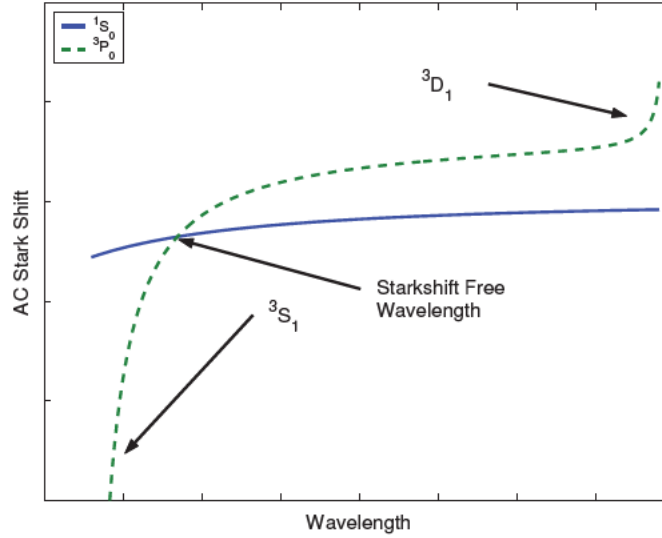


**FIGURE 4.6:** For near infrared light, the light shift due to coupling of the  $^3P_0$  with the  $^3S_1$  and  $^3D_1$  states in alkaline earth-like atoms has an opposite sign. Thus, hitting the right wavelength zeroes the differential polarizability between the  $^1S_0$  and the  $^3P_0$  state [58].

The master laser is a Toptica DL pro 780 operating at 760 nm. The stabilization is achieved using a grating in Littrow configuration. The operating power is 48 mW at a corresponding current of 148 mA, while the maximum power is specified to be 52.9 mW. The DL pro seeds the slave, which is in this case a self constructed tapered amplifier diode laser (m2k TAL-765-1000). The slave laser diode has a maximum output power of 1 W. However, it is operated at only 700 mW to insure an extended diode lifetime. A 60 dB optical isolator between the master and the slave laser suppresses optical feedback into the master laser diode which can lead to short term frequency instability. This behavior would result in a jittering behavior of the optical potential. That would lead to an increase in the motional energy of the trapped atoms which would eventually be lost from the trap.

### Stabilization of the lattice laser

We have used here the Pound-Drever-Hall technique to stabilize the master laser, which was set up in the frame of a master's thesis [1]. This is a fast and powerful method to lock the laser to a resonator or cavity. In our experiment we have stabilized the laser directly to the enhancement cavity for the optical lattice (see section 4.5). The main idea behind the PDH method is using the phase shift between the incoming wave and the reflected wave from the cavity in order to stabilize the laser frequency ( $\omega_{laser}$ ). To do that, we overlap both beams and detect them using a photodiode. When  $\omega_{laser}$  is perfectly resonant with the cavity, the resulting phase difference is  $\Delta\varphi = -180^\circ$ . This implies that at resonance, the incoming and the reflected fields interfere destructively and the power  $P_{tot} = 0$ . If  $\omega_{laser}$  drifts then  $P_{tot} \neq 0$  and a correction is necessary. What is still unknown here is in which direction the laser

drifted. Therefore, an EOM (Thorlabs EO-PM-NR-C1-EO) modulated at 12.5 MHz is introduced to the setup as a phase modulator. The result are sidebands at the modulation frequency. The sidebands are spectrally well separated from the carrier so that incoupling into the resonator is not possible. Thus, they are back-reflected from the resonator's incoupling mirror. The well defined phase of the 2 back-reflected sidebands with respect to the incident and reflected beam can be used to extract the phase of the reflected beam. It is achieved by beating the three waves together and reading the phase of the beat pattern. The power  $P_{tot}$  detected by the photodiode can be quantitatively written as [79]

$$\begin{aligned}
P_{tot} = & (P_c |F(\omega_{laser})|^2 + P_s |F(\omega_{laser} + \Omega)|^2 + |F(\omega_{laser} - \Omega)|^2 \\
& + 2\sqrt{P_c P_s} \text{Re} [F(\omega_{laser})F^*(\omega_{laser} + \Omega) - F^*(\omega_{laser})F(\omega_{laser} - \Omega)] \cos\Omega t \\
& + 2\sqrt{P_c P_s} \text{Im} [F(\omega_{laser})F^*(\omega_{laser} + \Omega) - F^*(\omega_{laser})F(\omega_{laser} - \Omega)] \sin\Omega t \\
& + (\text{terms oscillating at frequency } 2\Omega)
\end{aligned} \tag{4.7}$$

Here  $F$  is the reflection coefficient given by the ratio of the electric fields of the reflected beam and the incident beam,  $P_s$  is the power in each first-order sideband,  $P_c$  is the power in the carrier, and  $\Omega$  is the sideband frequency. This signal is detected by a fast photodiode (20MHz) and sent to a Digilock 110 feedback controller. The terms due to the interference of the sidebands with each other in eq. 4.7 are irrelevant for us, so they are neglected. Information about the carrier's phase is contained in the terms oscillating at the modulation frequency  $\Omega$ . Experimentally, these terms are filtered out from eq. 4.7 using a low pass filter and a mixer. If we consider for example the mixing of the modulation signal at  $\sin(\Omega t)$  with another signal at  $\sin(\Omega' t)$ , the product of both sine waves would be [79]

$$\sin(\Omega t)\sin(\Omega' t) = \frac{1}{2}\cos[(\Omega - \Omega')t] - \frac{1}{2}\cos[(\Omega + \Omega')t] \tag{4.8}$$

Since we are interested in the situation where  $\Omega = \Omega'$ , the term  $\cos[(\Omega - \Omega')t]$  will be a DC signal that can be factored out by a low pass filter.

The product of the modulation signal and the oscillating term at  $\Omega$  in eq. 4.7 is used as the input to the PID controller. The Digilock 110 contains 2 PID controllers. PID1 acts on the laser's DC modulation current. An integrated cut-off frequency for the integral part prevents it and PID2 from accumulating offsets in opposite directions. On the other hand PID2 acts on the laser's external grating through the piezo. Thus, PID1 corrects for short term disturbances while PID2 takes care of the long term drifts.

#### 4.4.4 The Yellow Laser System

As already mentioned, this thesis is part of a collaboration between the groups of Prof. Axel Görlitz and Prof. Stephan Schiller. The latter group is responsible for

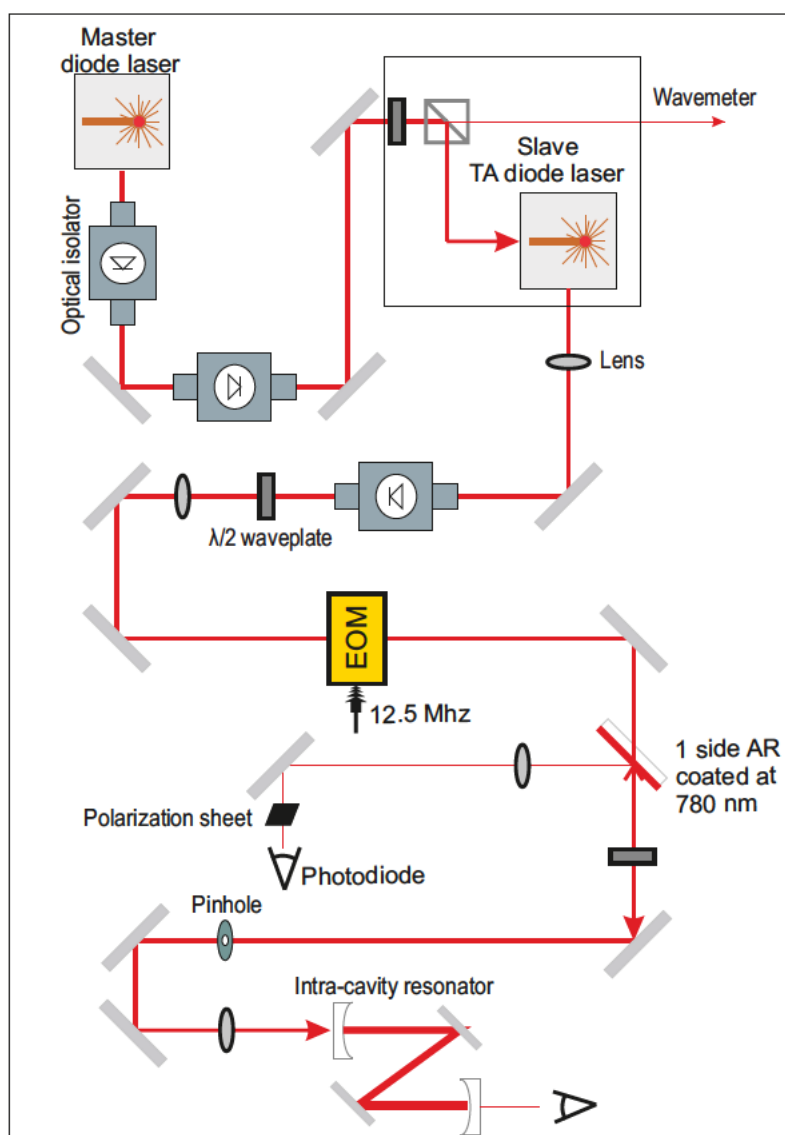


**FIGURE 4.7:** The near IR laser setup used for optically trapping the Yb atoms inside the optical lattice.

producing the yellow light required to excite the  $^1S_0 - ^3P_0$  transition at 578 nm for clock operation [80] [81]. The measurements shown in this thesis were taken using a setup based on frequency doubling light from a DL-Pro 100 diode laser. This setup has the advantages of having a high stability, a large scanning range, and it occupies a moderate volume. This section will summarize the status of the yellow laser system at the time the measurements were done, and will present the experimental results.

Light at 1156 nm used for frequency doubling is obtained by a commercial Topica DL-Pro 100 diode laser in Littrow configuration with an integrated isolator. The maximum output power of the laser diode is 97 mW, and it can be scanned up to 20 GHz without mode hopping. The laser is operated at 73.5 mW and its center wavelength is at 1156 nm. The laser current, temperature stabilization, and scanning signal are provided by commercial DCC 110, DTC 110, and SC 110 controllers, respectively. The yellow light is generated from infrared light by a 2 cm long PPLN crystal with 22 parallel waveguides (HC Photonics). The crystal used is identical to that built into our green laser system. While a coupling efficiency of 45% was achieved when using a bare fiber, only 30% were possible for free-space incoupling, but with a better reliability. At the optimum temperature, which was measured to be somewhere between 15°C and 20°C depending on the waveguide tested, the conversion efficiency was measured to be 160%/W/cm<sup>2</sup>, which is in agreement with the specifications of the crystal. For 12.5 mW of laser radiation at 1156 nm, about 200  $\mu$ W of yellow light were extracted.

### Stability of the clock laser system

The DL-Pro is stabilized through the yellow light on a ULE cavity. The yellow radiation exiting the PPLN crystal is locked using the Pound-Drever-Hall (PDH) method, which was explained in section 4.4.3 for the lattice laser system. A 10 cm long ULE cavity with a finesse that exceeds 300000 at 578 nm is used for this purpose [81]. The cavity is placed inside an evacuated aluminum chamber at  $8.5 \times 10^{-8}$  mbar. It is designed such that the accelerations due to mechanical vibrations along its length are minimized [23] and is mounted on an active vibration isolation system. An additional isolation from the environment is provided by a temperature controlled copper box inside vacuum with a thin gold layer. The aluminum and copper chambers are both temperature stabilized using peltier elements. This reduces the cavity's length fluctuations due to thermal effects and leads to a better stability.

### The laser frequency drift

One of the most important parameters that have to be precisely known is the laser frequency drift. The very narrow  $^1S_0 - ^3P_0$  clock transition with a natural linewidth on the order of 10 mHz [58] can only be detected spectroscopically if the laser frequency is well identified. Since the drift of the laser frequency is very stable, the drift rate can be corrected for before starting a spectroscopy measurement. To measure the drift rate, a fraction of the IR light is sent to the frequency comb as shown in figure 4.9 and its beatnote with one of the comb lines is measured.

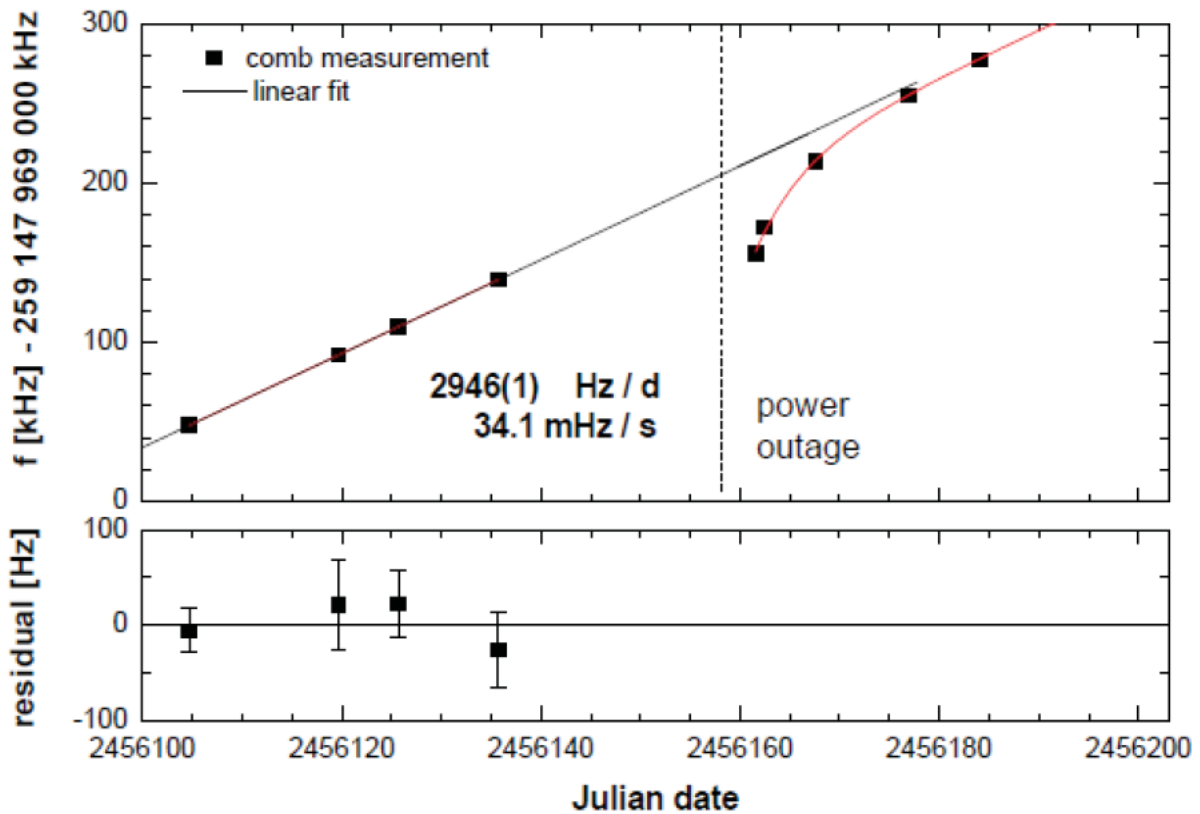


FIGURE 4.8: The drift of the clock laser, measured by beating the IR laser with a line of the frequency comb. The linear fit is only done over the first four data points since the vacuum pump of the ULE cavity suffered a power outage, which is indicated by the dashed line. The fit after the power outage shows first a non-linear behavior and an offset of several tens of kHz. The error bars shown in the lower scheme are those of the frequency comb for the different measurements.

A measurement of the frequency drift over a period of around 80 days is shown in figure 4.8. The linear fit of the first measurements corresponds to a drift of 34.1 mHz/s. This well determined drift was lost after a power outage of the ULE cavity vacuum pump. The first frequency measurements after re-evacuating the cavity showed an offset of several tens of kHz in addition to a non-linear drift behaviour, which eventually comes close to the previously determined drift rate.

#### The connection of the yellow clock laser to the Yb atomic source

As already mentioned, the clock laser is located in a different laboratory than the ultra-cold Yb source. For this reason, 2 optical fibers and three electrical cables are installed between both laboratories to allow optical and electrical communica-

tions. The effective distance between both laboratories is 350m. The first optical fiber (Fibercore SM450) is used for the frequency doubled light at 578nm, while the second (Fiber Nufern 1060-XP) serves to transport the 1156nm radiation. For practical reasons we decided to transport light at 1156nm to our laboratory where the cold atoms are prepared and do the frequency doubling there. An additional PPLN waveguide is used to produce yellow light, whose frequency is then manipulated by an AOM to scan over the clock transition. To overlap the clock laser beam with the atomic cloud, yellow light is coupled into a fiber and the output is then overlapped with resonant green light. The fluorescence from the  $^1S_0 - ^3P_1$  transition ensures that the light beam inside the vacuum chamber is at the position of the trapped atoms.

But the method of connecting both laboratories has its disadvantages. The perturbations on the optical fiber induce a spectral broadening, measured to be about 180 Hz over the whole fiber length [18]. Therefore, an active stabilization technique was built by the group of Professor Stephan Schiller to cancel these effects, following the scheme presented by Ma et. al. [82]. To do that, a small fraction of light is retro-reflected into the fiber after the output using a BK-7 glass plate and is sent back to the laboratory where the clock laser is located. After undergoing a double pass through an AOM placed before the fiber incoupler and operated at 40 MHz, the retro-reflected beam is then overlapped with the initial laser beam and the beat signal is measured. This signal is mixed with that of a local oscillator at 80 MHz. The resultant signal acts on the AOM through a VCO to cancel the perturbations induced by the optical fiber. Using this locking scheme a linewidth  $< 1$  Hz is measured for the beat signal instead of 360 Hz [18].

## 4.5 The Intra-Vacuum Optical Resonator

As it was already explained in section 4.4.3, we are using diode lasers to produce the 760 nm light field for the optical lattice. The relatively low light power that these diodes can provide makes it impossible to create an optical lattice with the required trapping potential and trap volume. The compactness of our experiment doesn't allow to use high power light sources such as Ti-sapphire laser because of their large volume. The solution is to amplify the light emitted by the diode laser with an optical resonator.

The resonator used in our experiment is a 1-D intra-vacuum folded resonator. It was designed and built in the frame of Tobias Franzen's bachelor and master's theses [83] [1]. The setup, constructed from Invar 36, is fixed in the main chamber as shown in figures 4.2 and 4.10. Despite the low linear thermal expansion coefficient that Invar has ( $\alpha = 1.2 \cdot 10^{-6}/^{\circ}K$ ), the magnetic coil glued on the outer side of the same flange still produces enough heat to cause non-negligible perturbations on the resonator. Therefore, an NTC temperature sensor is glued on the outer side of the chamber and a homemade PID controller regulates the temperature oscillations in

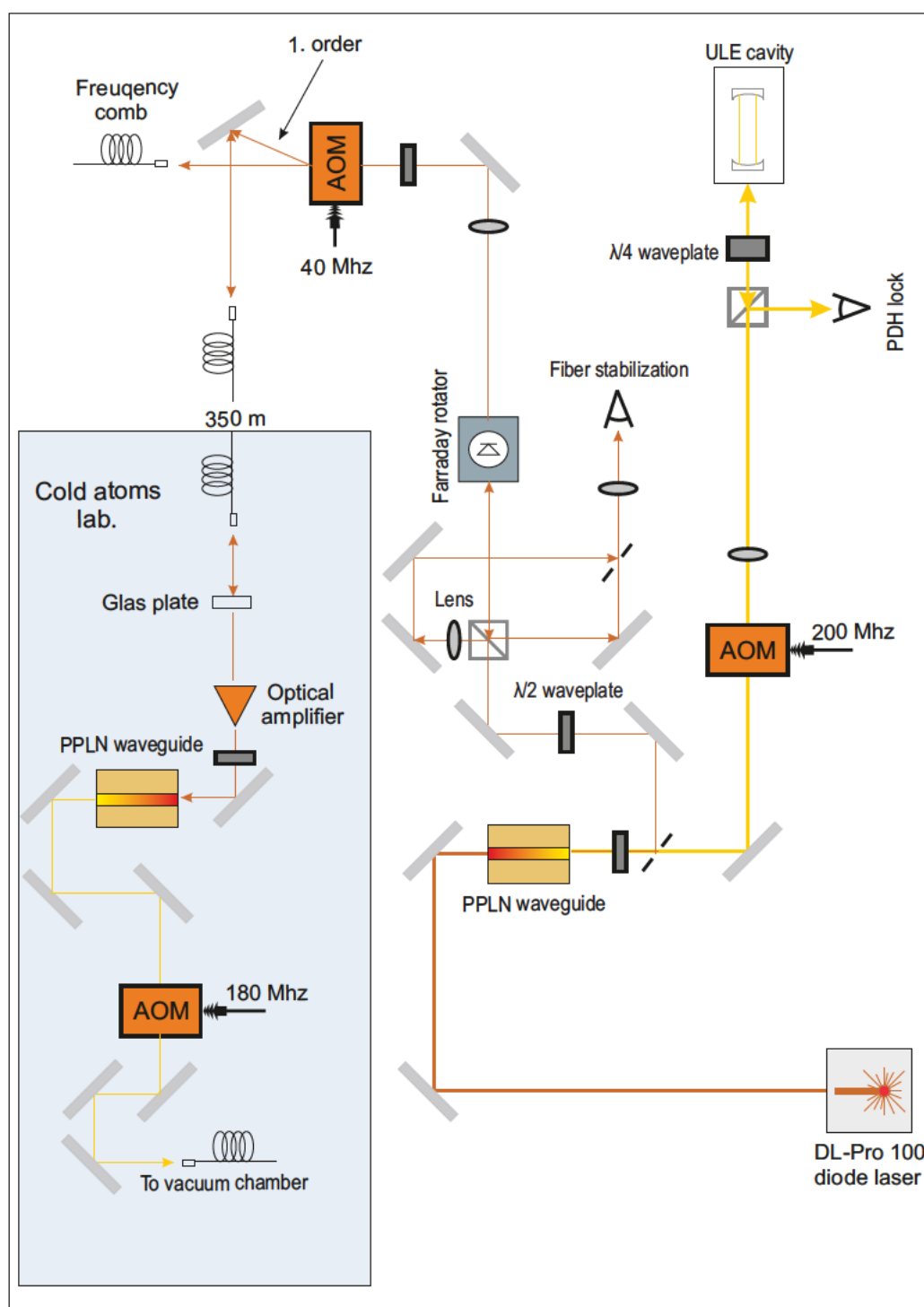


**FIGURE 4.9:** The complete clock laser setup. The marked region on the figure is the extra part built in our laboratory, whereas the rest is built on an optical table with active vibration control in the laboratory where the frequency comb is present.

	760 nm	556 nm	578 nm
Incoupling mirror	99.75%	<1%	<1%
Retro-reflecting mirror	99.75%	<1%	<1%
Rerouting mirrors	>99.95%	>99.95%	>99.95%

**TABLE 4.3:** The mirrors used for the folded intra-vacuum optical resonator and their reflectivities for the different wavelengths.

this region.

The 1-D resonator is 200 mm long and contains 4 mirrors. The incoupling and retro-reflecting mirrors are curved mirrors (radius of curvature 200 mm) selected to form a near-confocal setup. The other 2 mirrors are planar, and their function is redirecting the beam so that the 200 mm light path fits inside the vacuum chamber. The two guiding mirrors are specially designed to reflect at 760 nm, 556 nm, and 578 nm (see table 4.3), and they pre-define the field’s polarization inside the resonator to be perpendicular to the MOT’s magnetic field. On the contrary, the in-coupling and out-coupling mirrors transmit light at 556 nm and 578 nm. This allows us to determine the position of the 760 nm light through overlapping the 556 nm light with it. The cavity is scanned by a piezo that is attached to the back-reflecting mirror. External manipulation of the piezo is possible through integrated electric pins on one vacuum port. Light for the clock measurement is also aligned with the lattice light field to make sure that it hits the cold atoms. The mirrors are fixed using a NORLAND OPTICAL ADHESIVE 61 UHV glue, cured by UV radiation.

For the system described above, a finesse of 800 is measured. With an incoupling efficiency of 20%, the calculated intra-cavity light power was estimated to be 50 W which corresponds to a potential depth of 200  $\mu$ K. After examining it experimentally, we measured a lower potential depth of approximately 50  $\mu$ K. The experimental results are shown in chapter 5.

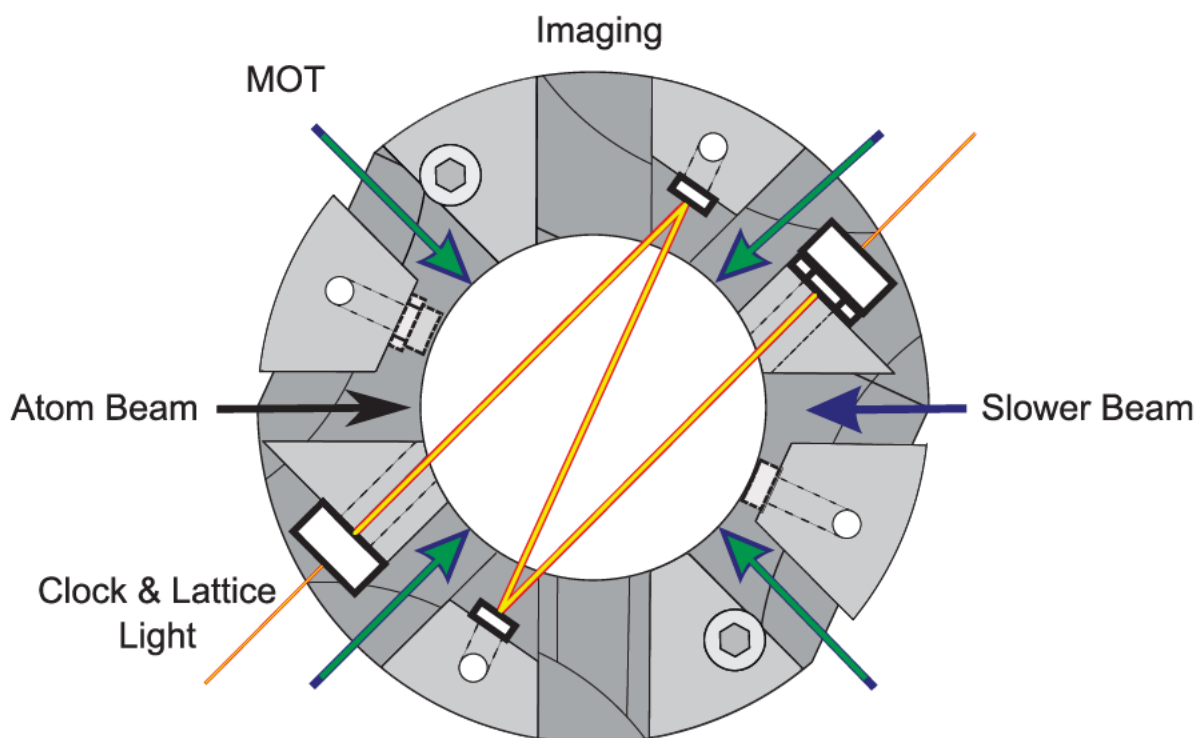


**FIGURE 4.10:** The 1-D intra-vacuum resonator. The laser beams for the pre-cooling and the post-cooling MOTs are sketched as overlapped blue and green arrows. The blue arrow coming from the right crosses the setup and passes through the Zeeman slower, till it reaches the atomic oven. From the left, the light at the magic wavelength enters the resonator, and is reflected in a z-form, as shown in the figure. When doing spectroscopy on the Yb atoms, the yellow laser beam is overlapped with the trapping beam, which is the best method allowing for an easy allignability. As mentioned, the vertical axis is kept free for imaging purposes [1].



# Chapter 5

## Characterization of the Ultracold Atomic Source

In this chapter, the preparation phases for the spectroscopy on the clock transition and the characterization of the ultra-cold atomic cloud in each of those phases will be discussed. The process of cooling the ytterbium atoms from hundreds of Kelvin to the  $\mu\text{K}$  level starts by slowing the atoms using the Zeeman slower before trapping them in the pre-cooling MOT. The pre-cooling stage cools the atoms down to the mK level and prepares the atoms to be loaded into the post-cooling stage MOT. The post-cooling stage MOT brings the atomic temperature down to a few tens of  $\mu\text{K}$ . This step is essential in order to be able to trap the atoms in the optical lattice, which has a potential depth around 50  $\mu\text{K}$ . The experimental parameters for each phase are summarized in figure 5.1, and they will be discussed thoroughly throughout this chapter.

### 5.1 Loading of the First Stage MOT

This is the process in which the atoms slowed by the Zeeman slower get trapped in the first stage MOT. The atoms leaving the atomic oven are exposed to a varying magnetic field, created by a wound coil, that keeps them at resonance with the laser beam @ 399 nm throughout the slowing region (see section 4.3). The slowing region is defined by the coil's length, which is a 30 cm long tube in our experimental setup. Atoms leaving the Zeeman slower have an average velocity around 40 m/s, which is within the capture velocity of the first stage MOT. The trapping volume of the MOT is defined by our 1 cm wide blue laser beams. The rate at which the number of atoms changes in the MOT depends on the loading rate ( $R$ ) on one hand, and the loss rate ( $N/\tau$ ) on the other hand [84]

$$\frac{dN}{dt} = R - \frac{N}{\tau} \tag{5.1}$$

where  $N$  is the number of atoms in the MOT and  $\tau$  is the MOT's lifetime. If we consider initially that no atoms are present in the trap, we get the boundary condition

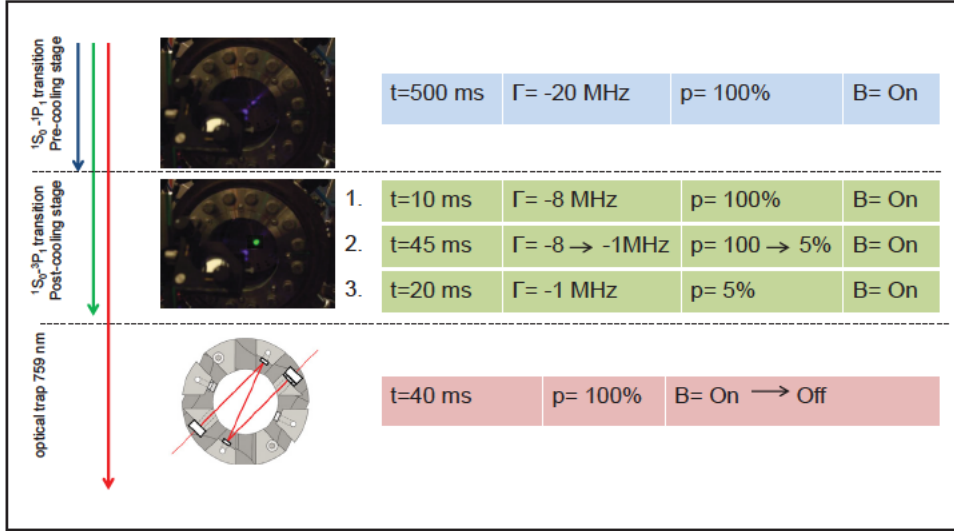


**FIGURE 5.1:** The sketch shows the experimental sequence starting with the pre-cooling stage and ending with the trapping of atoms in the optical lattice. The blue, green and red arrows on the left represent the laser to which the atoms are exposed to at the given stage. The time span of each phase together with the laser detuning, laser power and the magnetic fields during that phase are shown on the right, respectively.

$N(t=0)=0$ . The solution for the differential equation 5.1 is then

$$N(t) = N_s(1 - e^{-t/\tau}) \quad (5.2)$$

with  $N_s$  being the steady-state atom number in the trap after the trap has been loading for a time  $\tau$ . In this expression, only the single-body decay rate is relevant. In our experiment, the two-body decay rate is considered to be very small compared to the one-body decay rate. That's because of the moderate light intensity used to trap the atoms, and a vacuum pressure exceeding two times in the  $10^{-9}$  mbar at operating conditions. Thus, on one hand the atomic density is not high enough, and on the other hand the probability of a cold atom colliding with background gas is not negligible. Thus, we assume that the limiting mechanism for our first stage MOT is the one-body loss due to collisions with the background gas.

Measurements of loading times below 300 ms for the blue MOT have been observed at a vacuum pressure on the order of  $10^{-11}$  bar. The blue laser beam sent along the Zeeman slower was blue detuned and had a power of 2 mW. The magnetic fields for the Zeeman slower and the MOT were adjusted for minimum loading times (see section 4.3). The best values were recorded at a magnetic field gradient of 70 G/cm on the MOT side, as shown in figure 5.2. The parameters were however optimized later for the highest atom number and the best transfer efficiency into the second stage MOT. Thus, loading times between 500 ms and 1.5 s were adopted during the spectroscopy measurements shown later on.

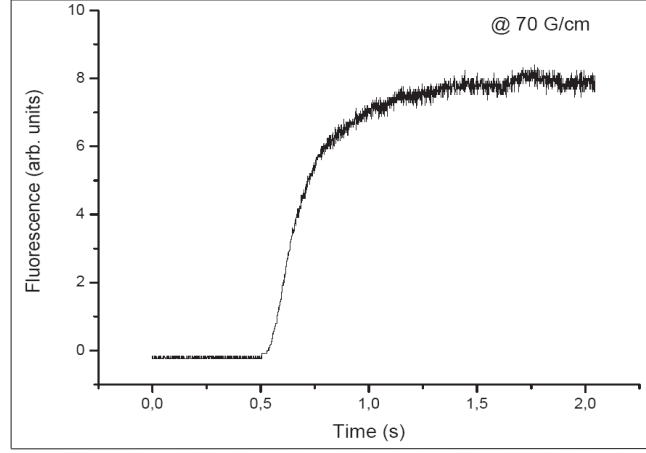


**FIGURE 5.2:** Loading curve of  $^{174}\text{Yb}$  in the first stage MOT. The best loading rate was obtained when the MOT was operated at magnetic field gradients close to 70 G/cm.

## 5.2 The Atom Number

We determine the number of atoms trapped in a MOT or in the optical lattice by using fluorescence imaging. Detection is done by the CCD camera mounted along the vacuum chamber's vertical axis (see figure 4.2). The relation for extracting the atom number from the fluorescent light is

$$N = \frac{P_{tot}}{\Gamma h\nu_{laser}} \quad (5.3)$$

The total light power emitted by the atomic cloud,  $P_{tot}$ , is calculated by integrating the light detected by the CCD camera ( $P_{det}$ ) over the whole solid angle. In addition to that, the aperture of the first imaging lens and the transmission through the optical elements,  $\beta$ , are included in the calculation. The relation is then expressed as

$$P_{tot} = (4\pi r_{lens}^2) P_{det} / \pi d^2 \beta \quad (5.4)$$

where  $d$  is the distance of the first imaging lens from the atomic cloud. Another important parameter for calculating  $N$  is the scattering rate  $\Gamma$ . The scattering rate of atoms excited with light near resonance is [61]

$$\Gamma = \frac{\gamma}{2} \left( \frac{s_0}{1 + s_0 + (2\delta/\gamma)^2} \right) \quad (5.5)$$

where,

- $s_0 = I/I_s$  is the ratio of the saturation intensity to the probe light intensity
- $\delta$  is the light detuning from the transition used for imaging

Atomic properties	Value
Saturation intensity, $I_s$	572.4 W/m <sup>2</sup>
Probe transition linewidth, $\gamma$	$2\pi \times 28$ MHz
Laser frequency, $\nu_{laser}$	$7.5 \times 10^{14}$ Hz
Experimental quantities	Value
Probe light intensity, $I$	100 W/m <sup>2</sup>
Radius of the 1 <sup>st</sup> imaging lens, $r_{lens}$	25 mm
Distance between atoms and 1 <sup>st</sup> lens, $d$	21 cm
Total transmission through optical elements, $\beta$	0.63

**TABLE 5.1:** The atomic properties and experimental characteristics relevant for calculating the atom number using the fluorescent imaging method.

- $\gamma$  is the transition linewidth

With this, when imaging at resonance, the detuning is  $\delta = 0$  and thus equation 5.5 reduces to

$$\Gamma = \frac{\gamma}{2} \left( \frac{s_0}{1 + s_0} \right) \quad (5.6)$$

The expression for the atom number  $N$  can be re-written to include the atomic properties and the experimental parameters as follows

$$N = \frac{8r^2 P_{det} (1 + s_0)}{\gamma h d^2 \beta \nu_{laser} s_0} \quad (5.7)$$

The transition used to image the Yb atomic cloud is the fast  $^1S_0 \rightarrow 1^1P_1$  transition at 399 nm because of its high scattering rate. To do that, we use the same light beams used to generate the blue MOT, but with the detuning turned to zero. The light emitted by the atoms first crosses a window and two lenses, and is reflected by one mirror, before getting detected. Losses due to those optical elements, as well as other technical and intrinsic data required for calculating the atom number, are shown in table 5.1.

The atom number in the blue MOT varied with the position of the MOT. The limitations were mainly the different loading rates at the different positions. The

limited optical access on the diagonal axes limits the adjustability of the MOT. At the position defined by the optical lattice, the number of  $^{171}\text{Yb}$  atoms trapped in the blue MOT is  $1.5 \times 10^6$  atoms  $\pm 16\%$ . The total laser power available for the blue MOT was 3.8 mW, measured just before the vacuum chamber.

The loading process into the green MOT follows by switching the blue light field off and exposing the atoms to a total of 4 mW of green laser power close to the  $^1S_0$ - $^3P_1$  transition at 556 nm. The diameter of the laser beam is 0.7 mm, illuminating the atomic cloud from all three axes, as shown in figure 4.2. The transfer efficiency into the green MOT, at the working position, is approximately 6%. However, transfer efficiencies close to 10% were measured at random positions, where the blue MOT and the green MOT were aligned to yield maximum transfer efficiency. The lower transfer efficiency at the position of the optical lattice is mainly due to the imperfect alignment of the optical beams and the magnetic fields. For both values of the transfer efficiency, the optimized green detuning is - 5 MHz and the laser power is set to the maximum value of 4 mW. The number of atoms measured inside the green MOT is  $8.7 \times 10^4 \pm 19\%$  atoms.

### Stability measurement of the green MOT

In an attempt to study the stability of the atom number and density in the green MOT, we performed a long term measurement during which over 1000 experimental cycles were recorded. The evaluation was done for the green MOT in the final phase, after the laser power and the detuning were ramped down to their final values (see figure 5.1). The parameters were ramped down slow enough not to lose a remarkable amount of atoms from the trap. The atomic cloud was compressed to approximately  $170 \mu\text{m}$  and we had an atomic density about  $10^{10} \text{ cm}^{-3}$ .

Throughout the two hours of measurement, the lasers stayed locked and no correction of any of the experimental parameters was necessary. The assigned experimental parameters resulted in a cycle length of approximately 2.5 seconds (see figure 5.1). The cycle starts by loading the blue MOT for about 500 ms. The green MOT is then loaded from the blue MOT in its first stage before being further cooled and compressed in its second stage. The magnetic fields are kept on throughout the whole process. The long-term measurement shows a fluctuation of approximately 20% in the atom number, as shown in figure 5.3. This value depends mainly on the stability of the blue as well as the green laser systems. Higher fluctuations have been observed on cold or hot days. Small temperature variations in the laboratory had a clear fingerprint on the stability of the laser systems. Another important value that was extracted from this measurement is the variation in the cloud width. The  $170 \mu\text{m}$  cloud-width fluctuated by about  $15 \mu\text{m}$  from the mean value (figure 5.3). As it will be shown in section 5.3.1, the radius of the atomic cloud is comparable to that of the lattice's Gaussian beam. Therefore, this may result in shot-to-shot fluctuations in the atom number inside the optical lattice.

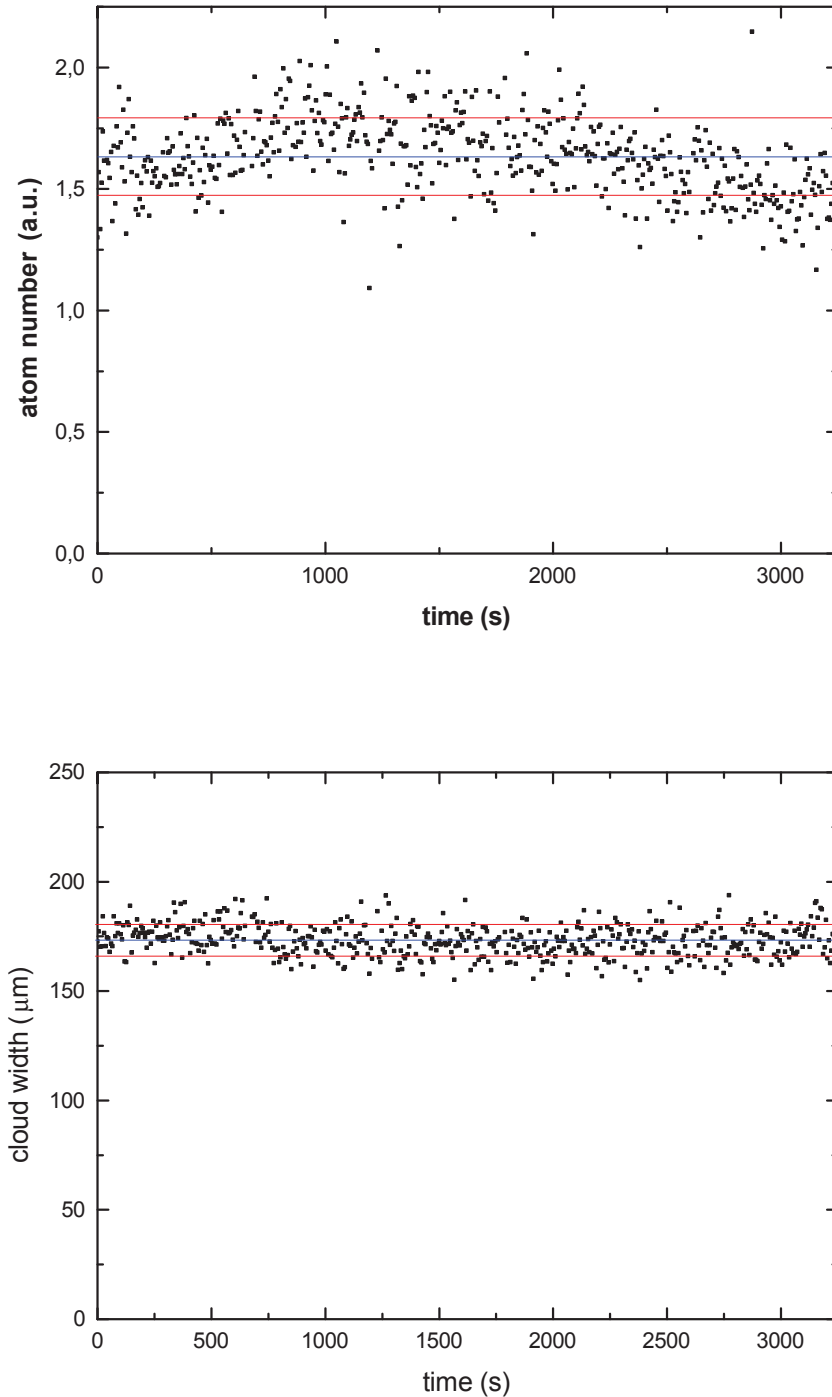


**FIGURE 5.3:** Top: Long term measurement over 3000 seconds showing the stability of the atomic number versus time. Over 1000 experimental cycles were covered in this measurement, in which  $^{171}\text{Yb}$  was trapped and cooled in the pre- and post-cooling stages. The standard deviation marked in red reveals a fluctuation of 9.8% from the mean. Bottom: Graph showing the stability of the atomic cloud width (FWHM of the Gaussian fit) after being cooled and compressed using the  $^1S_0\text{-}^3P_1$  green transition. The mean width is measured to be  $173\mu\text{m}$ , whereas the marks representing the standard deviations show a value of  $166$  and  $180\mu\text{m}$ .

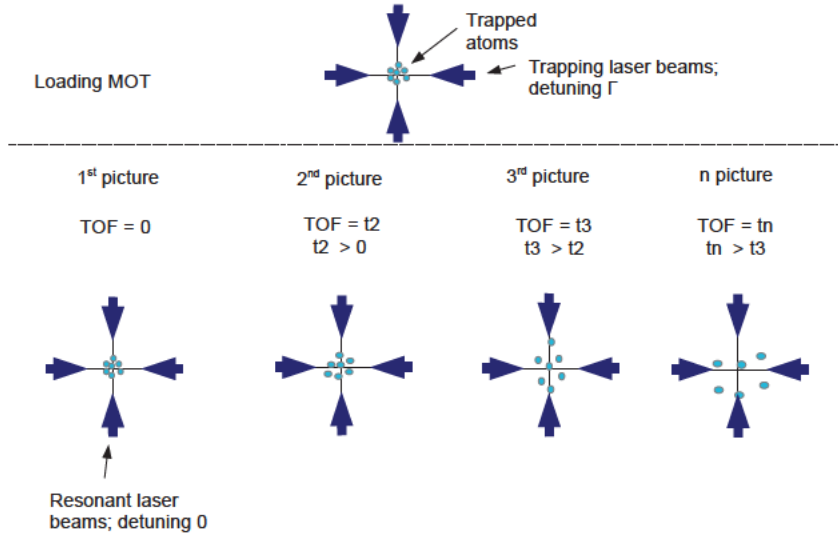


**FIGURE 5.4:** Time-Of-Flight (TOF). The MOT is loaded and then the atoms are released by switching off the laser light field. The atoms' expansion is obtained by taking successive images of the atomic cloud at certain time intervals by flashing the atoms with resonant laser radiation at 399 nm.

### 5.3 Temperature of Atomic Cloud

Temperature measurements were done using the time-of-flight method. To explain this, I will start with a standard expression in thermodynamics relating the temperature to the velocity of particles moving along the  $i$ -axis and having a gaussian velocity distribution [85]

$$k_B T_i = m v_{rms,i}^2 \quad (5.8)$$

When the atoms are released from the MOT, the atomic ensemble undergoes a gaussian expansion. This is done by turning off the MOT's light fields after loading the trap and letting the atomic cloud expand ballistically. The expansion of the cloud during this phase is

$$\sigma_i(t) = \sqrt{\sigma_i^2(0) + \frac{k_B T}{m} t^2} \quad (5.9)$$

where  $\sigma_i(0)$  is the initial width of the cloud along the  $i$ -axis and  $\sigma_i(t)$  is the width after the cloud undergoes an expansion for time  $t$  (see figure 5.4).

In our experiment, temperature measurements of atoms trapped in the first stage MOT are done by taking fluorescence images of the expanding atomic cloud with time intervals of  $200 \mu s$ . The atoms are illuminated with blue resonant light for  $500 \mu s$ . The expansion rate along the different axes is slightly different due to the inhomogeneous trap interaction with the atoms. The temperature of fermionic ytterbium

inside the blue MOT is around  $700 \mu\text{K}$ , whereas the temperatures measured for the bosonic isotope  $^{174}\text{Yb}$  were around  $3 \text{ mK}$ . The fast  $^1S_0\text{-}^1P_1$  transition at  $399 \text{ nm}$  is a good tool to trap the atoms leaving the Zeeman slower, and to cool the atoms to a certain limit. However, the temperatures required as a pre-requisite to load our optical lattice are around two orders of magnitude lower than what is obtained using the  $^1S_0\text{-}^1P_1$  transition.

Therefore, the post-cooling stage serves afterwards to cool the atoms down to below  $30 \mu\text{K}$  using the narrow  $^1S_0\text{-}^3P_1$  transition at  $556 \text{ nm}$ . The process of loading the green MOT from the blue MOT is described in section 5.3. After trapping the atoms in the green MOT, the light power and the detuning are ramped down to achieve minimum temperatures. The best ramping time was measured to be around  $45 \text{ ms}$ . It is in our interest to ramp down as fast as possible to keep the cycle short. However, shorter ramping times led to a remarkable loss of atoms inside the MOT. The trapped atoms are held after the ramping process in the MOT for around  $20 \text{ ms}$ . During this phase, the atoms are exposed to only  $5\%$  of the initial laser power and with a reduced detuning of  $1 \text{ MHz}$ . The relationship of the atom temperature with the laser power is shown in the bottom plot of figure 5.6. At full laser power of  $4 \text{ mW}$ , the atoms were heated up to temperatures around  $70 \mu\text{K}$ . This is higher than what is required to trap the atoms in our  $50 \mu\text{K}$  deep optical trap. The temperature of the atomic cloud drops down steadily with decreasing laser power to around  $20 \mu\text{K}$ , which is close to the Doppler limit, when using less than  $10\%$  of the initial power (see section 4.1). Reducing the value of the laser power to below  $5\%$  leads to a strong loss of atoms from the MOT.

### 5.3.1 The Optical Lattice

The optical resonator setup together with the laser system that are used to form the 1-D optical lattice are described in section 4.5. In this section, the experimental results related to the loading and trapping of atoms in the optical lattice will be shown. The number of atoms trapped in the optical lattice and its stability, as well as the lifetime, have a direct influence on the quality of the spectroscopy measurements on the clock transition. The optimization of those three values, together with the experimental limitations, will be discussed here.

For loading the optical lattice, it is crucial that the green MOT in its final phase is well overlapped with the position of the lattice, before the green laser is blocked (see figure 5.1). The first step is finding the position of the optical lattice inside the vacuum chamber. Since the optical lattice in our setup is fixed in position (see section 4.5), the green MOT has to be alligned to bring the atoms at the position of the lattice and to increase the loading efficiency. This is done by adjusting the magnetic fields in the horizontal and vertical planes. As it is shown in figure 5.7, three magnetic coils are used for the alignment. The coils Bh1 and Bh2 re-position the green MOT in the  $xz$  (horizontal) plane. The vertical allignement of the green MOT in the  $xy$  plane is done using the Bv1 coil. The overlapping of the green MOT

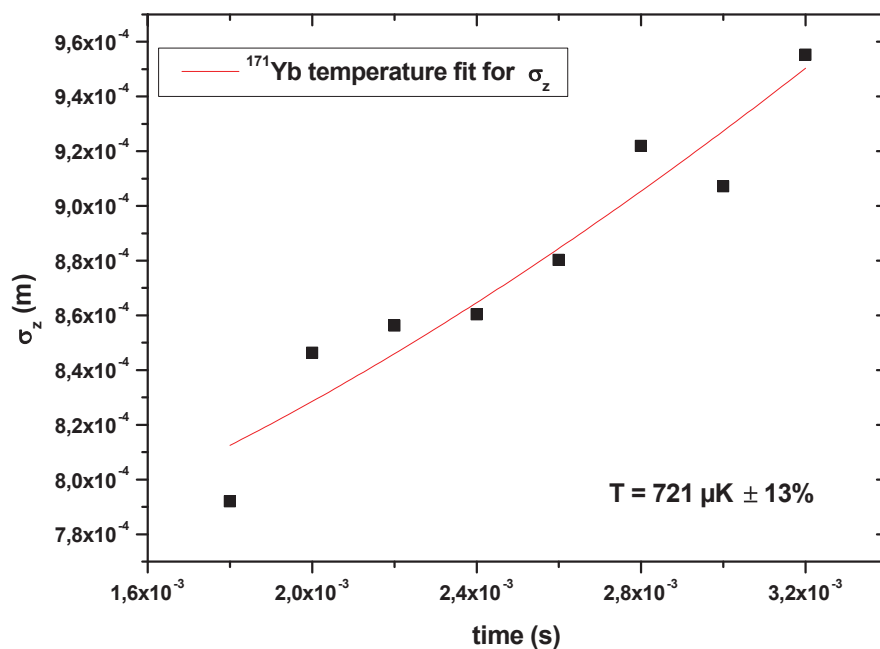
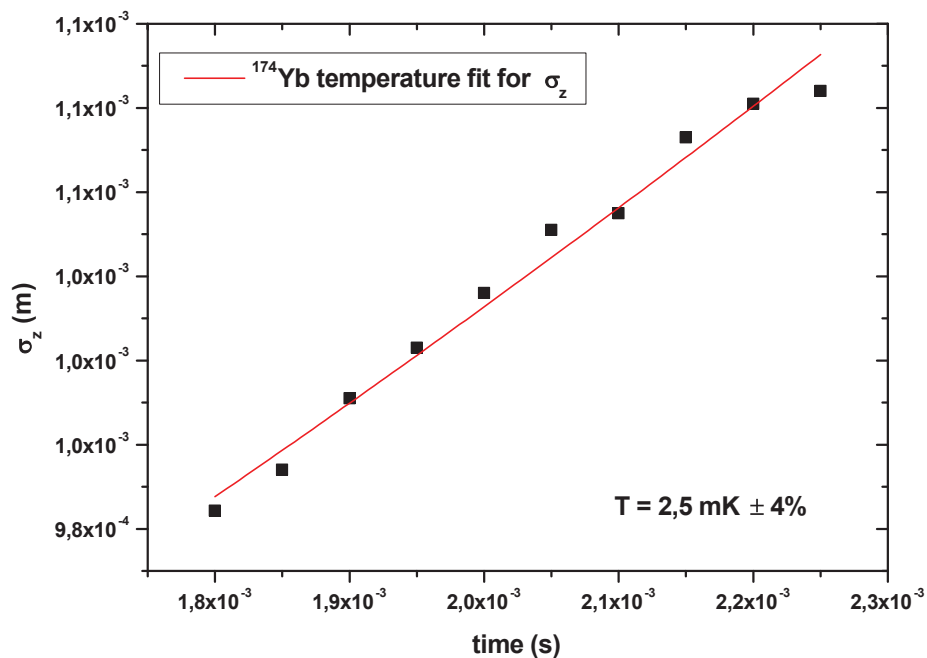


**FIGURE 5.5:** Temperature measurements of the fermionic isotope  $^{171}\text{Yb}$  and the bosonic isotope  $^{174}\text{Yb}$  in the blue MOT, using the TOF method. The plots, and the respective fits marked in red, show the expansion of the atomic clouds along the z-axis as a function of time.

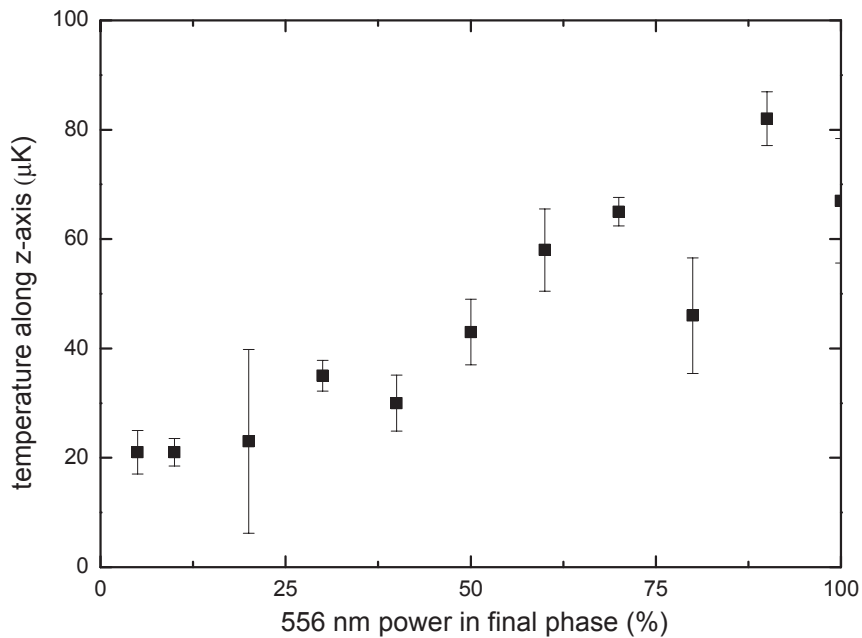
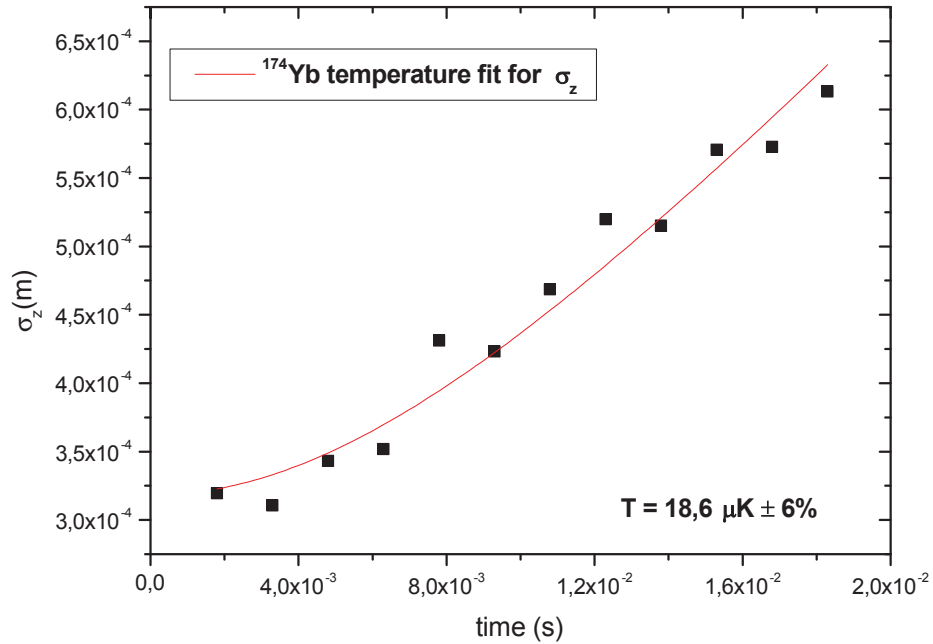


**FIGURE 5.6:** Top: Temperature measurement of the bosonic isotope  $^{174}\text{Yb}$  in the green MOT. The plot, and the corresponding fit in red, shows the expansion of the atomic cloud along the z-axis as a function of time. Bottom: A plot of temperature as a function of trapping light power for  $^{171}\text{Yb}$  in the green MOT. The experimental parameters for the isotope  $^{171}\text{Yb}$  were investigated in more details since the isotope was used for our spectroscopy measurement on the clock transition.

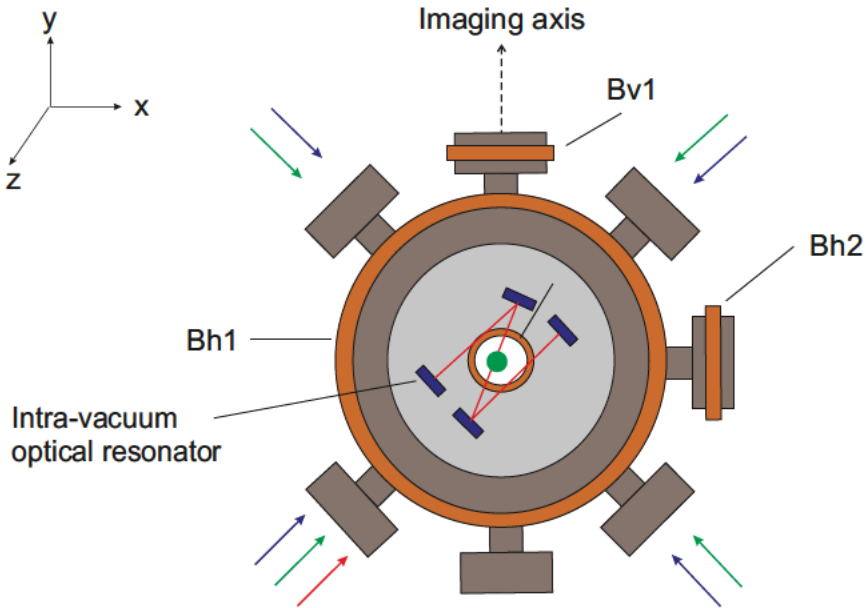


**FIGURE 5.7:** Simplified sketch of the main vacuum chamber. The relevant magnetic coils for adjusting the position of the green MOT are labeled as Bh1, Bh2 and Bv1. The magnetic field components of Bh1 and Bh2 are in the  $xz$  (horizontal) plane. Bv1 creates a magnetic field in the  $xy$  (vertical) plane.

with the lattice laser beam was done by changing the magnetic field of each coil at a time, while keeping the values of the other two constant. To check whether the green MOT is overlapped with the optical lattice, the MOT laser beams were switched off for a while before turning them on again. In case the MOT is not at the right position, no atoms are observed after 30 ms. When the green MOT is overlapped with the lattice beam, the atoms would get trapped inside the optical lattice for a longer time. Thus, the trapped atoms yield a non-vanishing fluorescence signal when the beams of the green MOT are switched on after 30 ms. The magnetic fields resulting from all three coils are then fixed at the values where the loading efficiency into the optical lattice is best. The loading efficiency appeared to be most sensitive to the magnetic field produced by Bh1. This is due to the inclination of the lattice laser beam at the trapping position. Figure 5.8 shows the dependency of the transfer efficiency, from the post-cooling stage into the optical lattice, on the position of the ultra-cold atoms. The change in the position of the MOT is induced by a change in the magnetic field produced by Bh1. Thus, the displacement of the atomic cloud is along the real radius of the red laser gaussian beam. The electrical current responsible for this change in the magnetic field was tuned between 17 and 17.5A. The normalized atom number as a function of position was fit with a Gauss profile and the measurement yielded a FWHM of  $165\mu\text{m} \pm 6\%$ . This value is comparable to the diameter of the atomic cloud at the time of loading into the optical lattice and to the lattice-beam-radius at the trapping position; calculated to be  $155\mu\text{m}$  [1]. Thus, the size of the atomic cloud after the compression phase in the post-cooling stage is

one of the main issues limiting the increase in the transfer efficiency.

The bottom plot in figure 5.8 shows the dependence of the transfer efficiency in the optical lattice on another important parameter, namely the temperature of the atomic cloud just before loading the optical lattice. The measurement was done by measuring the transfer efficiency for different powers of the green laser at the final stage of the green MOT (see section 5.3). The measurement was taken for three different values of the lattice potential depth. The maximum transfer efficiency from the green MOT into the optical lattice was measured to be around 25%. This is limited by the available laser power inside the resonator. Due to incoupling imperfections, a coupling efficiency higher than 10% into the intra-vacuum resonator was not possible [1]. The result is a potential depth of approximately  $50 \mu\text{K}$  (see section 6.3), which is comparable to the temperature of the atomic cloud in the final phase of the green MOT.

### The lifetime of atoms inside the optical lattice

The advantage of trapping the atoms in the optical lattice is the long access we gain to ultracold atoms after switching the MOT fields off. Taking our vacuum pressure into consideration, a lifetime of approximately 600 ms was expected for trapped atoms inside the lattice (see section 4.2). However, the experimental measurements showed a lifetime much shorter than that expected due to the background gas collisions. One reason behind the short lifetime may be the heating factor resulting from collisions with hot atoms and/or from near-resonant stray light. These two effects were investigated in an attempt to improve the lifetime of atoms in the optical lattice.

The trapped ultracold atoms are located along the path of the atomic beam coming from the atomic oven on the other side of the slower (see figure 4.2). Thus, collisions of the atoms coming from the atomic oven with the trapped atoms are probable and may be the reason behind the short lifetime. In order to investigate that, we ran the experiment at different oven temperatures. The values for the lifetime were taken for oven temperatures between  $340^\circ\text{C}$  and  $475^\circ\text{C}$ . As the top plot in figure 5.9 shows, no relevant improvement in the lifetime has been observed for lower oven temperatures. This rules out the possible role that the collisions of the atomic beam with the ultracold trapped atoms could have played, in reducing the lifetime of trapped atoms inside the optical lattice.

Another factor that may play a role in heating the trapped atoms is the near-resonance stray light. The detuned MOT laser beam at  $556 \text{ nm}$  is switched off using an AOM (see figure 4.5). Stray light can however still make its way to the vacuum chamber and heat the trapped atoms in the optical lattice. In order to avoid that, we placed a mechanical shutter after the AOM to block the residual near-resonant light. The bottom plot in figure 5.9 shows that the shutter has a positive affect on the lifetime. The increase in the lifetime for measurements done using the mechanical shutter is around 20 ms. This is already a relevant improvement, but the lifetime is

still below the limit induced by the background gas collisions.

Apart from the relatively short lifetime of atoms inside the lattice, large fluctuations were present in the atom number. The measurements done on the trapped atoms inside the optical lattice showed some discrepancy with the expected values. While the lattice potential depth was calculated to be  $200 \mu\text{K}$ , the experimental measurements indicate a value of approximately  $50 \mu\text{K}$  (see section 6.3). This factor, together with the comparable radii of the atomic cloud in the post-cooling stage and the trapping gaussian beam, may be the main reasons behind the big shot-to-shot fluctuations in the atom number, that limited the quality of the spectroscopy measurements. Moreover, despite the measures taken to increase the lifetime of atoms inside the optical lattice, the improved values are still about an order of magnitude lower than expected, if the collisions with the background gas are considered as the limitation. Thus, the reason behind the heating mechanism is still to be further studied. One possibility could be the intensity noise of the trapping laser [1] [86]. A higher vacuum pressure at the position of the lattice, due to outgassing of the glue used for the resonator, is also something that may be limiting the lifetime of trapped atoms inside the optical lattice.

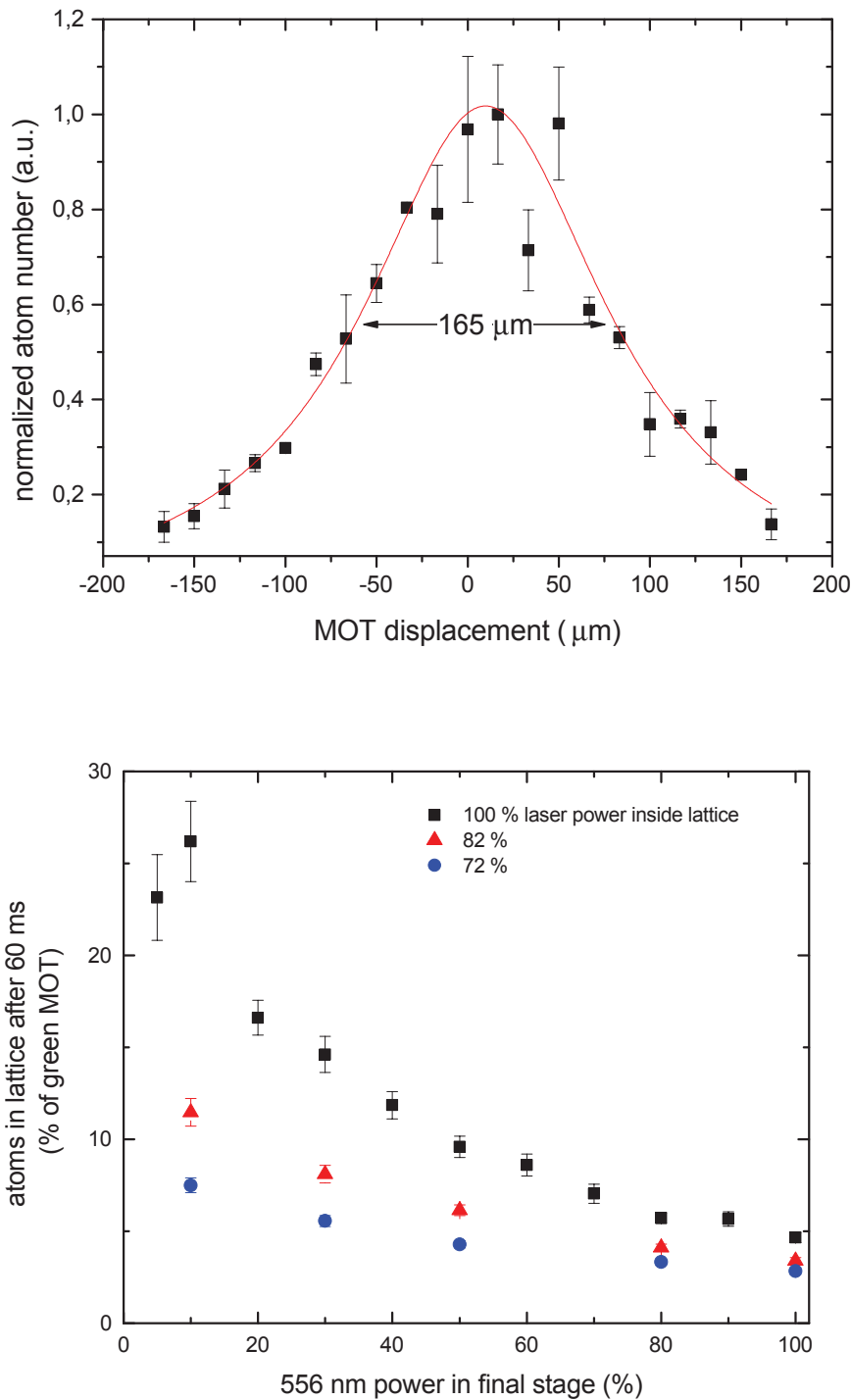


**FIGURE 5.8:** Loading efficiency in the 1-D optical lattice for  $^{171}\text{Yb}$ . Top: Normalized atom number transferred from the MOT into the optical lattice as a function of position of the MOT, relative to the assumed light-field maximum of the optical lattice. Bottom: Transfer efficiency of atoms into the optical lattice as a function of the green laser power in the final stage. Different curves have been taken for different lattice potential depths.

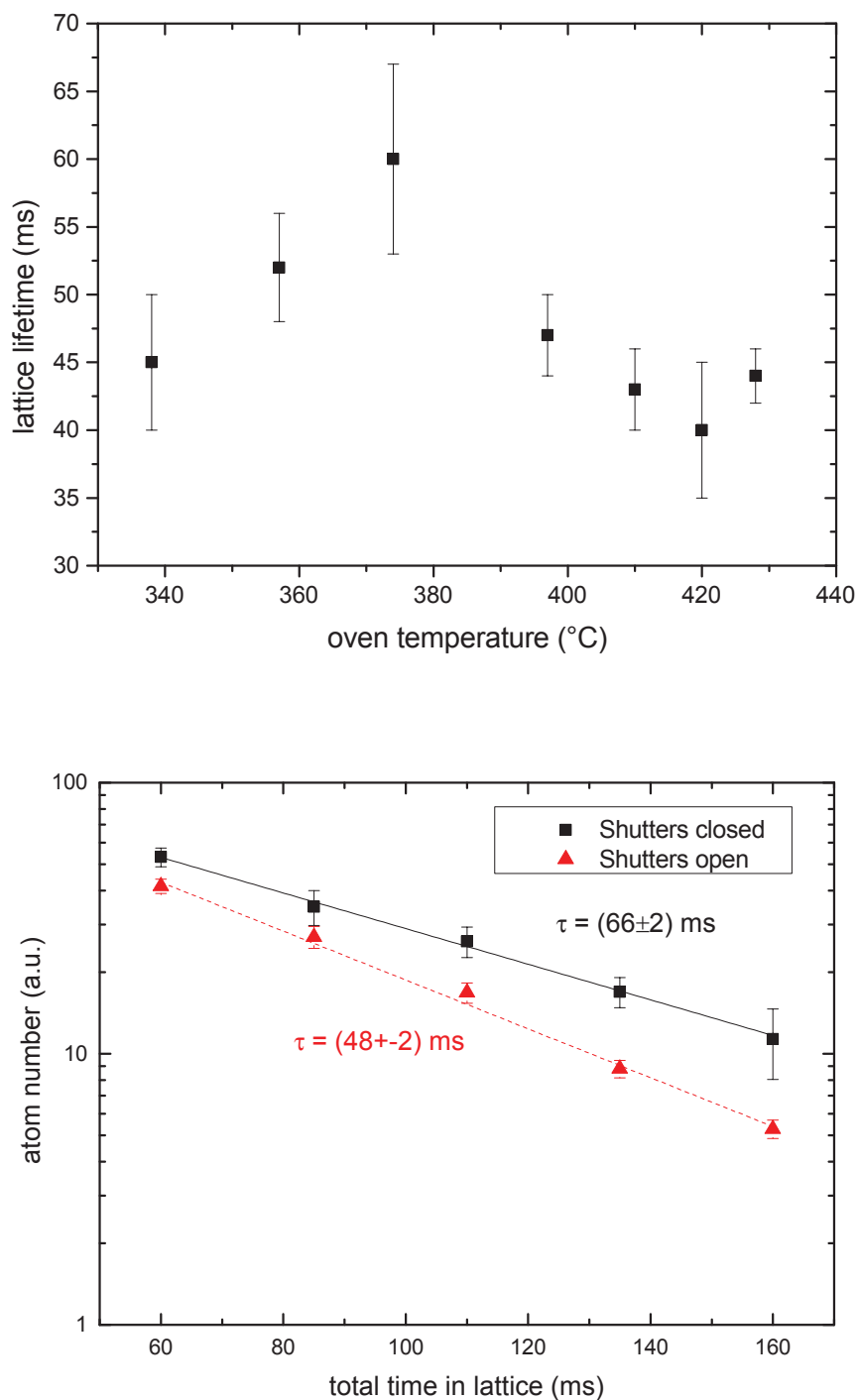


**FIGURE 5.9:** Lifetime of ultracold  $^{171}\text{Yb}$  in the 1-D optical lattice. Top: Relationship between the lifetime of atoms inside the optical lattice and the atomic oven temperature. Bottom: Lifetime of atoms in the optical lattice. The red plot shows the lifetime when the green light is switched off using an AOM, whereas the black plot shows an improved lifetime after the stray light was blocked by mounting a mechanical shutter after the AOM. The measurement was done at an oven temperature of  $375^\circ\text{C}$ .



# Chapter 6

## Spectroscopy on $^1S_0$ - $^3P_0$ Transition in $^{171}\text{Yb}$

In the context of this thesis, the first spectroscopy measurements on the  $^1S_0$ - $^3P_0$  clock transition in  $^{171}\text{Yb}$  was realized using the compact setup. The spectroscopy measurement was done in the scope of Tobias Franzen's masters thesis [1]. The transition was first localized by probing the freely expanding atomic cloud. More precise measurements on trapped atoms followed, yielding a narrower spectroscopy line. This chapter will show the spectroscopic results together with a sketch of the experimental sequence.

### 6.1 The Experimental Sequence

The different phases in which the atoms were slowed down, cooled, and trapped have been discussed in the previous chapters. The parameters in each, and for every, stage are put together in figure 6.1. The broad transition  $^1S_0$ - $^1P_1$  is used to slow the atoms in the Zeeman slower, as well as serving for pre-cooling the atoms down to 1 mK. During this stage the blue laser used for the MOT is red detuned by 20 MHz and the magnetic fields are on.

The atoms are then transferred into the green MOT and cooled down using the narrow  $^1S_0$ - $^3P_1$  transition (see section 5.3). A transfer efficiency of 6% is reached by exposing the atoms to 4 mW of red detuned laser power at 556 nm. Two processes follow afterwards. The first is ramping down the laser power and the detuning to minimize the recoil energy of the atoms together with the MOT diameter. As a result, the size of the atomic cloud and its temperature is reduced. Afterwards, the atoms are held in this experimental state for 20 ms to reach a minimal temperature.

After the ultracold atoms are prepared in the post-cooling stage, atoms are loaded in the optical lattice and spectroscopy is done on the  $^1S_0$ - $^3P_0$  clock transition. The imaging method that was used is the electron-shelving technique [87]. It is a very efficient way to observe weak transitions, in our case the  $^1S_0$ - $^3P_0$  clock transition. The idea behind it is to measure the number of atoms in the ground state, with

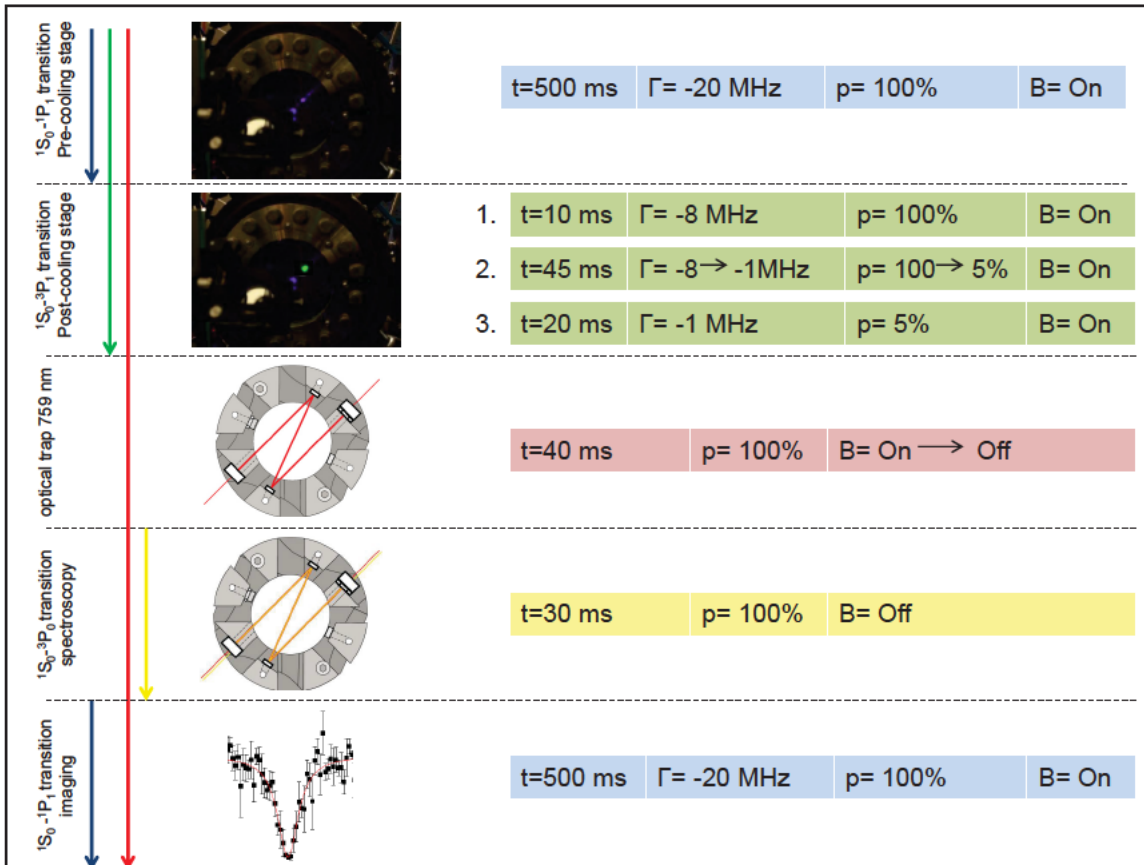


**FIGURE 6.1:** Sketch showing the experimental sequence, starting with the slowing of atoms and ending with the spectroscopy on the  $^1S_0$ - $^3P_0$  transition. The blue, green, red and yellow arrows on the left represent the laser to which the atoms are exposed at the given stage. The time span of each phase together with the laser detuning, laser power and the magnetic fields during that phase are shown on the right, respectively.

and without an excitation pulse. This was done by taking fluorescence images of the strong  $^1S_0$ - $^1P_1$  transition [58]. The depletion in the fluorescence signal signifies the number of atoms that was lost from the ground state after being excited to the long living state  $^3P_0$ .

The spectroscopy line of the clock transition was not directly observed using trapped atoms in the optical lattice. It was done step-by-step starting with spectroscopy on untrapped atoms using the chopped-MOT technique, followed by the chopped-lattice method, before the spectroscopy on trapped atoms inside the optical lattice was done. The different methods and the respective results will be discussed in the following sections.

## 6.2 Spectroscopy on Untrapped Atoms

In the frame of this work, the spectroscopy on the  $^1S_0$ - $^3P_0$  clock transition was done for the first time using our setup. Clock measurements have already been done by other groups using fermionic and bosonic Yb isotopes (see section 2.2) [40] [15] [16] [41] [42]. Our first attempts to detect the clock transition by probing atoms inside the optical lattice failed. Therefore, we made a step-back and probed the atoms in the post-cooling stage for the doppler broadened clock transition [58]. We refer to this method as the chopped-MOT technique.

As the name suggests, the chopped-MOT technique is based on releasing and recapturing the atoms in a MOT. In our case, the green MOT is used. Atoms in the green MOT are about 2 orders of magnitude colder than those trapped in the blue MOT. This results in less broadening of the clock transition due to the Doppler effect. The atoms are first cooled inside the MOT as described in the previous chapter. But instead of loading the atoms in the optical lattice as mentioned in figure 6.1, the MOT laser beams are switched off and the atoms are exposed to the probing laser for a short time before the MOT is switched on again (see figure 6.2). With the 578.4 nm laser having 500  $\mu$ W of power focused to a diameter of 200  $\mu$ m at the position of the atomic cloud, the calculated Rabi frequency is 3 kHz. This implies that only a small portion of atoms could be excited in one pulse, taking into consideration the Doppler broadening on the order of 100 kHz. Therefore, this sequence is repeated periodically for hundreds of times to excite a large number of atoms. After exposing the expanding atomic cloud to the probing clock-laser, the MOT light fields are turned on again to trap the atoms that are still in the ground state. This re-initializes the velocity-distribution curve of the atomic cloud. The atoms that get excited to the  $^3P_0$  state leave the MOT trapping region due to gravity. Therefore, the excited atoms go out-of-resonance with the near-vertical probe laser beam due to the Doppler effect. Otherwise, the following pulse at 578 nm could lead to the transfer of atoms from the excited state to the ground state through stimulated emission.

The spectroscopy line shown in figure 6.3 was taken by switching the probe laser

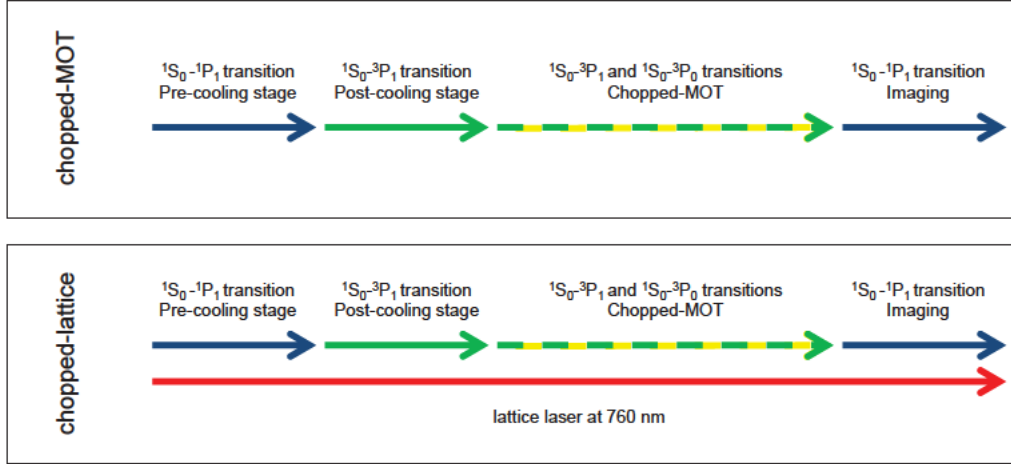


**FIGURE 6.2:** Sketch showing the experimental sequence for the chopped-MOT and the chopped-lattice techniques.

beam on every  $500 \mu\text{s}$  for 300 repetitions. The atoms that stay in the ground state are detected afterwards. For these experimental values, the maximum reduction of the atom number is 70%. The resulting Doppler broadened linewidth is 300 kHz, as it is shown in figure 6.3. The corresponding atomic temperature to the Doppler broadened line was calculated to be  $140 \mu\text{K}$ . This value is higher than what was expected compared to the lowest temperatures that were measured previously in the green MOT. However, the strong dependency of the temperature on the green laser power and frequency was demonstrated in the previous chapter. In this case, the MOT was not optimized for the minimum temperature but for the best position at the location of the 578.4 nm laser.

Concerning the central frequency, it is blue shifted by  $7.5 \text{ kHz} \pm 11\%$  due to the Doppler and the recoil shifts, that arise mainly from our experimental geometry. The alignment of the probing clock laser along the path of the lattice beam leads to a near-vertical probing of the atoms. In the case of untrapped atoms, the central frequency is shifted due to the non-vanishing velocity along the gravitational axis, resulting in a frequency shift [88]

$$\Delta\nu = \nu_0 \left( \frac{v + v'}{2c} \right) \quad (6.1)$$

Here, the recoil shift is included in the expression for Doppler shift. The atomic velocity before absorbing a photon and after the absorption is expressed as  $v$  and  $v'$ , respectively. Other sources of error may also influence the frequency, such as the residual near-resonance green light during the probing phase. For the chopped-MOT method, the MOT light was switched off using the AOM only. The mechanical shutter was not used due to its slow response. As it was shown in section 5.3.1, the lifetime of atoms trapped inside the lattice was increased by using the mechanical

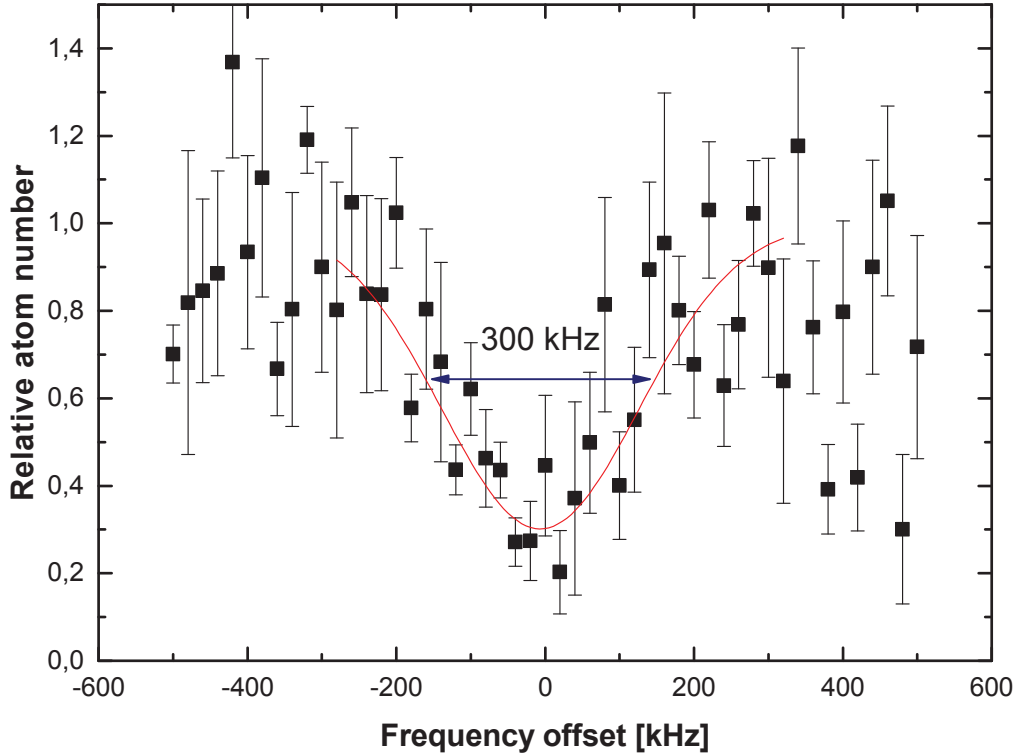


**FIGURE 6.3:** Spectroscopy on the  $^1S_0$ - $^3P_0$  transition for  $^{171}\text{Yb}$  in a chopped-MOT. The Doppler effect due to the motion of the freely expanding cloud results in a broad linewidth. The FWHM was measured to be approximately 300 kHz.

shutter. Thus, the influence of residual near-resonance green light has already been observed and may act as a source of error in this case.

### 6.3 Spectroscopy on Atoms Trapped in the Optical Lattice

The process of probing the clock transition for trapped atoms inside the optical lattice was done using two different methods. In the first method, the lattice light was switched on while the chopped-MOT sequence was running. We refer to this method by using the term chopped-lattice. Later on, spectroscopy was done on atoms trapped for an extended period of time in the optical lattice.

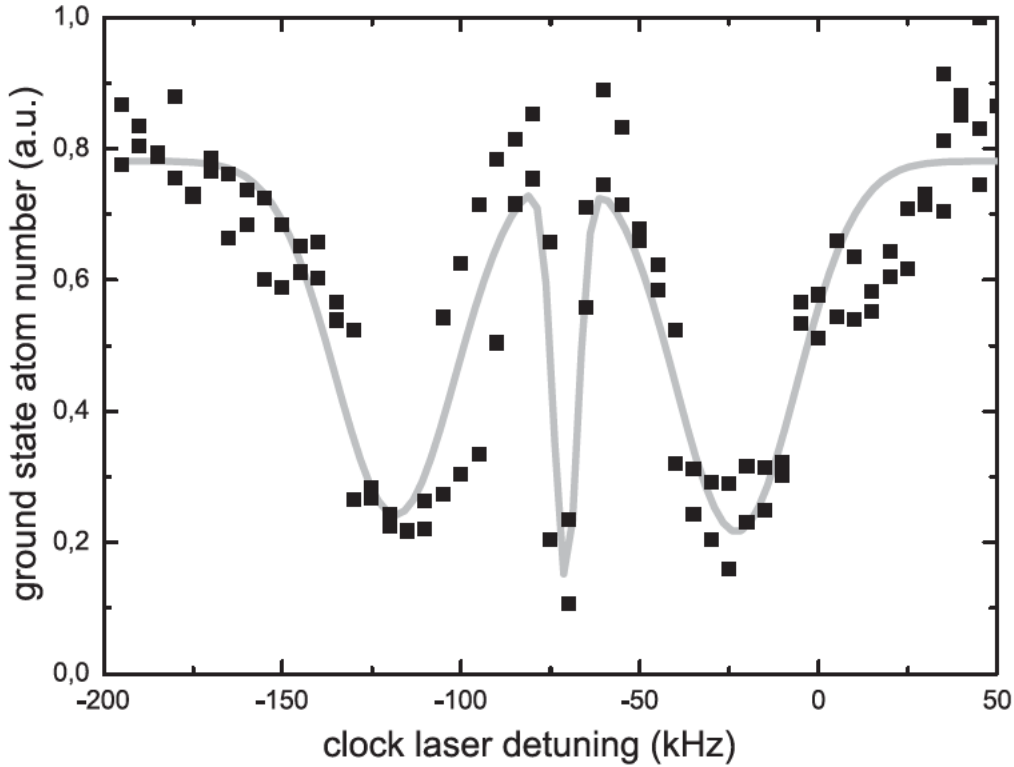


**FIGURE 6.4:** Spectroscopy on the  $^1S_0$ - $^3P_0$  transition in  $^{171}\text{Yb}$  using the chopped-lattice method. Throughout this measurement, the optical lattice was switched on. The linewidth is 2 orders of magnitude smaller than what was measured using the chopped-MOT method [89].

### 6.3.1 Spectroscopy in a Chopped-Lattice

The first attempt to probe the  $^{171}\text{Yb}$  atoms inside the optical lattice was by switching the 760 nm laser on, while operating the experiment in a similar way as it was done for the chopped-MOT method (see figure 6.2). This is an intermediate stage between untrapped atoms and trapped atoms in the optical lattice. The measurement taken here allows us to see the effect of the lattice on the Doppler broadened spectroscopy line, by trapping the atoms for a short time in the lattice during a chopped-MOT measurement. Thus, we refer to this method as "chopped-lattice". Since the 578 nm and the 760 nm laser beams are overlapped inside the resonator, no additional adjustments have to be done on the position of the atomic cloud. The overlapping of the light beams was done by aligning the clock-laser light at 578 nm with the lattice light at 760 nm. Both beams were guided over a long distance before and after the vacuum chamber to insure good alignment. The retro-reflecting mirror used for the intra-vacuum resonator has a minimal reflection for the 578 nm wavelength (<1%), thus transmitting the yellow laser beam finally outside the resonator (see section 4.5).

A spectroscopy line that was taken with the chopped-lattice method is shown in figure 6.4. Since a portion of the probed atoms is trapped in the optical lattice, the probability to induce stimulated emission of atoms in the  $^3P_0$  excited state back

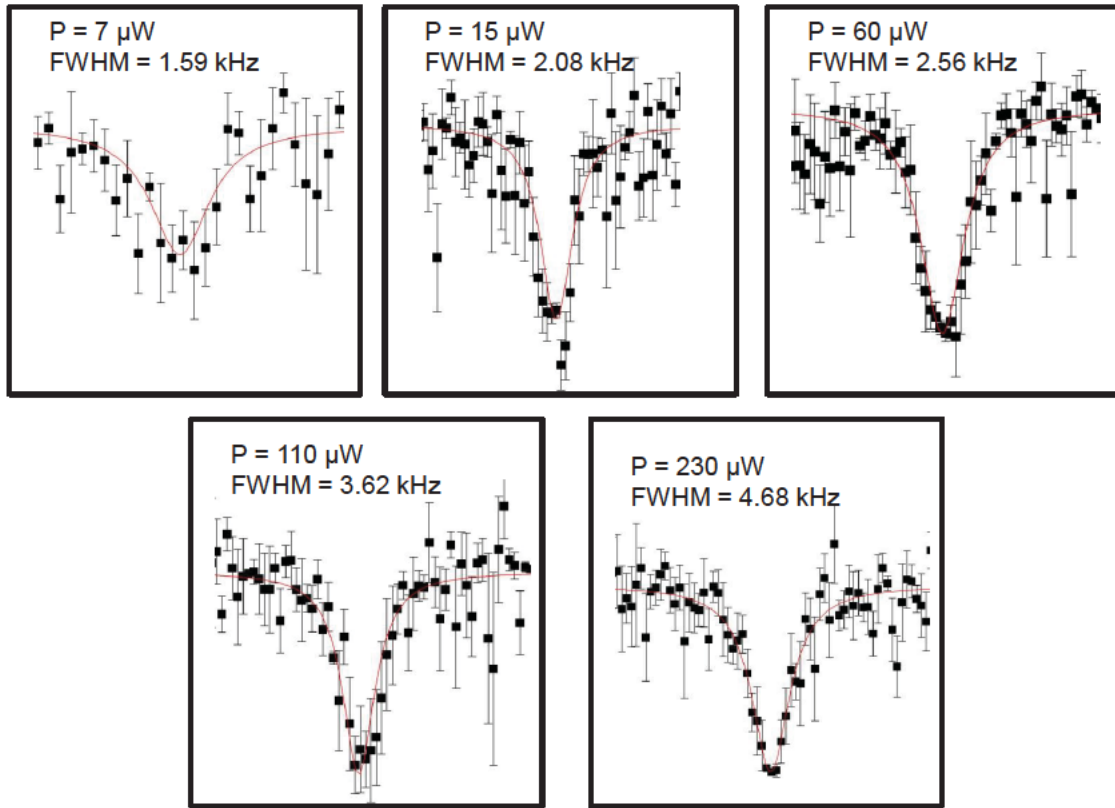


**FIGURE 6.5:** The carrier peak of the clock transition for atoms inside the optical lattice, measured using the "chopped-lattice" method for different probe laser power.

into the  $^1S_0$  state is higher than that for untrapped atoms, in which excited atoms are driven out of the trapping region by the force of gravity. Therefore, a smaller amplitude of the spectroscopy signal (i.e. a small reduction of the atom number) is expected here.

By trapping the atoms in the Lamb-Dicke regime, spectroscopy on the clock transition yields a profile with three components, namely the carrier peak and two sidebands [90]. The carrier peak is a result of the excitation of atoms from the  $^1S_0$  state to the  $^3P_0$  state, with motional states  $n=n'$  (see figure 6.7). On the other hand, transitions between different motional states result in 2 additional peaks, one is blue-detuned ( $n < n'$ ) and the other is red-detuned ( $n > n'$ ) with respect to the carrier. The measurement in figure 6.4 shows a 3 kHz broad carrier in addition to the blue and red sidebands. The two orders of magnitude narrower linewidth than that obtained by the chopped-MOT method is due to the suppression of the doppler broadening for the carrier peak. The independent nature of the carrier transition from  $n$ , makes it minimally sensitive to the temperature of trapped atoms, which is not the case for the sidebands. The ratio of the blue and red sideband amplitudes reveal in principal

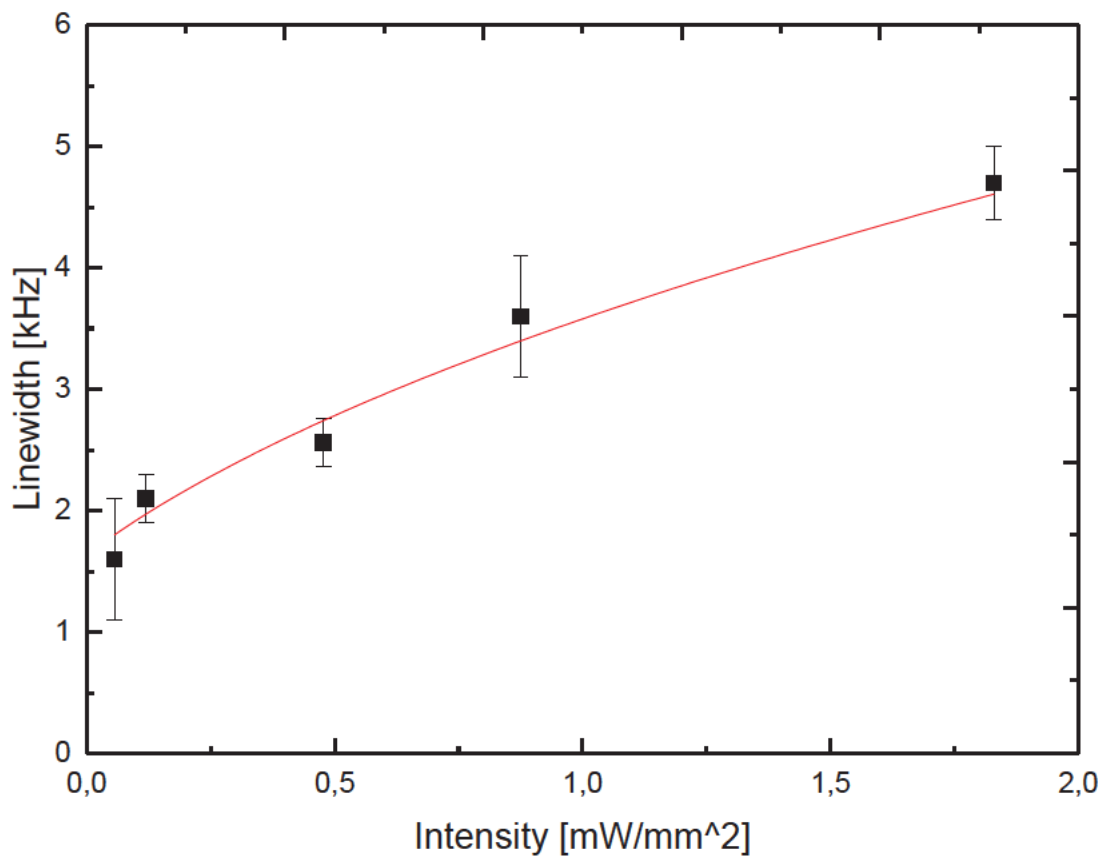
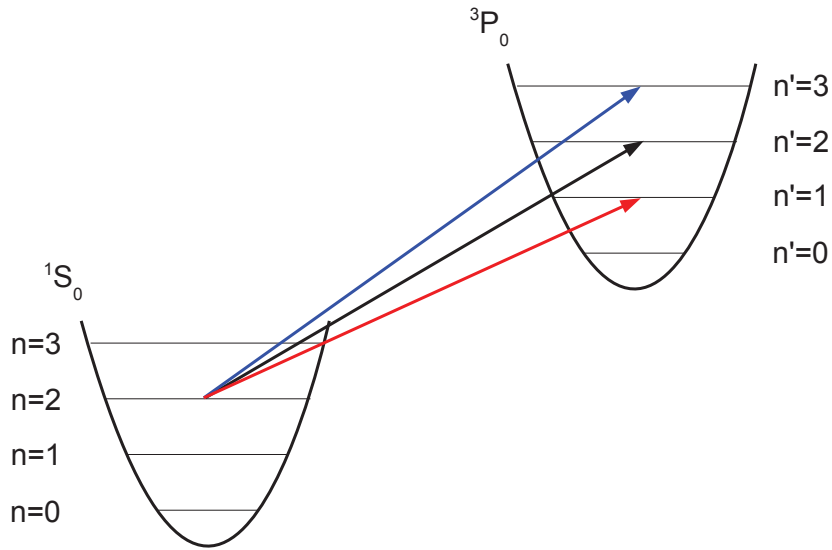


FIGURE 6.6: FWHM of the carrier peaks are plotted and show the increase in the linewidth for increasing laser power.



**FIGURE 6.7:** Transitions between different motional states of a trapped atom in the Lamb-Dicke regime. The atom is excited from the  $^1S_0$  ground state to the  $^3P_0$  excited state.

the thermal distribution of atoms inside the lattice. Unfortunately, the low signal to noise ratio doesn't allow us to obtain an exact temperature from the sideband amplitudes. However, the close amplitudes of both peaks indicate a temperature on the order of hundreds of  $\mu\text{K}$ . Moreover, by measuring the distance between the blue sideband and the carrier, the vibrational frequency of the atoms inside the lattice can be obtained. In addition to that, the width of the sideband is related to the anharmonicity of the lattice potential. From the measurement shown here, the vibrational frequency was found to be approximately 50 kHz. The 100 kHz separation between both sidebands indicates a lattice depth of approximately 50  $\mu\text{K}$ , which is about one fourth of what was expected.

In an attempt to study the reasons behind the linewidth broadening of the carrier peak beyond the Fourier limit, the effects of the saturation broadening and the magnetic shift were examined. The linewidth broadening due to the short pulses (500  $\mu\text{s}$  pulse length) is calculated to be 1 kHz, which is one third of the total broadening. The method shown here still employs the chopped-lattice technique. Thus, for the measurements done at this stage, the probed atoms were still exposed to the magnetic field gradient for the MOT. Considering our magnetic field gradient of 40 G/cm, the trapped atoms along a length of 200  $\mu\text{m}$  perceive a maximum magnetic field difference of 0.8 G. This corresponds to a contribution of the first order Zeeman shift to the total line broadening of 1 kHz (see section 2.5).

The third effect is saturation broadening. When probing the atoms with relatively

high intensities, the pumping rate becomes higher than the relaxation rate leading to a line broadening of the atomic transition, which is proportional to the ratio of the laser intensity to the saturation intensity of the transition [25]. The relation between the linewidth and the intensity of the probing laser was examined by taking spectroscopy measurements of the carrier peak for different laser intensities. The plots shown in figure 6.5 demonstrate this relationship for laser powers between  $7 \mu\text{W}$  and  $230 \mu\text{W}$ , which correspond to calculated peak intensities between  $0.06 \text{ mW/mm}^2$  and  $1.9 \text{ mW/mm}^2$ . The corresponding linewidths related to the minimum and the maximum intensities were measured to differ by several kHz, as shown in figure 6.6. At low intensities, the fit indicates a residual linewidth of approximately 1.5 kHz.

While the observed broadening may be explained by the Fourier-, Zeeman- and saturation-broadening, other residual broadening effects may also have contributed to the total broadening of the carrier linewidth. Those factors have still to be checked and controlled appropriately. This includes a possible deviation of the lattice wavelength from the magic wavelength [13], and the residual magnetic field at the position of the probed atoms.

### 6.3.2 Spectroscopy in the Optical Lattice

As already mentioned previously in this chapter, the main purpose of the spectroscopy measurements using the chopped-MOT method is to obtain a rough value for the transition frequency. After this was achieved, the experimental sequence described in figure 6.1 was applied for direct spectroscopy on atoms trapped in the optical lattice. After the ultracold atoms are prepared in the green MOT, the green laser is switched off by an AOM and the residual light is blocked by a shutter. Thus, the atoms are fully trapped in the optical lattice. At this stage, the atoms are only exposed to the lattice light source at 759 nm. The magnetic fields are ramped down as the last step before doing spectroscopy on the  $^1S_0$ - $^3P_0$  clock transition. The yellow light at 578 nm is then switched on for 30 ms. The detection is done by using the electron-shelving technique. The number of atoms that are still in the  $^1S_0$  ground state is detected after exposing the atoms to the probe laser, thus giving the number of atoms that was transferred to the  $^3P_0$  excited state. This is achieved by setting the experimental parameters back to the blue MOT phase (see figure 6.1), exciting the strong  $^1S_0$ - $^1P_1$  transition and measuring the number of atoms that is captured in the blue MOT.

The spectroscopy measurement done on the clock transition for atoms trapped in the optical lattice can be seen in figure 6.9. Due to the single laser pulse per experimental loop and the random spin of trapped atoms, only 25% of the initial population can be excited to the  $^3P_0$  state. A maximum excitation probability of 50% would have been possible in the case of spin polarized atoms. All four Zeeman sub-states appear in this spectroscopic measurement even though no intentional constant magnetic field was applied. The coils responsible for creating the MOT quadrupole field were turned off during the probing time. The four peaks are due to a constant magnetic field inter-

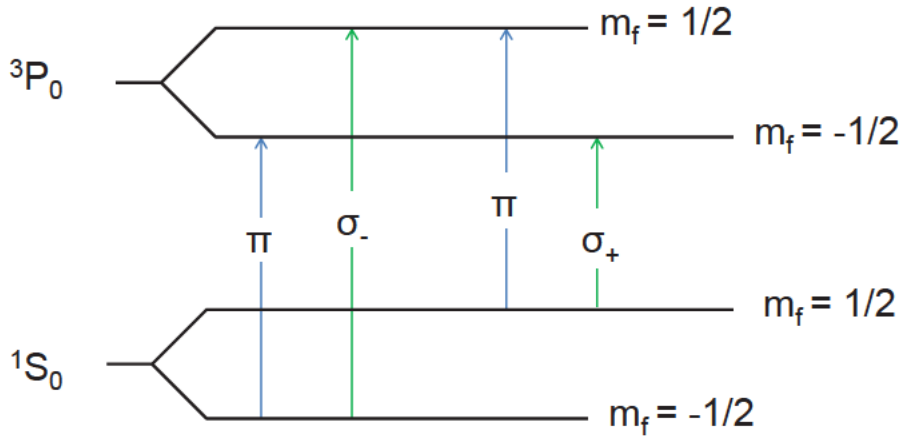


**FIGURE 6.8:** Transitions between the  $m_f = 1/2, -1/2$  substates of the  $^1S_0$  and  $^3P_0$  states.

acting with the ground state and the excited state. What we see are the transitions between the  $m_f = 1/2, -1/2$  substates of the  $^1S_0$  and  $^3P_0$  states. The strength of the constant magnetic field can be obtained from the splitting of the Zeeman sub-states. The shift coefficients were calculated to be  $\pm 940$  Hz/G and  $\pm 200$  Hz/G for the  $\sigma_{\pm}$  and the  $\pi$  transitions, respectively [91]. Taking the measurement in figure 6.9 into account, the magnetic field obtained from the  $\sigma_{\pm}$  and the  $\pi$  transitions appear to be inconsistent by a factor of 2. The value of the magnetic field obtained from the  $\sigma_{\pm}$  transitions is 1.7 G. Therefore, the peaks of the  $\pi$  transitions are expected to have a separation of 650 Hz instead of 1.3 kHz, as marked by the dashed lines in figure 6.9. The linewidth of the clock transition for measurements done on trapped atoms in the optical lattice is significantly smaller than that measured in a chopped-lattice. A linewidth of approximately 200 Hz was measured when exposing the atoms to about  $5\text{mW}/\text{cm}^2$  of yellow light, which is still saturation-limited [1]. But the affect of the saturation broadening on the linewidth was not further investigated here, knowing that the linewidth is dominated by other residual effects that have to be controlled in the first line, such as the Zeeman effect and the deviation of the lattice laser from the magic-wavelength.

The various shifts that were discussed in section 2.5 have been mentioned and maybe observed in some measurements. However, no detailed investigation of the shifts has been done in the scope of this thesis. A rough estimation of the shifts has been sketched in the masters thesis of Tobias Franzen [1]. Moreover, recent experimental results for optical atomic clocks with neutral Yb as a reference have been discussed in chapter 2. But the aim of presenting the spectroscopy measurements in this work is mainly to demonstrate the experimental status of the Yb atomic source, which has been built during my thesis. A more thorough investigation of the clock

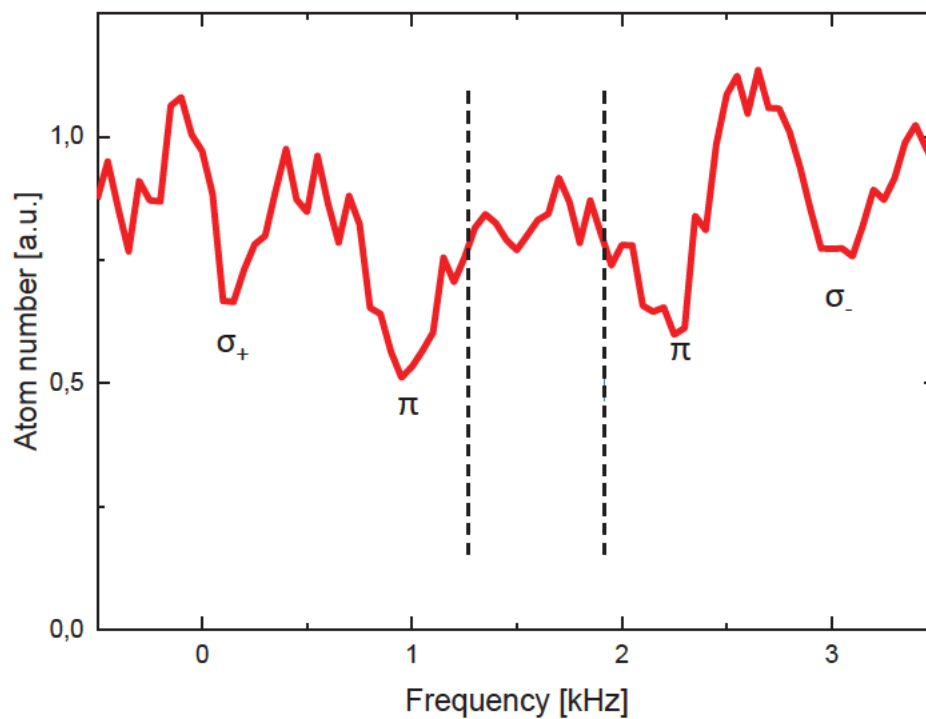


**FIGURE 6.9:** A spectroscopy measurement of the clock transition for  $^{171}\text{Yb}$ , trapped inside the optical lattice. The plot shows the four transitions for the possible Zeeman sub-states. The dashed black lines indicate the positions at which the  $\pi$  transitions are expected to be.

---

transition has been done by Gregor Mura [5]. An in-depth study of the systematic errors have still to be done for a better understanding of the experimental setup and for possible elimination of the broadening sources.



# Chapter 7

## Conclusion and Next Steps

In the frame of this thesis, a source of ultracold Yb atoms for a compact optical clock based on neutral Yb was built and characterized. The first spectroscopy measurements using this apparatus were also demonstrated. The optical and opto-mechanical setup of the ultracold source is fully contained on a  $2 \times 1 \text{ m}^2$  transportable table. The electronics for the experiment control are contained in two racks. The slowing and pre-cooling stages were done using the strong  $^1S_0$ - $^1P_1$  transition at 339 nm. The atoms were afterwards further cooled from a few mK to several tens of  $\mu\text{K}$  through the narrow  $^1S_0$ - $^3P_1$  transition at 556 nm. Finally, the atoms are loaded into the 1-D optical lattice, which gives us access to trapped atoms for around 65 ms. The clock transition was probed for atoms trapped inside the lattice, yielding a spectroscopy peak with a linewidth of 200 Hz.

The most time consuming tasks through-out this work were the attempts to improve the stability of the laser systems and to reduce the atom-number-fluctuations inside the post-cooling MOT and the optical lattice. The blue laser diode, which was chosen for its compactness, is extremely sensitive to temperature changes inside the laboratory. Thus, locking the laser on the right frequency for a longer time was a challenge, in particular during times when significant changes in the laboratory temperature were observed. In addition, the stabilization system for the green laser was far away from being perfect due to the very small spectroscopy signal we had. The spectroscopy's low signal-to-noise resulted in short-term fluctuations in the locking signal. The lack of stability in the laser systems may be one of the main reasons behind the fluctuations in the atom-number that had its clear fingerprints on our measurements. Whether the large fluctuations in the atom-number inside the optical lattice is mainly due to the instability of the MOT's laser systems or not, is something that we still don't know. After completion of the experimental work of this thesis, the blue as well as the green laser system have been replaced and a new spectroscopy setup has been built in the scope of the thesis of Gregor Mura [5] to improve the stability of the system.

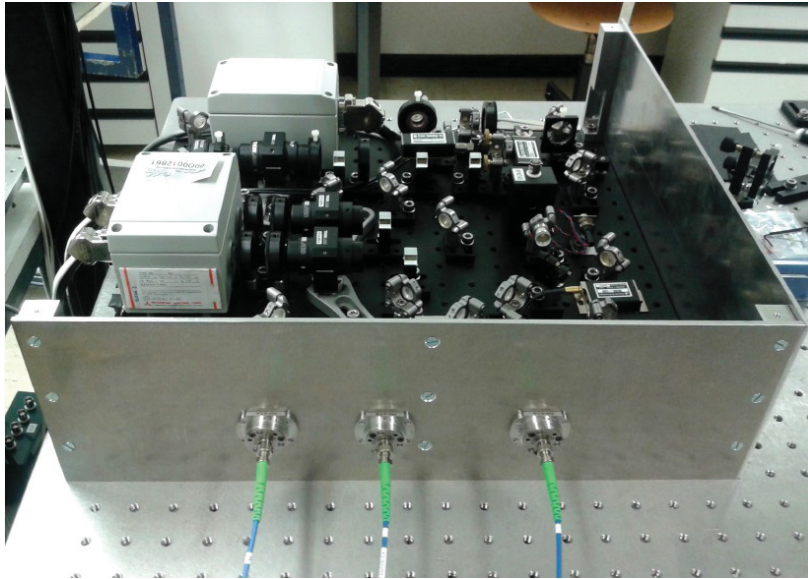


**FIGURE 7.1:** New 399 nm laser system. The whole system fits into a 19 inch, fiber-coupled, rack shelf [89].

### Next steps...

The results that have been shown in this work go back to the year 2013. For professional reasons, finalizing the thesis took me around two years after the experimental measurements have been taken. In the meanwhile, a lot of changes and modifications have been done to the experiment by my colleagues, in particular by Gregor Mura.

In the frame of Gregor Mura's Ph.D. thesis, the concentration was put on further development of the experiment by improving the existing setup and implementing new parts in the experiment to enhance the long-term, as well as the shot-to-shot stability of the experiment. Therefore, a new laser-setup at 399 nm was built (see figure 7.1). The new setup is contained in a box and blue light is out-coupled using optical fibers. This new construction is more compact than the old setup and is better isolated from the laboratory environment, which makes the diode lasers less sensitive to temperature fluctuations inside the laboratory. In addition to that, the source for the laser radiation for the green MOT was replaced by a new one from MenloSystems. The new laser has a higher output power and a better stability.

Moreover, a new fiber-based spectroscopy cell was designed and integrated in the experiment. This spectroscopy cell has several advantages over the one that was shown in this work. The new setup is not attached to the main vacuum chamber. Thus, the Yb oven for spectroscopy can be re-filled without having to open the main vacuum chamber. Moreover, the spectroscopy setup can be independently moved to the position where it is most convenient. But more importantly, the locking scheme of the green laser has changed with the implementation of the new setup. No direct

detection of green fluorescence is essential anymore. The blue and the green lasers are both locked by detecting the blue signal from the spectroscopy cell. By having both laser beams overlapped at the position of the atoms, the blue signal would drop when the green laser is at resonance with the atoms. This is due to the excitation of atoms to the long-living  $^3P_1$  state. This difference in the blue signal is then used to lock the green laser.

Recently, new spectroscopy measurements on the clock transition have been done. The transition have been observed with a linewidth that is one order of magnitude better than what was obtained using the old experimental setup. In addition to that, the signal-to-noise ratio has been improved by using a re-pumper at 1388 nm. The results will be demonstrated in Gregor Mura's Ph.D. thesis [5].

Several weeks ago, the experiment has been transported to INRIM - Turin, successfully demonstrating the transportability of the setup. The next big step is comparing our Yb optical clock with the Yb optical clock present at INRIM. A new characterization of the clock will help understand better the shifts on the clock transition and the respective uncertainties. A lot of work has been invested in building the clock and a lot is still to be done in terms of characterizing and optimizing the setup.



# Bibliography

- [1] Tobias Franzen. Spectroscopy of the Clock Transition in Ytterbium. Master's thesis, Heinrich-Heine-Universität Düsseldorf, 2012.
- [2] Charbel Abou Jaoudeh. A Magneto-Optical Trap for Atomic Ytterbium. Master's thesis, Heinrich-Heine-Universität Düsseldorf, 2008.
- [3] Y. Takasu, K. Komori, K. Honda, M. Kumakura, T. Yabuzaki, and Y. Takahashi. Photoassociation spectroscopy of laser-cooled ytterbium atoms. *Phys. Rev. Lett.*, 93:123202, 2003.
- [4] J. E. Golub, Y. S. Bai, and T. W. Mossberg. Radiative and dynamical properties of homogeneously prepared atomic samples. *Phys. Rev. A*, 37:119, 1988.
- [5] Gregor Mura. *Optimierung und Charakterisierung einer transportablen Optischen Gitteruhr mit Ytterbium*. PhD thesis, Heinrich-Heine-Universität Düsseldorf, 2015.
- [6] National Physical Laboratory. What is the most accurate measurement known? . [http://npl.co.uk/reference/faqs/what-is-the-most-accurate-measurement-known-\(faq-quantum\)](http://npl.co.uk/reference/faqs/what-is-the-most-accurate-measurement-known-(faq-quantum)), 2007 (accessed April 23, 2014).
- [7] F. G. Major. *The Quantum Beat*. Springer Science+Business Media, LLC, 2007.
- [8] National Institute of Science and Technology. A Revolution in Timekeeping . <http://nist.gov/pml/general/time/revol.cfm>, 2009 (accessed October 5, 2010).
- [9] T. P. Heavner, S. R. Jefferts, E. A. Donley, J. H. Shirley, and T. E. Parker. NIST-F1: recent improvements and accuracy evaluations. *Metrologia*, 2005.
- [10] S. Bize, P. Laurent, M. Abgrall, H. Marion, I. Maksimovic, L. Cacciapuoti, J. Gruenert, C. Vian, F. pereira dos Santos, P. Rosenbusch, P. Lemonde, G. Santarelli, P. Wolf, A. Clairion, A. Luiten, M. Tobar, and C. Salomon. Cold atom clocks and applications. *J. of Phys. B*, 38:S449, 2005.
- [11] D.W. Allan. Statistics of atomic frequency standards. *Proceedings of the IEEE*, 54:221, 1966.
- [12] R. J. Rafac, B. C. Young, J. A. Beall, W. M. Itano, D. J. Wineland, and J. C. Bergquist. Sub-dekahertz ultraviolet spectroscopy of  $^{199}\text{Hg}^+$ . *Phys. Rev. Lett.*, 85:2462, 2000.
- [13] Hidetoshi Katori, Masao Takamoto, V. G. Palchikov, and V. D. Ovsiannikov. Ultra-stable optical clock with neutral atoms in an engineered light shift trap. *Phys. Rev. Lett.*, 91:173005, 2003.

- 
- [14] C.W. Chou, D.B. Hume, J.C.J. Koelemeij, Wineland D.J., and T. Rosenband. Frequency comparison of two high-accuracy Al<sup>+</sup> optical clocks. *Phys. Rev. Lett.*, 104:070802, 2010.
- [15] N. D. Lemke, A. D. Ludlow, Z. W. Barber, T. M. Frontier, S. A. Diddams, Y. Jiand, S. R. Jefferts, T. P. Heavner, T. E. Parker, and C. W. Oates. Spin 1/2 optical lattice clock. *Phys. Rev. Lett.*, 103:063001, 2009.
- [16] N. Hinkley, J.A. Sherman, N.B. Phillips, M. Schioppo, N.D. Lemke, K. Beloy, M. Pizzocaro, and A.D. Ludlow. An atomic clock with  $10^{-18}$  instability. *Science* DOI:10.1126, 2013.
- [17] B.J. Bloom, T.L. Nicholson, J.R. Williams, S.L. Campbell, M. Bishof, X. Zhang, W. Zhang, S.L. Bromley, and J. Ye. An optical lattice clock with accuracy and stability at  $10^{-18}$  level. *Nature*, 506:71, 2014.
- [18] S. Schiller, G. Tino, S. Bize, U. Sterr, A. Görlitz, Ch. Lisdat, N. Poli, A. Nevsky, and C. Salomon. ELIPS3 - The Space Optical Clocks(SOC) Projet. Final Report, SOC Team, 2012.
- [19] Th. Udem, S. A. Diddams, K. R. Vogel, C. W. Oates, E. A. Curtis, W. D. Lee, W. M. Itano, R. E. Drullinger, J. C. Bergquist, and L. Hollberg. Absolute frequency measurements of the Hg<sup>+</sup> and Ca optical clock transitions with a femtosecond laser. *Phys. Rev. Lett.*, 86:4996, 2001.
- [20] S. A. Diddams, D. J Jones, J. Ye, S. T. Cundiff, J. L. Hall, J. K. Ranka, R. S. Windeler, R. Holzwarth, T. Udem, and T. W Haensch. Direct link between microwave and optical frequencies with a 300 THz femtosecond laser comb. *Phys. Rev. Lett.*, 84:5102, 2000.
- [21] T. W. Haensch and A. L. Schawlow. Cooling of gases by laser radiation. *Opt. Comm.*, 13:68, 1975.
- [22] R. Paschotta. Derivation of the Schawlow-Townes Linewidth of Lasers. Review, RP Photonics Consulting GmbH, 2010.
- [23] D. Leibbrandt, M. Thorpe, M. Notcutt, R. Drullinger, T. Rosenband, and J. Bergquist. Spherical reference cavities for frequency stabilization of lasers in non-laboratory environments. *Opt. Expr.*, 19:3471, 2011.
- [24] J. Millo, D. Magalhaes, C. Mandache, Y. Le Coq, E. English, P. Westergaard, J. Lodewyck, S. Bize, P. Lemonde, and G. Santarelli. Ultra-stable lasers based on vibration insensitive cavities. *Phys. Rev. A*, 79:053829, 2009.
- [25] A. Siegman. *Lasers*. University Science Books, 1986.
- [26] D. Leibbrandt, M. Thorpe, M. Notcutt, R. Drullinger, T. Rosenband, and C. Bergquist. Spherical reference cavities for frequency stabilization of lasers in non-laboratory environments. *Opt. Expr.*, 19:3471, 2011.
- [27] S. Webster and P. Gill. Force-insensitive optical cavity. *Opt. Lett.*, 36:3572, 2011.

- [28] T. Rosenband, D. B. Hume, P. O. Schmidt, C. W. Chou, A. Bruschi, L. Lorini, W. H. Oskay, R. E. Drullinger, T. M. Fortier, J. E. Stalnaker, S. A. Diddams, W. C. Swann, N. R. Newbury, W. M. Itano, D. J. Wineland, and J. C. Bergquist. Frequency ratio of  $\text{Al}^+$  and  $\text{Hg}^+$  single-ion optical clocks. *Science DOI 10-1126*, 2008.
- [29] Chr. Tamm, S. Weyers, B. Lipphardt, and E. Peik. Stray-field-induced quadrupole shift and absolute frequency of the 688-thz  $^{171}\text{Yb}^+$  single-ion optical frequency standard. *Phys. Rev. A*, 80:043403, 2009.
- [30] Chr. Tamm, N. Huntemann, B. Lipphardt, V. Gerginov, N. Nemitz, S. Kazda, S. Weyers, and E. Peik. Cs-based optical frequency measurement using cross-linked optical and microwave oscillators. *Phys. Rev. A*, 89:023820, 2014.
- [31] N. Huntemann, M. Okhapkin, B. Lipphardt, S. Weyers, Chr. Tamm, and E. Peik. High-accuracy optical clock based on the octupole transition in  $^{171}\text{Yb}^+$ . *Phys. Rev. Lett.*, 108:090801, 2012.
- [32] M. Roberts, P. Taylor, G. P. Barwood, P. Gill, H. A. Klein, and W. R. C. Rowley. Observation of an electric octupole transition in a single ion. *Phys. Rev. Lett.*, 78:1876, 1997.
- [33] M. Chwalla, J. Benhelm, K. Kim, G. Kirchmair, T. Monz, M. Riehe, P. Schindler, A. S. Villar, W. Hänsel, C. F. Roos, R. Blatt, M. Abgrall, G. Santarelli, G. D. Rovera, and Ph. Laurent. Absolute frequency measurement of the  $^{40}\text{Ca}^+ 2\text{S}_{1/2}$  to  $2\text{D}_{5/2}$  clock transition. *Phys. Rev. Lett.*, 102:023002, 2009.
- [34] T. Rosenband, D. B. Hume, P. O. Schmidt, T. M. Fortier, J. E. Stalnaker, S. A. Diddams, W. M. Itano, J. C. J. Koelemeij, D. J. Wineland, and J. C. Bergquist. Observation of the  $^1\text{S}_0$  to  $^3\text{P}_0$  clock transition in  $^{27}\text{Al}^+$ . *Phys. Rev. Lett.*, 98:220801, 2007.
- [35] T. Schneider, E. Peik, and Chr. Tamm. Sub-hertz frequency comparisons between two trapped  $^{171}\text{Yb}^+$  ions. *Phys. Rev. Lett.*, 94:230801, 2005.
- [36] P.J. Blythe, S.A. Webster, K. Hosaka, and P. Gill. Systematic frequency shifts of the 467 nm electric octupole transition in  $^{171}\text{Yb}^+$ . *J. of Phys. B*, 36:981, 2003.
- [37] H. S. Margolis, G. Huang, G. P Barwood, S. N. Lea, H. A. Klein, W. R. C Rowley, P. Gill, and R. S. Windeler. Absolute frequency measurement of the 674 nm  $^{88}\text{Sr}^+$  clock transition using a femtosecond optical frequency comb. *Phys. Rev. A*, 67:032501, 2003.
- [38] J. von Zanthier, M. Eichenseer, A. Yu. Nevsky, M. Okhapkin, Ch. Schwedes, and H. Walther. A single indium ion optical frequency standard. *Laser Physics*, 15:1021, 2005.
- [39] S. G. Porsev, A. Derevianko, and E. N. Fortson. Possibility of an ultra-precise optical clock using the  $6 1\text{S}^0-6 3\text{P}^0$  transition in  $^{171,173}\text{Yb}$  atoms held in an optical lattice. *Phys. Rev. A*, 69:021403, 2004.
- [40] A. V. Taichenachev, V. I. Yudin, C. W. Oates, C. W. Hoyt, Z. W. Barber, and L. Hollberg. Magnetic field-induced spectroscopy of forbidden optical transitions with application to lattice-based optical atomic clocks. *Phys. Rev. Lett.*, 96:083001, 2006.

- [41] Chang Yong Park, Dai Hyuk Yu, Won Kyu Lee, Sang Eon Park, Eok Bong Kim, Sun Kyung Lee, Jun Woo Cho, Tai Hyun Yoon, Jongchul Mun, Sung Jong Park, Taeg Yong Kwon, and Sang Bum Lee. Absolute frequency measurement of the  $^1S_0$  to  $^3P_0$  transition of the  $^{171}\text{Yb}$  atoms in a one dimensional optical lattice at KRISS. *Metrologia*, 50, 2013.
- [42] N. Poli, Z. W. Barber, N. D. Lemke, C. W. Oates, L. S. Ma, J. E. Stalnaker, T. M. Fortier, S. A. Diddams, L. Hollberg, J. C. Bergquist, A. Brusch, S. Jefferts, T. Heavner, and T. Parker. Frequency evaluation of the doubly forbidden  $^1S_0$  to  $^3P_0$  transition in bosonic  $^{174}\text{Yb}$ . *Phys. Rev. A*, 77:050501, 2008.
- [43] St. Falke, H. Schnatz, J. S. R. Vellore Winfred, Th. Middelmann, St. Vogt, S. Weyers, B. Lipphardt, G. Grosche, F. Riehle, U. Sterr, and Ch. Lisdat. The  $^{87}\text{Sr}$  optical frequency standard at PTB. *Metrologia*, 48:399, 2011.
- [44] G. Campbell, A. Ludlow, S. Blatt, J. Thomsen, M. Martin, M. de Miranda, T. Zelevinsky, M. Boyd, J. Ye, S. Diddams, T. Heavner, T. Parker, and S. Jefferts. The absolute frequency of the  $^{87}\text{Sr}$  optical clock transition. *Metrologia*, 45:539, 2008.
- [45] S. Falke, N. Lemke, C. Grebing, B. Lipphardt, S. Weyers, V. Gerginov, N. Huntemann, C. Hagemann, A. Al-Masoudi, S. Haefner, S. Vogt, U. Sterr, and C. Lisdat. A strontium lattice clock with  $3 \times 10^{-17}$  inaccuracy and its frequency. *New Journal of Physics*, 16:073023, 2014.
- [46] T. Akatsuka, M. Takamoto, and H. Katori. Three-dimensional optical lattice clock with bosonic  $^{88}\text{Sr}$  atoms. *Phys. Rev. A*, 81:023402, 2010.
- [47] J.J. McFerran, D.V. Magalhaes, C. Mandache, J. Millo, W. Zhang, Y. Le Coq, G. Santarelli, and S. Bize. Laser locking to the  $^{199}\text{Hg}$   $^1S_0$ - $^3P_0$  clock transition with  $5.4 \times 10^{-15}/\sqrt{\tau}$  fractional frequency instability. *Opt. Lett.*, 37:3477, 2012.
- [48] M. Peterson, R. Chicireanu, S.T. Dawkins, D.V. Magalhaes, C. Mandache, A. Clairon, Y. Le Coq, and S. Bize. Doppler-free spectroscopy of the  $^1S_0$ - $^3P_0$  optical clock transition in laser-cooled fermionic isotopes of neutral mercury. *Phys. Rev. Lett.*, 101:183004, 2008.
- [49] J. Bland-Hawthorn and P. Kern. Astrophotonics: a new era for astronomical instruments. *Opt. Expr.*, 17:1880, 2009.
- [50] F. Merkt and T. Softley. Final-state interactions in the zero-kinetic-energy-photoelectron spectrum of  $\text{H}_2$ . *J. Chem. Phys.*, 96:4149, 1992.
- [51] C. Campbell, A. Radnaev, and A. Kuzmich. Wigner crystals of  $^{229}\text{Th}$  for optical excitation of the nuclear isomer. *Phys. Rev. Lett.*, 106:223001, 2011.
- [52] S. T Cundiff. Phase stabilization of ultrashort optical pulses. *J. of Phys. D*, 35:R43, 2002.
- [53] S. T Cundiff and J. Ye. Colloquium: Femtosecond optical frequency combs. *Reviews of Modern Physics*, 75:325, 2003.
- [54] W.J. Riley. Techniques for Frequency Stability Analysis. In *IEEE International Frequency Control Symposium*, 2003.

- [55] J. Davis. Clock and Time Transfer Statistics and Analysis Techniques. In *European Frequency and Time Forum*, 2012.
- [56] N. Poli, C.W. Oates, P. Gill, and G.M. Tino. Optical atomic clocks. *La rivista del Nuovo Cimento*, 36:555, 2013.
- [57] N.D. Lemke, J. von Stecher, J.A. Sherman, A.M. Rey, A.D. Ludlow, and C.W. Oates. p-wave cold collisions in an optical lattice clock. *Phys. Rev. Lett.*, 107:103902, 2011.
- [58] Zeb Barber. *Ytterbium Optical Lattice Clock*. PhD thesis, University of Colorado, 2007.
- [59] S. Porsev and A. Derevianko. Multipolar theory of blackbody radiation shift of atomic energy levels and its implications on optical lattice clocks. *Phys. Rev. A*, 74:020502, 2006.
- [60] J.A. Sherman, N. D. Lemke, N. Hinkley, M. Pizzocaro, R.W. Fox, A. D. Ludlow, and C. W. Oates. High accuracy measurement of atomic polarizability in an optical lattice clock. *Phys. Rev. Lett.*, 108:153002, 2012.
- [61] H. J. Metcalf and P. Van der Straten. *Laser Cooling and Trapping*. Springer-Verlag, 1999.
- [62] W. D. Phillips and H. Metcalf. Laser deceleration of an atomic beam. *Phys. Rev. Lett.*, 48:596, 1982.
- [63] V.S. Letokhov, V.G. Minogin, and B.D. Pavlik. Cooling and trapping of atoms and molecules by a resonant light field. *Opt. Comm.*, 19:698, 1976.
- [64] V. S. Lethokov. Narrowing of the doppler width in a standing light wave. *JETP Letters*, 7:272, 1968.
- [65] C. Salomon, J. Dalibard, A. Aspect, H. Metcalf, and C. Cohen-Tannoudji. Channeling atoms in laser standing wave. *Phys. Rev. Lett.*, 59:1659, 1987.
- [66] A. Yamaguchi, N. Shiga, S. Nagano, H. Ishijima, Y. Koyama, M. Hosokawa, and T. Ido. A strontium optical lattice clock. *Journal of the National Institute of Information and Communication Technology*, 57:146, 2010.
- [67] R.H. Dicke. The effect of collisions upon the doppler width of spectral lines. *Phys. Rev. Lett.*, 89:472, 1953.
- [68] D.J. Wineland and W.M. Itano. Laser cooling of atoms. *Phys. Rev. A*, 20:1521, 1979.
- [69] R. Grimm, M. Weidemüller, and Y. Ovchinnikov. Optical dipole traps for neutral atoms. *Advances in Atomic, Molecular and Optical Physics*, 42:95, 1999.
- [70] J. Mitroy, M. S. Safronova, and Charles W. Clark. Theory and applications of atomic and ionic polarizabilities. *J. of Phys. B*, 43:202001, 2010.
- [71] Handbook of Basic Atomic Spectroscopic Data  
. <http://www.nist.gov/pml/data/handbook/index.cfm>, 2009 (accessed September 19,2014).

- [72] NIST Atomic Spectra Databases  
. <http://physics.nist.gov/PhysRef-Data/ASDA1>.
- [73] I. I. Sobelman. *Atomic Spectra and Radiative Transitions*. Springer-Verlag, 2 edition, 1992.
- [74] C. J. Bowers, D. Budker, E. D. Commins, A. T. Nguyen, D. DeMille, S. J. Freedman, S. Q. Shang, and M. Zolotarev. Experimental investigation of excited state lifetimes in atomic ytterbium. *Phys. Rev. A*, 53:3103, 1996.
- [75] C. W. Hoyt, Z. W. Barber, C. W. Oates, T. M. Fortier, S. A. Diddams, and L. Hollberg. Observation and absolute frequency measurements of the  $^1S^0$ - $^3P^0$  optical clock transition in neutral ytterbium. *Phys. Rev. Lett.*, 95:083003, 2005.
- [76] C. W. Hoyt, Z. W. Barber, C. W. Oates, L. Hollberg, A. V. Taichenachev, and V. I. Yudin. Direct excitation of the forbidden clock transition in neutral  $^{174}\text{Yb}$  atoms confined to an optical lattice. *Phys. Rev. Lett.*, 96:083002, 2006.
- [77] C.J. Bowers, D. Budker, E.D. Commins, D. DeMille, S.J. Freedman, A.T. Nguyen, S.Q. Schang, and M. Zolotarev. Experimental investigation of excited-state lifetimes in atomic ytterbium. *Phys. Rev. A*, 53:3103, 1996.
- [78] P. Tipler. *Modern Physics*. Worth Publishers, 1985.
- [79] E. Black. An introduction to pound-drever-hall laser frequency stabilization. *Am. J. Phys.*, 69:79, 2000.
- [80] A. Nevsky, U. Bressel, C. Eisele, M. Okhapkin, S. Schiller, A. Gubenko, D. Livshits, S. Mikhlin, I. Krestnikov, A. Kovsh, S. Vogt, C. Lisdat, T. Legero, U. Sterr, and I. Ernsting. A narrow-line-width external cavity quantum dot laser for high-resolution spectroscopy in the near-infrared and yellow spectral ranges. *Appl. Phys. B*, 92:501, 2008.
- [81] S. Vogt, C. Lisdat, T. Legero, U. Sterr, I. Ernsting, A. Nevsky, and S. Schiller. Demonstration of a transportable 1 hz-linewidth laser. *Appl. Phys. B*, 104:741, 2011.
- [82] L.S. Ma, P. Jungner, J. Ye, and J.L. Hall. Delivering the same optical frequency at two places: accurate cancellation of phase noise introduced by an optical fiber or other time-varying path. *Opt. Lett.*, 19:1777, 1994.
- [83] Tobias Franzen. Aufbau eines eindimensionalen optischen Gitters für eine Ytterbium-Atomuhr.
- [84] C. Monroe, W. Swann, H. Robinson, and Wieman.C. Very cold trapped atoms in a vapor cell. *Phys. Rev. Lett.*, 65:1571, 1990.
- [85] T. Brzozowski, M. Maczynska, M. Zawada, J. Zachorowski, and W. Gawlik. Time-of-flight measurement of the temperature of cold atoms for short trap-probe beam distances. *J. of Opt. B*, 4:62, 2002.
- [86] T.A. Savard, K.M. O'Hara, and J.E. Thomas. Laser-noise-induced heating in far-off resonance optical traps. *Phys. Rev. A*, 56:1095, 1997.

- 
- [87] H. Dehmelt. Proposed  $10^{14}$   $dv < v$  laser fluorescence spectroscopy on  $\text{Tl}^+$  mono-ion oscillator ii (spontaneous quantum jumps). *Bull. Am. Phys. Soc.*, 20:637, 1975.
- [88] S. Barnett. On the recoil and doppler shifts. *J. Mod. Opt.*, 57:1445, 2010.
- [89] G. Mura, T. Franzen, C. Abou Jaoudeh, A. Görlitz, H. Luckmann, I. Ernsting, A. Nevsky, S. Schiller, and SOC team. A transportable optical lattice clock using  $^{171}\text{Yb}$ . In *2013 IFCS-EFTF proceedings*, 2013.
- [90] Martin Boyd. *High Precision Spectroscopy of Strontium in an Optical Lattice: Towards a New Standard for Frequency and Time*. PhD thesis, University of Colorado, 2007.
- [91] N. D. Lemke. *Optical Lattice Clock with Spin 1/2 Ytterbium atoms*. PhD thesis, University of Colorado, 2012.



# Erklärung

Hiermit versichere ich, die vorliegende Arbeit selbständig und nur unter Zuhilfenahme der angegebenen Quellen und Hilfsmittel angefertigt und Zitate kenntlich gemacht zu haben.



# ACKNOWLEDGEMENTS

A lot of people, to whom I am thankful, collaborated to this work through technical, emotional and financial support.

Prof. Axel Görlitz ... Thank you!

Prof. Stephan Schiller ... Thank you!

Friedrich-Naumann-Stiftung für die Freiheit ... Thank you!

Gregor Mura and Tobias Franzen (clock team) ... Thank you!

Christian Bruni and Frank Münchow (molecules team) ... Thank you!

Ralf Stefan (Dr. Gadget) ... Thank you!

And for my family and wife, no words can express how thankful I am for your presence in my life.

Jean Abou Jaoudeh ... Maallim

Rita Abou Jaoudeh ... A7la Mara

Katja Abou Jaoudeh ... Jnudel

Jessy Abou Jaoudeh ... Mokh

Wissam Abou Jaoudeh ... Akrouf